Mode-coupling regimes in 2D plasma crystals

Thomas Bernhard Röcker

München 2014

Mode-coupling regimes in 2D plasma crystals

Thomas Bernhard Röcker

Dissertation
an der Fakultät für Physik
der Ludwig–Maximilians–Universität
München

vorgelegt von
Thomas Bernhard Röcker
aus München

München, den 21.03.2014

Erstgutachter: Prof. Dr. Dr. h.c. Gregor Morfill
Zweitgutachter: Prof. Dr. Hartmut Zohm
Tag der mündlichen Prüfung: 30.07.2014

"We have to learn again that science without contact with experiments is an enterprise which is likely to go completely astray into imaginary conjecture."
Hannes Alfvén

Contents

List of Figures

Zusammenfassung

Diese Arbeit ist eine kumulative Dissertation und besteht aus drei Aufsätzen. Sie setzt die Studien der Diplomarbeit zur eigenständig kohärenten Beschreibung der wakevermittelten Modenkopplung in Plasmakristallen fort.

Der erste Aufsatz untersucht die Ionengeschwindigkeitsverteilung (idf) in einem schwachionisierten Gas, welches einem homogenen elektrischen Feld ausgesetzt ist und in dem Ladungsaustauschkollisionen der dominante Stoßtyp sind. Die Untersuchung geht dabei nur von elementaren Grundprinzipien aus und ist somit eigenständig kohärent. Die „Referenzverteilung" wird mittels einer Monte-Carlo-Simulation (MC-Simulation) am Beispiel des energieabhängigen Wirkungsquerschnitts für Argon berechnet. Ich nutze mehrere analytische Modelle (basierend auf einem konstanten Wirkungsquerschnitt oder konstanter Stoßfrequenz) und vergleiche die entsprechenden idfs untereinander, sowie mit der Referenzlösung. Es zeigt sich, dass kein Modell für den experimentell häufig wichtigen Fall eines schwach suprathermalen Ionenstroms mit befriedigender Genauigkeit anwendbar ist. Einen konstanten Wirkungsquerschnitt und Separabilität der idf annehmend, sowie darauf folgende Maxwell-gewichtete Mittelung, reduziert die integro-differentielle Boltzmanngleichung zu einer gewöhnlichen Differentialgleichung. Ich zeige, dass ihre Lösung die Resultate der MC-Simulation, für *beliebige* Stärke des Ionenstroms, mit großer Genauigkeit reproduziert. Das gewonnene Modell lässt sich auf eine Vielzahl von Problemen im Bereich der komplexen Plasmen anwenden - darunter der Ladungsvorgang der Staubteilchen, die Bildung von Wakefeldern und nicht-Hamiltonische Dynamik.

Im zweiten Aufsatz behandle ich das vorrangige Beispiel eines nicht-Hamiltonischen Prozesses in zweidimensionalen (2D) Plasmakristallen: Die Modenkopplungsinstabilität (MCI), induziert durch die wakevermittelte Wechselwirkung der Staubteilchen. Durch das Einbinden des Formalismus einer linearen Plasmarückantwort (zur eigenständig kohärenten Beschreibung der Teilchenwechselwirkung) wird die bisherige Theorie erweitert. Ich verwende dazu die Ergebnisse des ersten Aufsatzes für subthermale und suprathermale Ionenströme. Ein Abbildungsverfahren setzt die eigenständig kohärenten Kopplungskoeffizienten und das effektive Dipolmoment der Wakes miteinander in Beziehung. Das Dipolmoment ist ein fundamentaler Parameter, welcher die Modenkopplung im üblicherweise verwendeten „Yukawa-Punktwake-Modell" charakterisiert. Ich wende das Abbildungsverfahren auf verfügbare experimentelle Daten an. Die resultierende Größenordnung des Dipolmoments zeigt in mehreren Fällen das Vorliegen *starker* Modenkopplung an. Diese wurde zuvor nie systematisch untersucht.

Dieses Ergebnis motiviert die Untersuchungen der dritten Veröffentlichung: Ich studiere den Einfluss starker Staubteilchen-Wake-Wechselwirkungen auf Dispersion und Polarisation von Staubgittermoden in 2D-Plasmakristallen. Die starke Kopplung bewirkt eine „Anziehung" zwischen den Moden und macht ihre Polarisationen elliptisch. Bei Hybridisierung rotieren die Hauptachsen der Lissajous-Ellipsen um 45° (bleiben aber weiterhin senkrecht zueinander). Um die Implikationen für Experimente aufzuzeigen, berechne ich die entsprechenden Teilchenbahnen und spektrale Dichten der longitudinalen und transversalen Moden. Beide Observablen offenbaren deutliche Spuren elliptischer Polarisation. Abschließend untersuche ich die Verschiebung der Hybridisierung bei starker Kopplung. Der Effekt ist signifikant: Das Einsetzen der Hybridisierung erfolgt bei Wellenzahlen welche merklich kleiner sind als die Grenze der Brillouin-Zone (wo die Hybridmode bei schwacher Kopplung zuerst auftritt).

Abstract

The present work is a cumulative thesis consisting of three refereed publications. It continues the diploma studies dealing with the self-consistent investigation of wake-mediated mode-coupling in plasma crystals.

In the first paper, I investigate the ion-velocity distribution function (idf) of a weakly-ionized gas, subjected to a uniform electric field and ion-neutral charge-exchange collisions. The "reference" idf, based on the energy-dependent cross-section for argon, is calculated by Monte-Carlo (MC) simulations. I consider several analytical models (based on either constant cross-section or constant collision-frequency) and compare them with each other and to MC results. It is demonstrated that none of available models applies to the experimentally often relevant situation of slightly suprathermal ion-flow. Assuming constant cross-section and separability of idf, followed by subsequent application of Maxwellian-averaging, the integro-differential Boltzmann equation is reduced to a simple differential equation. Evidently, its solution reproduces the reference idf with good accuracy for *arbitrary* value of field strength. These studies are of fundamental importance for a variety of problems in complex plasmas - among them the charging of dust grains, the formation of wake fields and non-Hamiltonian dynamics.

The second paper deals with the primary example of non-Hamiltonian dynamics in two-dimensional (2D) plasma crystals: The mode-coupling instability (MCI), induced by the wake-mediated interactions between grains. The corresponding theory is extended by using the linear-response formalism for the self-consistent description of particle interactions. In this approach, I employ the results from the first paper for subthermal and suprathermal regimes of ion flow. A mapping procedure relates the self-consistent coupling coefficients to the effective wake dipole moment - the parameter essentially characterizing the mode coupling in the framework of conventionally used Yukawa/point-wake model. I apply the mapping to several available experiments and compare theoretically obtained dipole moments with experimental data. In several cases, the resulting magnitude of dipole moment indicates *strong* mode-coupling, which was never systematically studied.

In the third publication, I investigate the effects of strong grain-wake interactions on dispersion and polarization of dust-lattice wave modes in 2D plasma crystals. Strong coupling causes an "attraction effect" between the modes, making their polarizations elliptical. Upon hybridization, the Lissajous ellipses major axes rotate by 45° (but remain mutually orthogonal). I show the implications for experiments by calculating representative particle trajectories and spectral densities of longitudinal and transverse waves. Both these observ-

ables reveal the distinct fingerprints of elliptical polarization. Furthermore, I investigate the shift of the hybrid mode at strong coupling. The effect is found to be significant: The hybridization onset is at wave numbers which are notably smaller than the border of the first Brillouin zone (where the onset takes place in the regime of weak coupling).

Chapter 1

Introduction

This section provides the basic knowledge about complex plasmas which is essential for understanding the thesis' results. Here, the presentation is mostly kept qualitative to allow fluent reading. Where necessary, instructive formulas or numbers are given and typical scales are estimated. Readers interested in further details may refer to the cited references.

1.1 A plasma state of soft matter

The interdisciplinary complex plasma research spans various fields, including (i) the physics of ionized gases [1, 2], (ii) cosmic plasmas [3, 4], (iii) plasma processing/engineering [5, 6] and (iv) the field of soft matter [7, 8]. While investigations of (i) and (ii) reach back to the 1960s, (iii) and (iv) were mainly developed in the last two decades, providing a different approach to complex plasmas: The latter are regarded as the plasma state of soft matter (analogue to complex fluids [9]), being a binary mixture of a (micromolecular) weakly ionized gas-component and a (macromolecular) microparticle-component. Such systems are specifically designed for laboratory purpose and can be essentially treated as an "one-phase fluid", when the interactions between microparticles dominate [8].

The microparticles ("dust" or "grains") are individually observable and the system is optically thin. Therefore three-dimensional diagnostics and easy manipulation (e.g. by Langmuir probe [10], laser radiation pressure [11] or electromagnetic fields [12, 13]) on the most fundamental level, the individual particle level ("kinetic level"), are possible. Moreover the energy and momentum exchange rates can exceed typical damping rates substantially, letting the system reach equilibrium easily, thus making dynamical processes observable [8, 14]. All these aspects privilige complex plasmas to serve as model for strong-coupling phenomena in cognate systems, e.g., colloids (dynamics take very long), ion crystals (confinement requires high effort) or even fluids and solids (observation on kinetic level difficult).

In complex plasmas, the microparticle subsystem is thermodynamically open due to (i) plasma absorption by the grains which results in spatially strongly varying grain charges, and (ii) the formation of wake fields behind the grains. Consequently, the concepts of

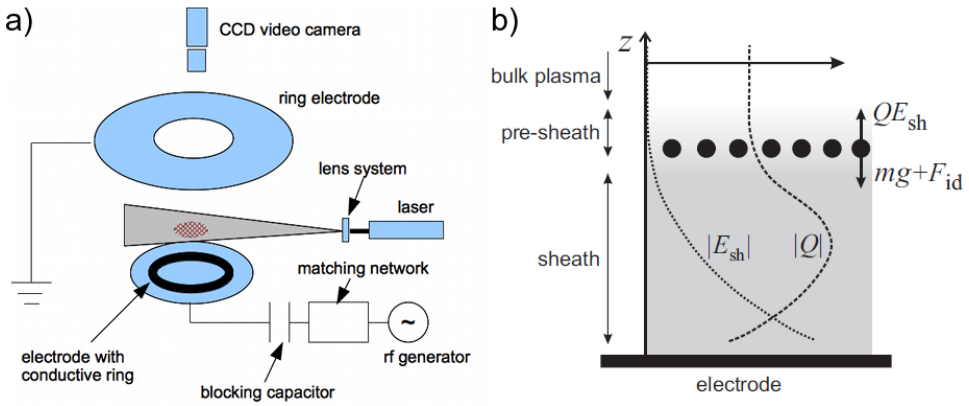

Figure 1.1: a) Typical setup in ground-based complex plasma experiments. The red pattern depicts the dust grains. The vacuum chamber is not shown here. b) Gravitational, ion-drag and (averaged) sheath electric force - mg, F_{id}, QE_{sh}, respectively - acting on the microparticles in the (pre)sheath. The dotted and dashed curves show the qualitative progression of equilibrium particle charge $|Q|$ and electric field modulus $|E_{\mathrm{sh}}|$, respectively. z denotes the (vertical) distance from the lower electrode. At the grains levitation height, the electric field force compensates for gravity and ion drag. From Ref. [7].

Hamiltonian dynamics and free energy are generally inapplicable. These points distinguish complex plasmas from an ordinary state of matter (e.g. solid, fluid) and provide a broad range of new effects [15]. The present work focuses on aspect (ii) affecting the mutual grain interactions.

1.2 Two-dimensional plasma crystals in rf-sheaths

Most ground-based complex plasma experiments[1] are performed in the "Gaseous-Electric-Conference chamber" [19] (compare Fig. 1.1a). It consists of a grounded, cylindrical-symmetric vacuum chamber, filled with an inert gas (pressure 0.1-1000 Pa) and equipped with glass windows allowing the observation of plasma from top and side. An electrode (diameter 10-15 cm) is mounted at the chambers bottom and connected to a radio-frequency (rf) generator (via blocking capacitor and matching network), usually driven with 13.56 MHz at 10-100 W. Either the grounded chamber itself acts as counter-electrode or a grounded ring-electrode is positioned parallel to the lower electrode (separation 2-4 cm). In between the electrodes, a low-temperature and low-density (near the midplane, the ratio of electron/ion density and neutral density, $n_{e,i}/n_n$, is around 10^{-8}-10^{-6}) plasma is produced.

Its electrons can quasi-instantaneously respond to the alternating rf-field configuration,

[1] Still, other experimental setups are available, e.g. ground-based dc-discharges [16] or discharges under microgravity conditions [17, 18].

while ions only respond to the average sheath field, due to their much larger masses. Thus a "bulk region" is established near the midplane of discharge, where the electrons have temperatures T_e of a few eV, while the ions are in (quasi-)thermal equilibrium with neutrals. Therefore, the ion velocities follow a Maxwellian distribution characterized by the neutrals temperature T_n. This can be regarded as a direct consequence of low plasma-density, i.e., ions (and electrons) collide with neutrals much more often than with each other which "maxwellizes" the ion-velocity distribution function (idf). The high-energetic electron-neutral collisions and resulting impact ionizations sustain the plasma.

Due to the relatively small electron-masses, the electron flux toward the chambers walls is much higher than the corresponding ion flux. Therefore the lower electrode acquires a negative self-bias (the reason for the blocking capacitor) of some tens of volts. Conclusively, the average electric field in a plasma layer near the chamber walls is non-zero (with increasing field strength toward the walls), repelling and attracting electrons and ions, respectively. This layer is termed "plasma sheath", the transition area from bulk to sheath is the "presheath" (Fig. 1.1b).

The (averaged) electric field induces a strong ion-downstream. The corresponding longitudinal[2] idf has a long high-energy "tail" as many ions have velocities larger than the downstreams "flow velocity" u_i[3]. Normalizing the latter by the neutrals' thermal velocity $v_T = \sqrt{T_n/m_n}$ (m_n is the mass of neutrals), one obtains the corresponding "thermal Mach number" M_T characterizing the anisotropy of idf: For $M_T < 1$ ($M_T > 1$) the idf is close to (notably different from) the aforementioned Maxwellian and the flow is called "subthermal" ("suprathermal").

The microparticles (usually mono-disperse melamine-formaldehyde microspheres with a few μm diameter and mass $m \simeq 10^{-14}$ - 10^{-12} kg) are injected from particle dispensers at the chambers top. They are lighted by a laser sheet (approximately 100 μm width) and observed with video cameras (10-1000 fps). A conductive ring placed on the lower electrode (or a ring-shaped groove) produces a electric field horizontally confining the particles.

The injection of dust perturbs the plasmas quasi-neutrality. Absorption of the resulting ion- and electron-fluxes charge the microparticles up[4]. Under special circumstances (e.g. laser-heated grains, highly-charged but yet small particles, high neutral density) [14], other charging mechanisms (e.g. the photoelectric effect, emission of secondary electrons, radioactivity) are superimposed. After a typical timescale of 0.1-10 μs (depending on the concrete charging method and ratio of ion- to electron-temperature [21]), the flux balance determining the (usually negative) quasi-stationary[5] grain charge Q is reached [22]. Usually, Q is some ten thousand electron charges per micron of grain diameter.

The particles acquire their quasi-stationary levitation height (perturbed by thermal fluctuations) in a narrow region close to (or in) the sheath, where the (averaged) electric

[2] with respect to the ion flow

[3] Defined as the first moment of longitudinal idf.

[4] The charging fluxes can be described by the "Orbit-limited motion" theory, working well under typical experimental conditions [20, 21].

[5] Due to random absorption and emission, Q fluctuates around its mean-value [23]. Under certain circumstances, this can result in spontaneous grain heating. Compare Ref. [24, 25] and Sec. 1.3.

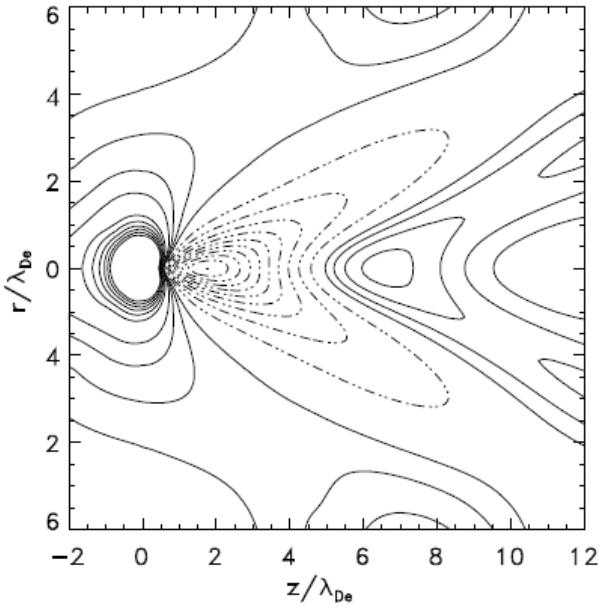

Figure 1.2: Potential of a charged grain (situated at the most left node) and its plasma wake in cylindrical coordinates r, z (normalized by the electron-Debye length). Solid and dashed lines indicate repulsive and attractive regions, respectively. The corresponding calculations assume Boltzmann response for electrons and collisionless ions following a shifted Maxwellian velocity distribution which is peaked at thermal Mach number $M_T = 7.5$ (suprathermal ion-flow). From Ref. [39].

field compensates for gravity and drag force exerted by the directional ion-flow[6] (compare Fig. 1.1b) [27, 28]. The balance of forces induces a strong vertical confinement [10]. The measurement of corresponding resonance frequency Ω_{conf} allows the experimental evaluation of Q [15].

The aforementioned "ion-drag force" has contributions from (i) ion absorption on the grain[7], and (ii) ion scattering (where the grain acts as lens for the flowing plasma). The latter results in a region of perturbed ion-flow (viz. a local plasma polarization) behind every grain, termed "plasma wake" [33]. Though in several publications oscillatory wake structures (a series of potential maxima and minima) were reported [34–38], this effect is typically smeared out [8], leaving a single attractive region (compare Fig. 1.2) whose shape is sensitive to ion-neutral collisions [10, 39, 40]. The scattering contribution to the ion-drag force can be interpreted as the electrostatic interaction of the microparticle with its own wake [41,42], i.e., for a motionless grain at the origin and potential ϕ, the expression $F_{\text{id}} = -Q\nabla\phi|_{\mathbf{r}=0}$[8] is found. In terms of kinetic theory, the scattering part of force originates from Landau damping.

A self-consistent expression for the linearised grain potential[9] ϕ can be obtained by applying the "linear dielectric response formalism" [45] to the Poisson equation and kinetic equation for ions[10] [46]. The found expression is valid in regions where the plasma is weakly

[6] In certain environments, magnetic or/and thermophoretic forces have to be considered as well [26].

[7] This makes corrections to the Orbit-limited motion approach necessary [29–32].

[8] It should be noted that for small M_T the ion-drag force can be calculated as well from the "binary collision approach" [43, 44]. It presumes a particular form of idf (e.g. shifted Maxwellian) and thus the approach is not self-consistent.

[9] From here on, ϕ denotes the linearised potential, i.e., the leading term of potential expansion in a series of Q.

[10] Principally, the kinetic equation for electrons has to be considered as well. Most investigations either

coupled to the grain (termed "regions of linear screening"). This is the case in regions where the ions and electrons potential energies (due to the electric grain field) are small, compared to the corresponding effective temperatures. Close to the grains surface the screening gets highly non-linear. This region is usually much smaller than the corresponding effective screening length λ. Refs. [42, 51, 52] suggest that the screening in the sheath ($M_T \gg 1$, as found in many ground-based experiments) is mostly due to ions, while near the sheath-presheath edge electrons provide a comparable contribution [10,14], i.e., $\lambda \simeq \sqrt{T_i/(4\pi e^2 n_i)}$, where T_i is the characteristic kinetic energy of ions.

It is reasonable to *exclusively* consider the charge-exchange collisions (i.e. ion and neutral atom switch identity) in the collision integral of ion-kinetic equation. Elastic and Coulomb-type collisions provide much smaller effect on the ion momentum (except for highest density discharges [14, 53, 54]).

Schweigert *et al.* [55] and Ivlev *et al.* [42] considered for the modelling of charge-exchange collisions the Bhatnagar-Gross-Krook (BGK) collision operator [56]: It is constructed from the classical "Stosszahlansatz" and presumes a velocity-independent collision frequency. For $M_T \ll 1$, the leading order of the resulting expression for ϕ is the spherically-isotropic Yukawa potential. Higher orders in M_T tend to make ϕ anisotropic and attractive in a certain region downstream from the particle (unison with experimental observations [10, 57]). Further on, this approach is termed CCF ("constant collision frequency") model.

Kompaneets *et al.* employed a collision operator with *constant* charge-exchange cross-section, mimicking a mobility-limited ion-drift with constant mean-free path [51]. Furthermore, the velocity distribution of neutrals was assumed to be sharply peaked around zero, i.e., it was modelled by the Dirac-delta function. In transverse direction[11], the resulting potential scales Yukawa-like [$\propto r^{-1}\exp(r/\lambda)$] in a narrow region around the particle ($r \simeq 0.5\text{-}4\,\lambda$), but exhibits a notably different behaviour [$\propto 1/r^3$] for smaller and larger distances. In longitudinal direction, the potential was found to be attractive. It scales dipole-like [$\propto 1/r^2$] for large r. The expressions are in excellent agreement with measurements of mutual particle attraction, performed at strong ion flow ($M_T \simeq 10$). In the following, the model is referred as CMP ("constant mean-free path") model.

Although the assumption of constant cross-section is a meaningful approximation in a wide range of Mach numbers (the cross-section depends only weakly logarithmic on the colliders relative velocity) [58–61], neither the assumption of constant collision frequency in CCF model, nor the hypothesis of infinitesimally small neutral-velocity distribution in CMP model, are generally applicable. They are only reasonable for small and large M_T, respectively. Thus, there are three fundamental open questions:

- For which ranges of M_T are CCF and CMP models reasonably applicable?
- Which is the appropriate "transition" model?
- Is it possible to provide a "universal" solution, valid for all Mach numbers?

neglect the perturbation of the electron velocities or consider Boltzmann response [31, 34, 35, 37, 39]. The real situation might be more complicated. Compare Refs. [47–50] and Sec. 3.

[11] with respect to the ion flow

In Sec. 2.1 and 2.2, these question are systematically studied.

Employing one of the discussed models for ϕ, one can calculate the interaction energy $V = Q\phi|_{r=\Delta}$ of two isolated[12] grains levitated at the same height and separated by distance Δ. The corresponding coupling strength of particles (at kinetic dust temperature T_d) is depicted by the "screened coupling parameter" $\Gamma_\mathrm{s} = Q^2/(T_d\Delta)e^{-\Delta/\lambda}$: For Γ_s being larger than the melting curve $\Gamma_M(\kappa)$[13], a strongly-coupled "condensate" of microparticles, the "plasma crystal"[14], can be formed. The "screening parameter" $\kappa = \Delta/\lambda$ is typically close to one yielding $\Gamma_\mathrm{s} \gtrsim 10^2$ as crystallisation condition [62, 63].

Within a plasma crystal (the case of non-isolated dust grains), the interparticle forces are generally collective [15, 67], i.e., given the fact that the plasma flux to a certain grain (determining Q and λ) strongly depends on the presence of other charges, the force between two constituents of the crystal is a (rather complicated) function of *absolute* positions of *all* other microparticles. Still, for a vertically confined monolayer with *not* too high dust density ($\kappa \gtrsim 1$), the interparticle forces can be approximated as superposition of binary grain interactions [15].

The primary examples of plasma crystals are strongly coupled ($\Gamma_\mathrm{s} \simeq 10^4$-$10^5$, $\kappa \simeq$ 0.7-1.3) 2D monolayers[15] with hexagonal lattice cell[16] (Δ is in the sub-millimetre range), formed in the field of the (pre)sheath [68, 69]. Usually they consist of some ten thousand particles and have a horizontal extent of some cm. The monolayers stability is provided by confinement and its energy absorption from the ion flow [15, 75] saturated due to simultaneous cooling by dust-neutral collisions[17] [14, 108]. Given the fact that in most complex plasmas the Knudsen number [109] is much larger than unity, the dust-neutral friction force (orientated along the relative velocities) can be approximated by common Epstein formula [76] assuming diffusive scattering [77].

1.3 Non-Hamiltonian dynamics of dust lattice modes

Friction is a *universal* example (occurring in a broad range of fields) for a mechanism thermodynamically opening a physical system. In anisotropic complex plasmas further *system-specific* features, induced by the sheath field, make energy exchange between microparticles and ambient plasma possible:

- As previously mentioned, the grain charges and their screening depend on the *absolute* positions of all other particles in the crystal (collective interaction) and even for the case of reciprocal interactions (conserving the total momentum of the system) the electrostatic force cannot be expressed as gradient of a scalar function ϕ, i.e.,

[12] I.e. they are *not* constituents of a larger grain complex.

[13] The particular form of $\Gamma_\mathrm{M}(\kappa)$ depends essentially on the model used for ϕ [62–65].

[14] Similar to a Wigner-crystal [66].

[15] Furthermore, it is possible to form one-dimensional strings [70, 71], 2D multilayers and three-dimensional complexes [72–74].

[16] For smaller grains ($< 5\mu$m), even fcc, bcc, hcp and hexagonal cylindrical structures were observed [68].

[17] Usually, the electron drag is negligible compared to the neutral drag force [21].

$\mathbf{F} = -Q(\mathbf{r})\,\nabla\phi(\mathbf{r}) \neq -\nabla\big[Q(\mathbf{r})\,\phi(\mathbf{r})\big]$ [78]. Thus the work done over a circle process is *not* equal to zero, as follows from $\nabla\times\mathbf{F} = \nabla Q(\mathbf{r})\times\nabla\phi(\mathbf{r}) \neq 0$ and Stokes theorem.

- Apart from ion drag, the wakes exert attractive forces [79,80] on neighboring grains. In the mutual grain interaction, the wakes play the role of a third body (i.e. they are not a "fixed" part of the grain) making the interaction non-reciprocal. Therefore, the force $\mathbf{F}_{21\mathrm{w}}$ acting between particle 1 and the wake of particle 2 is generally different from $\mathbf{F}_{12\mathrm{w}}$, the force between particle 2 and the wake of particle 1 (compare Fig. 1.3).

These features identify plasma crystals as non-Hamiltonian systems[18] which do not conserve energy and cannot be adequately described in terms of Hamiltonian mechanics[19]. This may not be misinterpreted as a violation of Newtons third law, but it is a consequence of the plasma crystals "engineering" as a grain-interaction-dominated *one*-component fluid, i.e., the ambient plasma is treated as kind of "reservoir" charging and mediating the particles and their motion, respectively.

The crystals energy absorption from the ambient plasma can result in spontaneous grain heating [85, 89–92]. This process is well explained by the resonance of phonons. Before presenting the details on the resonance, the essentials of phonons in plasma crystals are briefly summarized.

In plasma crystals the phonon eigenfrequencies are relatively low, but still exceed the typical friction rates notably, i.e., the phonons can freely propagate[20] in form of weakly damped "dust-lattice" (DL) modes[21]. Typical phase velocities are of the magnitude of a few cm/s [97], the corresponding characteristic frequency- and time scales are the "dust-lattice frequency" $\Omega_{\mathrm{DL}} = \sqrt{Q^2/(m\lambda^3)}$ and fractions of seconds. Three types of DL modes can be sustained in a monolayer: The longitudinal and transverse in-plane modes (horizontal grain motion) [98,99] and the transverse out-of-plane mode (vertical grain motion[22]) [100]. Experimentally, the corresponding dispersion relations can be obtained by measuring thermal fluctuations and subsequent plotting in Fourier space [7,91]. The results indicate that both in-plane modes are acoustic, the out-of-plane mode is optical.

The wakes couple the acoustic "compression" in-plane and optical out-of-plane modes [89,90]. In case of weak vertical confinement and strong enough grain-interactions (experimentally both parameters can be easily controlled by decrease of rf-power and increase of particle number, respectively [91]), these "lower" and "upper" modes[23] are in resonance and

[18] Delayed charging [81,82] and random charge fluctuation [23, 83–85] result in non-Hamiltonian effects [25] as well. These examples are not specific for anisotropic complex plasmas, but occur as well in other experimental setups.

[19] It should be noted that reformulations of Hamiltonian dynamics, addressing the particular problem of non-conservative forces, exist. Compare Ref. [86–88].

[20] Although phonons are sustained in any liquid or solid elastic media, free propagation is not always possible: E.g. in colloids, where strong solvent damping allows only phonon diffusion [7].

[21] Apart from the usual plasma waves and the DL modes, complex plasmas provide a broad variety of linear and non-linear wave phenomena, e.g., dust bending waves [93], mach cones [94], and solitons [95,96].

[22] The stability of vertical motion is provided by the vertical confinement forces.

[23] For convenience, further on the "compression" in-plane and out-of-plane modes are termed "lower" and "upper" modes, respectively.

form lower and upper *hybrid* modes associated with coupled horizontal and vertical particle motion[24]. These modes are decaying and growing[25], respectively, but show the same dispersion. For weak dust-neutral friction (viz. the neutral gas pressure is low enough) the upper hybrid mode induces an instability (the "mode-coupling instability" or "MCI"): The microparticles absorb energy from the flowing plasma, which results in anomalously high kinetic energies and melting of the crystalline structure.

Although self-consistent wake models provide better agreement with experimental results [52], many theoretical investigations of MCI are still based on the simple "Yukawa/point-wake" model [89–92, 101], since it makes the analysis of new qualitative effects associated with the particle-wake interaction more transparent. In this model, the wake is considered as positive, point-like effective charge q, located at the distance δ below each grain (compare Fig. 1.3). Thus, the total interaction between two particles is a simple superposition of particle-particle and particle-wake interactions, both described by (spherically-symmetric) Yukawa potentials with effective screening length λ.

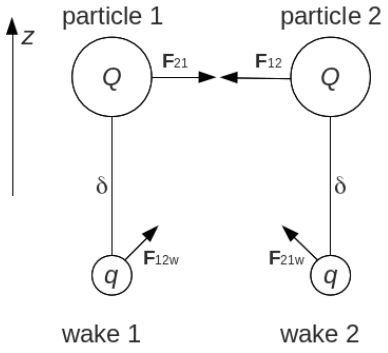

Figure 1.3: Illustration of Yukawa/point-wake model for two microparticles (charge Q) with their wakes (charge q, vertical extent δ). $\mathbf{F}_{12,21}$ and $\mathbf{F}_{12w,21w}$ denote the reciprocal particle-particle and non-reciprocal particle-wake interaction forces, respectively. The vertical axis z is along the ion flow.

The main observable feature of MCI is the upper hybrid modes spectral density[26]. The latter is governed by the modes maximum growth rate which is proportional (for given κ and Ω_{conf}) to the (normalized) wake dipole moment $\tilde{q}\tilde{\delta}$ ($\tilde{q} = q/Q$, $\tilde{\delta} = \delta/\lambda$). This fundamental quantity remains essentially arbitrary in the framework of Yukawa/point-wake model. However, the wake potential and its multipole expansion are determined by the plasma fluxes toward the grain and hence by ion-neutral collisions (compare Sec. 1.2). Therefore $\tilde{q}\tilde{\delta}$ has to be a function of the corresponding parameters. I study this problem in Sec. 2.2.

The latest MCI-investigations [89–92] *presume* that the magnitude of wake dipole moment is small ($\tilde{q}\tilde{\delta} \ll 1$). This corresponds to relatively small ion-flow velocities ($M_T \lesssim 1$) and quasi-isotropic screening. Both points are not met in most ground-based complex plasma experiments. A rigorous analysis for *arbitrary* $\tilde{q}\tilde{\delta}$ is carried out in Sec. 2.3, answering fundamental questions about the modes polarization and associated particle trajectories.

[24]It should be noted that the coupling of acoustic "shear" in-plane and out-of-plane modes does not result in hybridization, but simple mode-crossing [92].

[25]The corresponding decay and growth rates have the same modulus.

[26]Defined as one-particle kinetic energy per unit wave vector and unit frequency.

Chapter 2

Cumulative thesis

This cumulative thesis consists of three papers. They are reprinted in Sec. C with permission from American Institute of Physics (AIP) and the American Physical Society (APS):

- M. Lampe, T.B. Röcker, G. Joyce, S.K. Zhdanov, A.V. Ivlev and G.E. Morfill, *Ion distribution function in a plasma with uniform electric field*, Phys. Plasmas **19**, 113703 (2012). Copyright: AIP.
- T.B. Röcker, S.K. Zhdanov, A.V. Ivlev, M. Lampe, G. Joyce and G.E. Morfill, *Effective dipole moment for the mode coupling instability: Mapping of self-consistent wake models*, Phys. Plasmas **19**, 073708 (2012). Copyright: AIP.
- T.B. Röcker, A.V. Ivlev, S.K. Zhdanov and G.E. Morfill, *Effect of strong wakes on waves in two-dimensional plasma crystals*, Phys. Rev. E **89**, 013104 (2014). Copyright: APS.

In Sec. 2.1, 2.2 and 2.3 the essential objectives, methods and results of the publications mentioned above are summarized.

2.1 Ion distribution function in a plasma with uniform electric field

2.1.1 Objectives

In low-temperature partially ionized plasmas, simple approximations for the ion-velocity distribution function (idf) $f(\mathbf{v})$ are often used to facilitate theoretical analysis. For example, wake field calculations have often been based on an assumed displaced Maxwellian distribution [37,39,102] or on an approximated analytic distribution function [42,51,55,60]. Since the steady-state (mobility-limited) ion distribution function is actually quite different from these simple approximations, a more realistic treatment is called for.

In the paper, analytical and simulation methods and models are used to calculate the idf of a plasma, subject to a uniform electric field $\mathbf{E} = E\hat{\mathbf{e}}_z$ (i.e. the z-axis is orientated

along the electrical field) and the (dominant) charge-exchange collisions (compare Sec. 1.2). Therefore the idf is determined by the balance between acceleration due to the electrical field and ion drag from the charge-exchange collisions.

2.1.2 Methods

Formally, the idf can be obtained by solving the Boltzmann equation with the charge-exchange collision integral depending on the relative speed of the colliding particles. This velocity dependence makes the *exact* problem analytically intractable.

Thus, it is solved by a MC simulation[27]. In the latter a large number of ions ($\simeq 10^6$) with an (initial) Maxwellian distribution, are loaded. Then all of the ions are accelerated over one time step (much smaller than the mean time between charge exchange collisions) by the constant field and conclusively subjected to probabilistic charge-exchange scattering following the null-collision method [103]. This time stepping is repeated until the ion distribution function reaches a steady state. Continuing this over many more steps, the velocities are laid down on a 2D grid to calculate the 2D idf. This MC solution is the "reference" to which I compare all analytical models.

As already mentioned in Sec. 1.2, there exist two *approximate* analytic approaches for idf, the CCF [56] and CMP [51] model:

- In the CCF model a constant collision-frequency is assumed and thus the charge-exchange cross-section is indirectly proportional to the relative velocity of colliders. This implies two notable simplifications: (i) The (integro-differential) Boltzmann equation is reduced to a (first-order) linear differential equation. (ii) The idf separates *exactly* into the product of transverse[28] and longitudinal idfs, $f_\perp(u_\perp)$[29] and $f_z(u_z)$, respectively. This yields $f(\mathbf{u}) = (2\pi)^{-1} \exp(-u_\perp^2/2)\, f_z(u_z)$, where $f_z(u_z)$ can be written in terms of exponential and error functions.

- The CMP model essentially considers the limit of very large thermal Mach numbers. In this case, nearly all the ions have velocities notably larger than the thermal velocity of neutrals. Thus the (Maxwellian) neutral-velocity distribution can be replaced by a Dirac-delta function. Furthermore the model assumes a mobility-limited ion drift with *constant* mean-free path $l = (n_n \Sigma)^{-1}$ (Σ is the *constant* charge-exchange cross-section). The resulting longitudinal distribution contains no ions with negative velocities and is of half-Gaussian form.

The solutions for $f_z(u_z)$ from the MC simulation and both analytical models are compared. Furthermore the reliability of simplifications employed in CCF and CMP models are evaluated. Guided by the corresponding results, an *approximate* model is provided which is valid for *any* value of M_T. The model is based on the following assumptions:

[27] The code by M. Lampe and G. Joyce can be found in the supplementary material of the paper.

[28] with respect to $\mathbf{E}$

[29] The longitudinal and transverse velocities were normalized by the thermal velocity of neutrals, i.e., $u_z = v_z/v_T$, $u_\perp = \sqrt{v_x^2 + v_z^2}/v_T$, respectively.

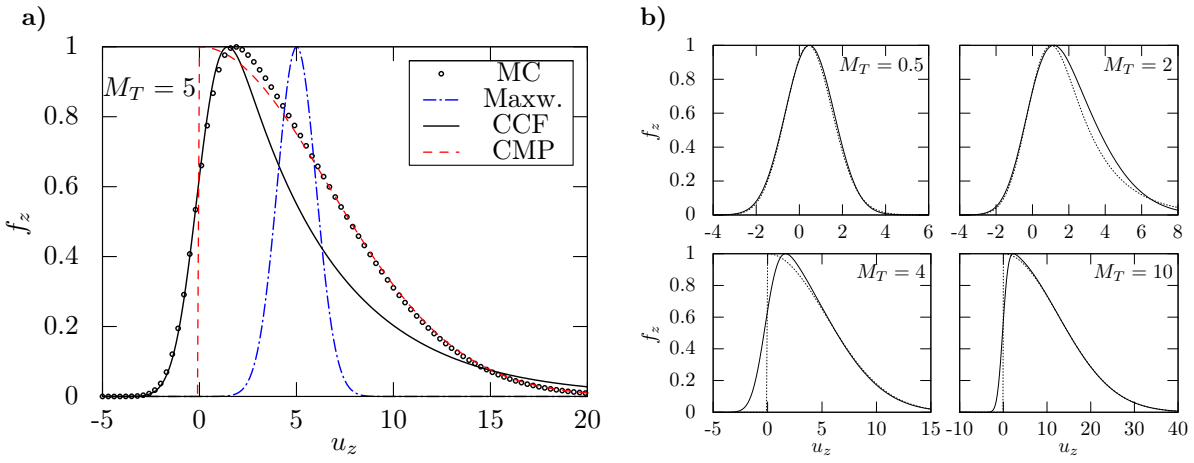

Figure 2.1: a) Review of different models for the longitudinal ion-velocity distribution $f_z(u_z)$ at thermal Mach number $M_T = 5$. Solid curve: CCF model [56]; dashed curve: CMP model (large-M_T limit) [51]; dash-dotted curve: displaced Maxwellian distribution; bullets: MC simulations assuming constant cross-section. b) Solid curves: MC distribution functions for $M_T = 0.5$, 2, 4, 10. The dotted curves show the CCF and CMP solutions for $M_T = 0.5$, 2 and $M_T = 4$, 10, respectively. Here and below, all distribution functions are normalized to unity at maximum.

- The charge-exchange cross-section is constant.
- The two-dimensional distribution function factorizes, i.e., $f(\mathbf{u}) = f_z(u_z) f_\perp(u_\perp)$.
- Slowly varying functions are replaced by constants obtained from averaging over a Maxwellian distribution[30].

Incorporating these points, it is possible to reduce the integro-differential Boltzmann equation to a linear ordinary differential equation (ODE) for the longitudinal idf. The latter can be solved numerically. Finally, the accuracy of the approach is evaluated and the aforementioned assumptions are discussed.

2.1.3 Results

Fig. 2.1 shows the longitudinal idf $f_z(u_z)$ obtained from the CCF model, the CMP model and the MC simulations. The MC idf (bullets in Fig. 2.1a), peaking in the thermal region $0 \lesssim u_z \lesssim 2$, has a weakly-shifted Maxwellian curvature and a half-Gaussian shape, left and right of the maximum, respectively. It is noteworthy that there are very few ions in the thermal region and relatively many ions faster than the average velocity, i.e., with $u_z > M_T$.

[30] I.e. a slowly varying $W(u_z)$ is replaced by the constant $\langle W \rangle = \int \frac{du_z}{\sqrt{2\pi}} W(u_z) \exp\left(-u_z^2/2\right)$.

The often assumed shifted Maxwellian (blue dash-dotted curve in Fig. 2.1a) is completely different from the MC results and therefore this way of ion-flow modelling has to be refused (except for environments with $M_T \ll 1$ or in the bulk region of discharge). The analytical models provide a more reasonable representation of the idf. Anyway certain features differ from the MC results:

- In case of CCF model, the corresponding solution has a long exponential tail (instead of a half-Gaussian shape) and therefore the model provides less hot ions. This is a consequence of the assumption of constant collision frequency, which is only accurate for *small* $M_T \lesssim 2$ (upper plane of Fig. 2.1b). Thus, when ions and scatterer atoms have distributions close to Maxwellian, CCF model is reasonable.

- In CMP model, there are no ions with negative velocities. This is related to the assumption of neutral-velocity distribution, which is sharply peaked around zero: All charge-exchange ions are born with zero velocity (inherited from the neutrals), and then are accelerated to positive velocity. Therefore CMP model is only applicable for discharges with very strong ion downstream ($M_T \gtrsim 10$, shown in the lower plane of Fig. 2.1b).

None of the two analytical models provides an accurate reproduction of the MC idf, especially in the important "transfer regime", approximately ranging $2 \lesssim M_T \lesssim 10$.

The approximation of MC idf is much better when using the developed ODE model: The corresponding longitudinal idf[31] is in very good agreement with the MC results for *any* M_T, especially in the transfer regime (compare Fig. 2.2a). The models transverse distribution is simply Maxwellian at approximately the neutrals temperature.

The assumptions made in the derivation of ODE model are found to be reasonable and accurate enough for most practical purposes. The error contributions can be evaluated one by one:

- The idfs obtained for constant and velocity-dependent charge-exchange cross-sections show small differences for large-M_T cases. Anyway, all the qualitative features of the reference are reproduced (maximum error $\simeq 5\%$) when employing constant-Σ (compare Fig. 2.2b).

- The two-dimensional distribution function does not factorize exactly (as in the CCF model), but it separates to a good approximation[32]. The separation becomes exact for very small and large thermal Mach numbers.

- The strategy of Maxwellian-averaging causes a negligibly small error which becomes larger for smaller field strength. Its maximum error is $\simeq 1\%$.

Therefore it can be concluded that the major error contribution comes from the multiplicative approximation.

[31] $f_z(u_z)$ can be expressed in closed integral-form.

[32] The deviation of the "transverse temperature" $T_\perp$ is largest at $M_T \simeq 2$ (about 14%). For very small and large M_T, one obtains $T_\perp \to T_n$.

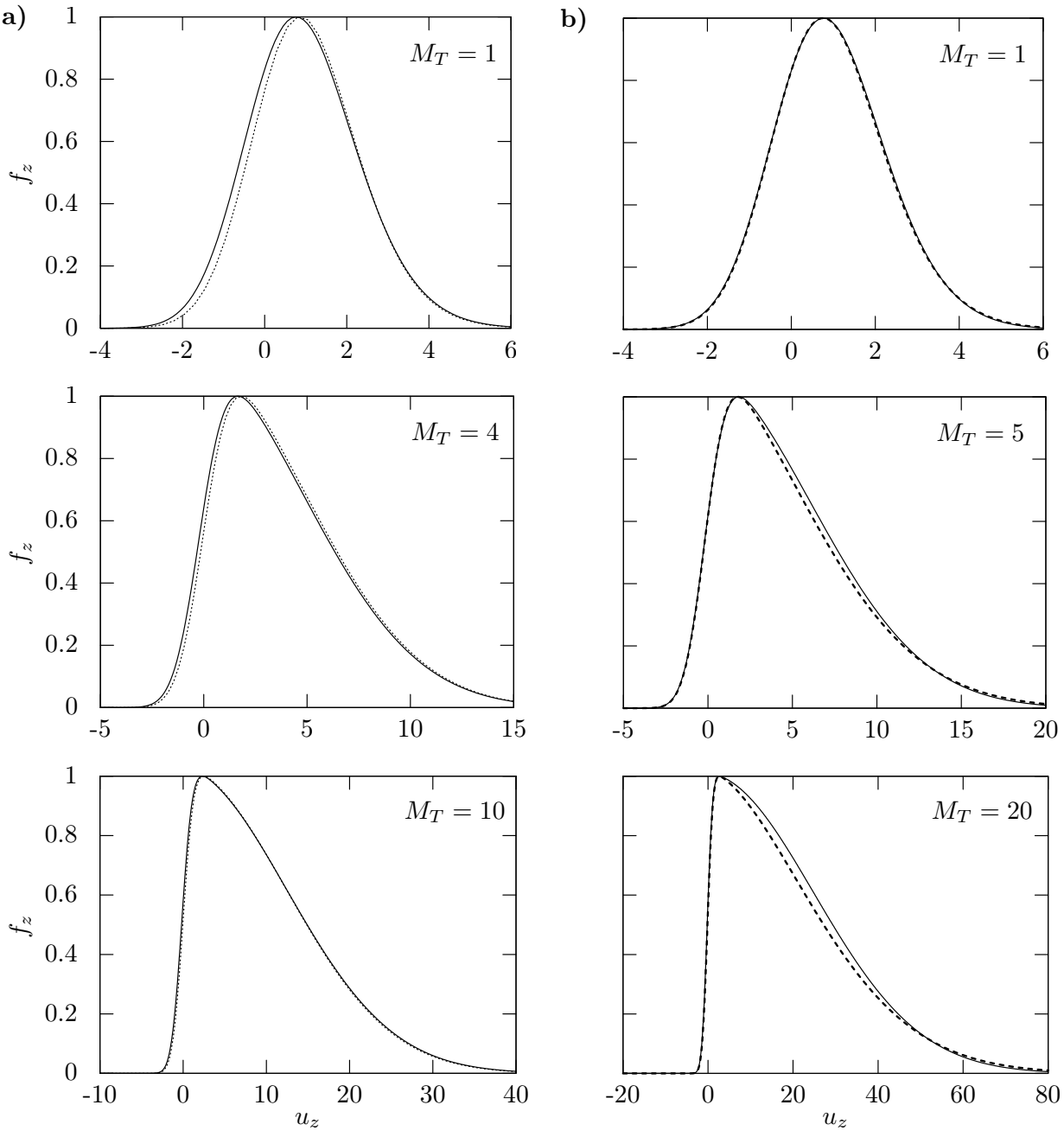

Figure 2.2: Comparison of longitudinal ion-velocity distribution function $f_z(u_z)$ obtained from MC simulations and ODE model, for different values of M_T. The solid lines show the "reference", i.e., the MC results for exact (velocity-dependent) argon cross-section [61]. a) Dotted curves are the ODE model results. b) The dashed lines illustrate the MC results for *constant* cross-section.

2.2 Effective dipole moment for the mode-coupling instability

2.2.1 Objectives

As described in Sec. 1.3, the wake dipole moment $\tilde{q}\tilde{\delta}$ essentially remains arbitrary within the phenomenological "Yukawa/point-wake model" [89–92, 101]. This is a fundamental disadvantage in comparison with experiments, as $\tilde{q}\tilde{\delta}$ determines the spectral density of the hybrid mode, as well as the thresholds of pressure and confinement for MCI onset.

My objective in the paper is the self-consistent generalization of existing MCI theory. The linear dielectric response formalism is applied to kinetic theory of subthermal and suprathermal regimes of ion-flow. The validity ranges of CCF and CMP model for their application in MCI theory have to be evaluated. Finally, I derive the dependence of wake dipole moment on ambient plasma parameters.

2.2.2 Methods

The equations of motion for the i-th grain (mass m), located at position $\mathbf{r}_i = (x_i, y_i, z_i)$ in a vertically confined monolayer with infinite horizontal extent, reads

$$\ddot{\mathbf{r}}_i + \nu_{\mathrm{dn}}\dot{\mathbf{r}}_i + \Omega_{\mathrm{conf}}^2 z_i \hat{\mathbf{e}}_z = \frac{1}{m}\sum_{j\neq i}\mathbf{F}_{\mathrm{int}}(\mathbf{r}_i - \mathbf{r}_j), \tag{2.1}$$

where $\mathbf{F}_{\mathrm{int}}(\mathbf{r}_i - \mathbf{r}_j) = -\nabla\phi(\mathbf{r})|_{\mathbf{r}=\mathbf{r}_i-\mathbf{r}_j}$ is the force on the i-th particle due to *non-reciprocal* pair interaction [i.e. generally $\phi(\mathbf{r}_i - \mathbf{r}_j) \neq \phi(\mathbf{r}_j - \mathbf{r}_i)$] with the neighbor j (the summation is over all particles in the lattice). ν_{dn} is the dust-neutral friction rate, Ω_{conf} is the eigenfrequency of vertical confinement and $\hat{\mathbf{e}}_z$ denotes the unit vector orientated along the ion flow.

Introducing small perturbations $\propto e^{i\mathbf{k}\cdot\mathbf{r}_i - \omega t}$ (wave vector $\mathbf{k}$ and frequency ω) to Eq. (2.1) and subsequently linearising yields the equation

$$\det\left[\mathsf{D}_{\mathbf{k}} - \Omega^2\mathsf{I}\right] = 0. \tag{2.2}$$

$\mathsf{D}_{\mathbf{k}}$ is the dynamical matrix with eigenvalues Ω^2, reading in general form [52]

$$\mathsf{D}_{\mathbf{k}} = \begin{pmatrix} \alpha_x - \beta & \gamma & i\sigma_x \\ 2\gamma & \alpha_y + \beta & i\sigma_y \\ i\sigma_x & i\sigma_y & \Omega_{\mathrm{conf}}^2 - 2\alpha_z \end{pmatrix}, \tag{2.3}$$

and

$$\Omega^2 = \omega(\omega + i\nu_{\mathrm{dn}}), \tag{2.4}$$

respectively. I denotes the unit matrix.

Conceptually, $\mathsf{D}_{\mathbf{k}}$ describes the monolayers elastic response and its entries are determined by the second derivatives of ϕ. $\alpha_{x,y,z}, \beta, \gamma$ are the "dispersion elements", $\sigma_{x,y}$ are

the "coupling elements". The latter make $\mathsf{D}_\mathbf{k}$ non-Hermitian[33] and mimic the influence of particle-wake interactions: $\sigma_{x,y}$ are only *non*-zero in the case of *non*-reciprocal interactions. The coupling elements magnitude is essentially governed by the wake dipole moment. It distinguishes the regimes of "weak" and "strong" coupling, where $\tilde{q}\tilde{\delta}$ is small and large, respectively.

Self-consistent general[34] expressions for dispersion and coupling elements are obtained from the linear dielectric response formalism (see Sec. 1.2). The results essentially depend on the dielectric properties of the plasma, viz., the corresponding permittivity (with contributions from electrons and ions), which in turn incorporates all assumptions of the particular plasma model. For the subthermal and suprathermal regimes of ion-flow, the permittivities from CCF and CMP model are used.

I evaluate the corresponding ranges of validity (in terms of M_T) by comparison of electric fields in CCF and CMP models, $E_{\mathrm{CCF,CMP}}$ respectively, with the field E_{MC}, resulting from the MC simulations (description in Sec. 2.1). Given that $E_{\mathrm{CCF,CMP}} \to E_{\mathrm{MC}}$ for $M_T \to 0$ and $M_T \to \infty$ [51,104], CCF and CMP model are identified to provide acceptable accuracy for Mach numbers with $E_{\mathrm{CCF,CMP}}/E_{\mathrm{MC}} > 90\%$, respectively.

Knowing both models' ranges of validity, "mapping" of self-consistent expressions for $\mathsf{D}_\mathbf{k}$ to the dynamical matrix from the Yukawa/point-wake model [90], provides a straightforward way relating $\tilde{q}\tilde{\delta}$ to the parameters of subthermal or suprathermal ion flow. The mapping procedure essentially stresses the "information" obtained from analysis of experimental spectra: The lower and upper modes dispersion relations $\omega_{\mathrm{lo,up}}$ and the hybrid modes spectral density [91, 92, 106, 107].

Let us elaborate on these points: When Ω_{conf} is notably larger than the threshold upon which hybridization firstly sets in (the "critical confinement" Ω_{cr}), the coupling is negligible and the modes are solely determined by the dispersion elements, reading $\Omega_{\mathrm{h}} = \sqrt{\alpha_x - \beta}$ and $\Omega_{\mathrm{v}} = \sqrt{\Omega_{\mathrm{conf}}^2 - 2\alpha_z}$. Near the onset of hybridization, i.e. for $\Omega_{\mathrm{conf}} \lesssim \Omega_{\mathrm{cr}}$, this holds as well, but *only* under the condition that the coupling is *weak* ($\tilde{q}\tilde{\delta} \to 0$) and *except* for a small vicinity of the wave vector where hybridization occurs first (the "critical wave vector" $\mathbf{k}_{\mathrm{cr}}$[35] or the "critical wave number" $k_{\mathrm{cr}} = |\mathbf{k}_{\mathrm{cr}}|$). Close to $\mathbf{k}_{\mathrm{cr}}$ the lower and upper modes $\Omega_{\mathrm{lo,up}}(\mathbf{k})$ are determined by the equation [90, 92]

$$\Big[\Omega - \Omega_{\mathrm{h}}(\mathbf{k}_{\mathrm{cr}}) - \nabla\Omega_{\mathrm{h}}(\mathbf{k})|_{\mathbf{k}_{\mathrm{cr}}} \cdot (\mathbf{k} - \mathbf{k}_{\mathrm{cr}})\Big]\Big[\Omega - \Omega_{\mathrm{v}}(\mathbf{k}_{\mathrm{cr}}) - \nabla\Omega_{\mathrm{v}}(\mathbf{k})|_{\mathbf{k}_{\mathrm{cr}}} \cdot (\mathbf{k} - \mathbf{k}_{\mathrm{cr}})\Big] + \sigma^2 = 0, \quad (2.5)$$

where σ^2 is essentially governed by $\sigma_{x,y}$ providing coupling between the lower and upper modes[36]. Most important for the mapping procedure, σ^2 is proportional to the hybrid modes growth rate, whose maximum in turn determines the corresponding spectral density.

[33] Note that $\mathsf{D}_\mathbf{k}^* = \mathsf{D}_{-\mathbf{k}}$.

[34] I.e. valid for arbitrary M_T.

[35] Lower and upper modes exactly touch in $\mathbf{k} = \mathbf{k}_{\mathrm{cr}}$, when $\Omega_{\mathrm{conf}} = \Omega_{\mathrm{cr}}$. If the coupling is weak, $\mathbf{k}_{\mathrm{cr}}$ is located near the border of first Brillouin zone. This can be seen from the modes crossing condition $\Omega_{\mathrm{cr}}^2 = \big[\alpha_h - \beta + 2\alpha_v\big]_{\mathbf{k}=\mathbf{k}_{\mathrm{cr}}}$.

[36] The sign in front of σ^2 is negative for coupling of acoustic compression and out-of-plane modes. In such case, the corresponding modes simply cross [92], i.e., no hybridization sets on (compare Sec. 1.3).

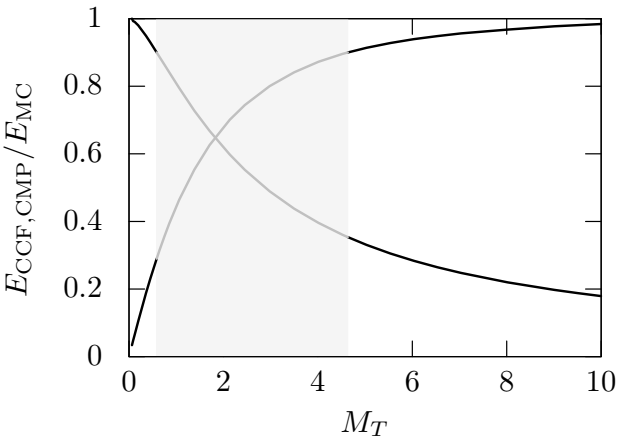

Figure 2.3: The curve tending to unity at $M_T = 0$ represents the ratio of electric fields in CCF model and MC simulations, $E_{\mathrm{CCF}}/E_{\mathrm{MC}}$, at a given M_T. The curve approaching unity at large M_T shows the same, but for CMP model. The shadowed "gray zone" indicates the range of M_T where neither of both analytic models provides acceptable accuracy (more than 10% deviation).

Conclusively, I consider the dynamical matrices from CCF (CMP) and Yukawa/point-wake as being "mapped" experimentally meaningful, when both

- result in the same dispersion relations,
- give the same maximum growth rates for the hybrid modes.

Such mapping is carried out, using the wake dipole moment as "mapping parameter". This procedure finally yields the desired relation between dipole moment and parameters of ambient plasma. It should be noted that the aforementioned points are not considered in a strict sense, but according to experimental accuracy.

Finally, I apply the developed procedure to several experiments (covering a broad range of Mach numbers and screening constants). The corresponding results are compared with the published values for $\tilde{q}\tilde{\delta}$ (when available). This allows the estimation of mapping strategies accuracy.

2.2.3 Results

In the subthermal regime, the "wake contribution" to the plasma permittivity is quite small and therefore the dispersion elements of CCF dynamical matrix practically coincide with the corresponding expressions obtained from Yukawa/point-wake model [90]. On the contrary, the coupling elements are found to be quite different in magnitude. They are expressed in terms of integral exponential functions. From the comparison of electric fields, it can be concluded that the CCF model is applicable for $M_T \lesssim 0.8$ (compare Fig. 2.3).

In the CMP model, i.e. suprathermal regime, both, reciprocal *and* coupling elements of $\mathsf{D_k}$ (expressed in terms of definite integrals containing modified Bessel functions of second kind [105]), significantly change. However, given a proper renormalization procedure for the effective values of Q and λ, the dispersion relations of modes remain the same as in Yukawa/point-wake model, according to typical experimental accuracy [52]. Therefore I conclude that the suggested mapping procedure is applicable for CMP model as well. From Fig. 2.3 it is evident that CMP model is appropriate for $M_T \gtrsim 4 - 5$.

Although in both models the magnitudes of $\sigma_{x,y}$ differ compared to the results from Yukawa/point-wake model, the shapes of the corresponding curves $\sigma_{x,y}(\mathbf{k})$ seem to be comparable. The results of matching the maximum growth rates can be found in Fig. 2.4:

At subthermal ion-flow, $\tilde{q}\tilde{\delta}$ is directly proportional to the thermal Mach number. The κ-dependence[37] can be fitted to good accuracy by a cubic polynomial (double-dashed line in Fig. 2.4a). Things are a little bit more peculiar in the suprathermal regime: Here, the effective screening length λ is proportional to the Mach number and consequently $\kappa = \Delta/\lambda$ and the collision parameter $\zeta = \lambda/l$ are both functions of M_T, which determine $\tilde{q}\tilde{\delta}$ (Fig. 2.4b). In both cases, $\tilde{q}\tilde{\delta}$ practically does not depend on the propagation direction of the wave (differences for propagation along different lattice main axes are typically smaller than 5%).

In Tab. 2.1, three generic experiments are listed, to which the proposed mapping procedure was applied. The mapped dipole moments are found to be in a rather narrow range and they agree very well with the published values. However, for the experiments carried out by Couëdel *et al.* [91, 92] deviations between mapped and published dipole moments are evident. They are related to the fact that Couëdel *et al.* obtained $(\tilde{q}\tilde{\delta})_{\mathrm{pub}}$ by comparing dispersion relations with spectral densities, instead of comparison in terms of the growth rate (as performed by the mapping procedure). In this respect, the fact that the two completely different approaches yield comparable dipole mo-

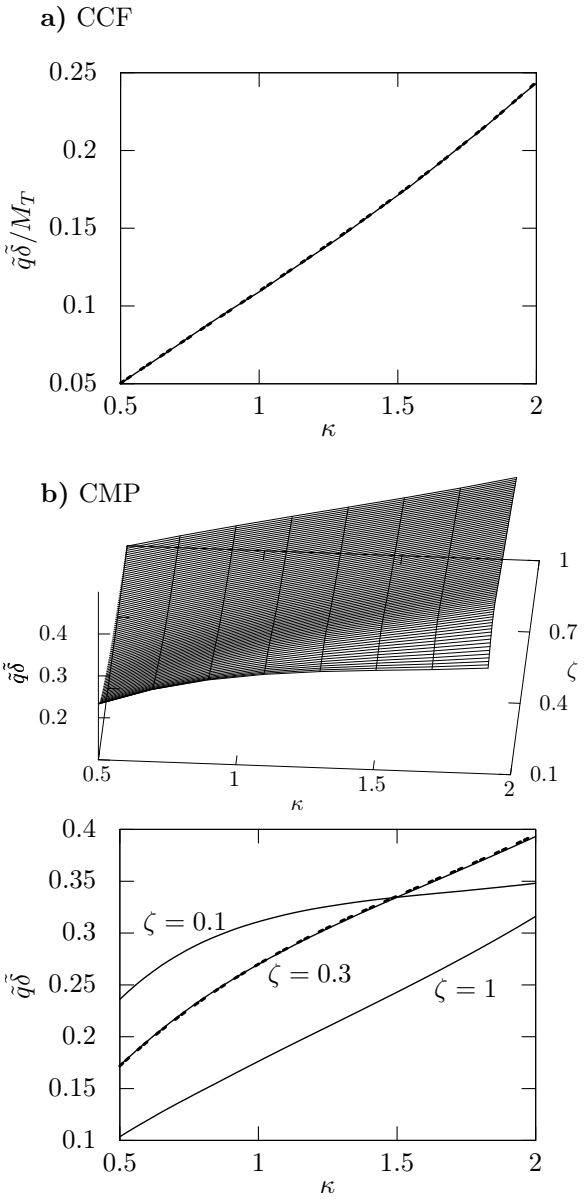

Figure 2.4: a) The wake dipole moment per thermal Mach number $\tilde{q}\tilde{\delta}/M_T$ versus the screening parameter κ. The curve results from CCF model (subthermal regime). b) The dependence of $\tilde{q}\tilde{\delta}$ on κ and collision parameter ζ, obtained from CMP model (suprathermal regime). The double-dashed lines are cubic polynomial fits.

[37] Note, in this regime the effective screening length is practically equal to the local ion-Debye length and thus $\kappa \simeq \sqrt{4\pi e^2 \Delta^2 n_i / T_n}$.

ments can be considered as an acceptable agreement. The bulk of experiments listed in the paper were performed in highly suprathermal regimes $M_T \gtrsim 6$ and thus the dipole moments are notably large ($\tilde{q}\tilde{\delta} = 0.2\text{-}0.3$), indicating strong mode-coupling.

Ref.	p (Pa)	E_0 (V/cm)	ζ	κ	M_T	$(\tilde{q}\tilde{\delta})_{\mathrm{pub}}$	$\tilde{q}\tilde{\delta}$
[101]	2.8	21.7	0.19	1.1	10.3	0.25[b]	0.30
[107][a]	2.67	21.4	0.27	0.79	10.5	0.26	0.24
[91][a]	0.76	20.4	0.06	1.05	19.8	0.1[c]	0.30

[a] Mode-coupling [b] Used in simulations. [c] From fit of fluctuation spectra.

Table 2.1: Three representative monolayer experiments performed in an argon discharge. For each experiment, the gas pressure p and the corresponding levitation electric field E_0 are shown. Both determine the collision parameter ζ, the screening parameter κ, and the thermal Mach number M_T. The last two columns show the wake dipole moments deduced from experiments/simulations, $(\tilde{q}\tilde{\delta})_{\mathrm{pub}}$, and $\tilde{q}\tilde{\delta}$ which is calculated from the mapping procedure.

2.3 Effect of strong wakes on waves in two-dimensional plasma crystals

2.3.1 Objectives

The investigations of coupled DL modes in previous publications essentially assume *weak* particle-wake interactions, represented by a small wake dipole moment [89–92, 101]. In this limit, the modes dispersion, polarization and spectral densities only receive small corrections in a relatively narrow vicinity of the critical wave vector. Furthermore, the hybridization sets in near the border of first Brillouin zone, upon the crossing of uncoupled branches (achieved at the corresponding critical confinement).

As I concluded in Sec. 2.2, $\tilde{q}\tilde{\delta}$ can be fairly large under current experimental conditions, indicating the presence of *strong* mode-coupling. While uncoupled lower and upper wave modes are linearly polarized, the polarization and particle trajectories (associated with the DL waves) of the strongly coupled pendants are fundamental open questions. Moreover, in the regime of strong coupling, the critical wave vector is shifted away from the border of Brillouin zone.

The objective of the paper is to study the regime of strong wake-induced coupling between wave modes in two-dimensional plasma crystals. Weak and strong coupling regimes are compared, pointing out the essential differences. After that, I investigate the characteristic features of strong coupling near the hybridization point. In particular: The modes polarizations, the individual particle trajectories, the mode spectral densities and the shifts of critical wave number and critical confinement.

2.3.2 Methods

Previous publications neglect investigation of the lower hybrid mode [89, 90, 92]. This is a reasonable approximation to reality, as the mode is rapidly decaying and thus its contribution to experimental results, e.g. spectra, is minor. However, in order to provide a consistent theory and predict characteristic features of strong coupling quantitatively accurate, I consider *both* hybrid modes in the paper.

I consider weak dust-neutral friction, which is the typical situation for experiments. On the other hand, the damping should be sufficiently strong to suppress the MCI. This ensures that the kinetic temperature can reach a steady-state level, which is low enough to keep the crystalline order. Yet, the temperature is high enough, so that the hybrid modes can still be observed in experiments. Considering Eq. (2.4), this yields

$$\omega \simeq \Omega - i\frac{\nu_{\mathrm{dn}}}{2}, \quad \nu_{\mathrm{dn}} > 2\eta, \tag{2.6}$$

where η denotes the maximum growth rate of hybrid modes.

The paper studies the particular case of waves propagating along the principal lattice axis for which the mode coupling is most efficient. This assumption does *not* restrict generality for the following reasons:

- All features of the MCI can be observed for waves propagating along the principal lattice axes [90].
- Eq. (2.2) has the same form for $\mathbf{k}$ along *any* principal lattice axis.
- Experimentally, the particle motion is tracked in a freely selected plane. The latter is determined by $\mathbf{k}$ and the vertical coordinate z [91, 111].

The dynamical matrix [and consequently Eq. (2.2)] simplifies notably: The elements γ and σ_y are equal to zero and consequently the in-plane acoustic "shear" mode becomes exactly decoupled[38] from lower (acoustic "compression") and upper (optical out-of-plane) modes. The simplified version of dynamical matrix (2.3) reads[39]

$$\mathsf{D} = \begin{pmatrix} \Omega_{\mathrm{h}}^2 & i\sigma_x \\ i\sigma_x & \Omega_{\mathrm{v}}^2 \end{pmatrix}. \tag{2.7}$$

The entries of the matrix (2.7) are obtained from Yukawa/point-wake model [89], assuming $\tilde{q}\tilde{\delta} = 0.21$ (as suggested in Sec. 2.2). For such magnitude of dipole moment, mimicking strong coupling, the entries of matrix (2.7) differ notably from the corresponding terms obtained in the limit $\tilde{q}\tilde{\delta} \to 0$ ("wake-free" regime).

The dispersion relations of strongly coupled modes near the onset of hybridization ($\Omega_{\mathrm{conf}} \gtrsim \Omega_{\mathrm{cr}}$) are derived from Eq. (2.2) and compared to the wake-free results.

[38] In this case, $\sigma \equiv 0$ when Eq. (2.5) is evaluated for the in-plane shear and out-of-plane modes.
[39] In the paper, the notation $\sigma \equiv \sigma_x$ is used.

From the eigenvalues [Eq. (2.6)] and eigenvectors of the matrix (2.7), I calculate the expressions for propagating wave modes. Their polarizations are conveniently characterized by the "circularity" ϵ: For linearly and circularly polarized wave modes, the circularity is 0 and 1, respectively, $0 < \epsilon < 1$ stands for elliptical polarization. The corresponding Lissajous ellipses illustrate all these results.

In experiments investigating DL wave modes, the main observables are the tracked particle positions. The particle motion associated with the waves is damped due to dust-neutral friction and triggered by thermal noise. While damping was already considered in the macroscopic Newtonian dynamics [viz. *determined* particle trajectories, expressed by Eq. (2.1)], noise is a *microscopic stochastic* process which requires the treatment of Brownian dynamics [7, 110]. The conclusive particle trajectories are the result of both dynamics simultaneously evolving. Therefore, I use the Langevin equation, assuming an uncorrelated stochastic excitation force (Gaussian white noise [97, 108, 110]) acting on each particle. The latter is defined by its first two stochastic moments obtained from the fluctuation-dissipation theorem (at the relevant kinetic dust temperature[40]). The moments determine the magnitudes of wave modes amplitudes in steady state (friction, on average, is balanced by thermal noise and the hybrid modes growth is saturated).

Consequently, I apply the inverse Fourier transform to the steady-state expressions for the wave modes and obtain the individual particle trajectories. They can be regarded as a "weighted" superposition of corresponding Lissajous ellipses. Areas, in which the particle resides most of a typical observation time span[41], are visualized by enclosing "orbitals". Their major axes are obtained by the following procedure: The wave modes' amplitudes are averaged over wave number and the resulting constants are dragged out of the inverse Fourier transforms integral. The remaining integral expression, modulating the amplitude (and containing only cosine- and sine terms), is treated as a phase distribution over time. The product of its standard deviation and the averaged amplitudes define the orbitals major axes.

Furthermore, the perturbations obtained from the Langevin equation and the fluctuation-dissipation-theorem govern the Fourier-transformed particle velocities. They are used to represent the average kinetic energy. Its derivative with respect to wave vector and frequency yields the modes spectral densities[42] (dimensionality $\mathrm{J{\cdot}cm^2{\cdot}s}$).

In the last section, the shifts of critical wave number Δk_{cr} and critical confinement $\Delta\Omega_{\mathrm{cr}}$ are numerically calculated from a pair of coupled non-linear equations.

2.3.3 Results

Fig. 2.5 shows the a) dispersion relations and circularity ϵ, b) longitudinal and transverse spectral densities, c) Lissajous ellipses, d) particle trajectories and corresponding orbitals of strongly coupled modes ($\tilde{q}\tilde{\delta} = 0.21$). All plots demonstrate results for typical $\kappa = 1$.

[40] The relevant temperature is determined by T_n and mechanisms of individual dust heating due to delayed charging and charge fluctuations [23, 25, 82]. Compare Sec. 1.2.

[41] Typically some seconds.

[42] Sometimes referred as "fluctuation wave spectra" [91, 106, 107, 111].

The left column, $\Omega_{\rm conf} = 6$, shows the case of separate modes (hybridization is suppressed by strong vertical confinement). In the right column, the hybrid mode is formed due to subcritical confinement $\Omega_{\rm conf} = 5.66 < \Omega_{\rm cr}$. Wave numbers and *all* frequencies are normalized by Δ and $\sqrt{1-\tilde{q}}\,\Omega_{\rm DL}$, respectively. In the following, the results (a-d) are discussed one-by-one.

In Fig. 2.5a) undamped modes[43] were considered for simplicity. The dashed lines show the dispersion relations of uncoupled modes (i.e. in the limit $\tilde{q}\tilde{\delta} \to 0$), the colored lines are the same for the strongly coupled modes. Decreasing the vertical confinement (or correspondingly increasing the wake dipole moment), the modes are flattened ("attraction effect"). The flattening becomes more and more constricted before the modes finally touch, the lower and upper hybrid modes are formed and $\Omega(k)$ becomes imaginary: The critical point of strongly coupled modes is reached far before their crossing. The hybridization can be considered as a non-equilibrium second-order phase transition, where the imaginary part of $\Omega(k)$ is the proper order parameter.

The color-coding in the dispersion relations illustrates the circularity ϵ determining the modes polarizations: For $k \ll 1$, as well as for k near the border of the first Brillouin zone, the separate modes polarizations are linear, i.e. $\epsilon \to 0$. For $k \simeq k_{\rm cr}$, the circularity becomes significant and the polarization is essentially elliptical. At the points where upper and lower separate branches merge and form the hybrid branch, the modes are circularly polarized ($\epsilon = 1$). In between those, the hybrid modes are always elliptically polarized. Furthermore, upon the crossing of horizontal and vertical branches, the polarization of hybrid modes becomes linear near the intersection.

Fig. 2.5b shows the longitudinal and transverse steady-state mode spectral densities $I_{\rm l,t}(k,\omega)$ for $\nu_{\rm dn} = 0.3$, respectively. Remarkably, $I_{\rm l}(k,\omega)$ of the separate modes does not only show a bright longitudinal, but also a weak transverse component, and vice versa for $I_{\rm t}(k,\omega)$. Qualitative interpretation of these results is straightforward: The mode polarization changes between linear and elliptical, and therefore we find the "weak" components varying between zero and their peak brightness. The latter is smaller than the density of "strong" components, since the modes are still separated. The hybrid branch has equal longitudinal and transverse spectral densities, where the relative contribution of the lower hybrid mode to the total spectral density is relatively small due to its decay. The spectral density distribution along the hybrid branch can be slightly asymmetric (with respect to the center) which may be important for the analysis of high-resolution spectra. The spectral density is in units of $\sqrt{3}\Delta^2\nu_{\rm dn}T_d/[16\pi^3(1-\tilde{q})\Omega_{\rm DL}]$.

The Lissajous ellipses, Fig. 2.5c, visualize the essential difference between separate and hybrid wave modes, $\mathbf{w}_{\rm lo,up}$ and $\mathbf{w}^{\rm (hyb)}_{\rm lo,up}$, respectively, in terms of polarization: In the separate regime (left column), their major axes are orientated along the coordinate axes, which is particularly not true for Lissajous ellipses of lower and upper *hybrid* modes (right column): These are rotated by 45° with respect to the axes of separate modes (but remaining mutually orthogonal)[44]. The rotation occurs discontinuously at the merging points (where

[43] $\nu_{\rm dn} = 0$ and consequently $\Omega_{\rm lo,up} = \omega_{\rm lo,up}$, as follows from Eq. (2.6).

[44] The hybrid modes equal longitudinal and transverse spectral densities follow from the 45°-rotation.

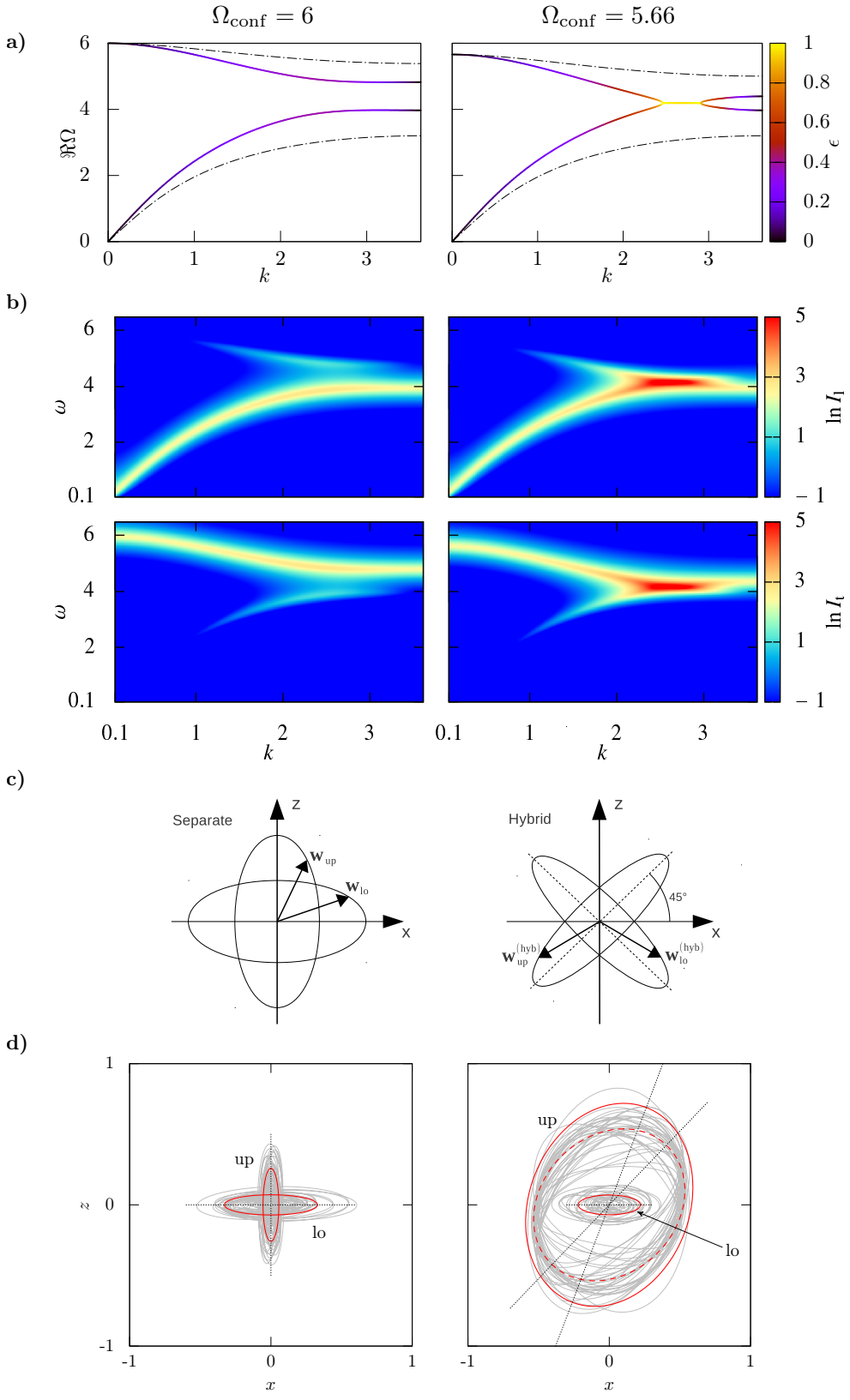

Figure 2.5: Effects of strong-wake induced coupling.

the degenerate modes are circularly polarized). The shape of ellipses is determined by the circularity ϵ: For $\epsilon = 0$ they degenerate into lines, for $\epsilon = 1$ a circle is formed. The illustration is for $\epsilon = 0.5$.

The features of the Lissajous ellipses are reflected by the characteristic ellipsoid-shaped single particle trajectories. I obtain them for the experimental typical observation interval $\simeq 3$s [92, 112]. The trajectories are indicated by the grey lines in Fig. 2.5d. The red solid-line ellipses are the corresponding orbitals[45]. In the separate regime, the orbitals major axes (straight dotted lines) are along the coordinate axes. In the hybridized regime, the major axis for the (decaying) lower mode is practically horizontal, while for the (growing) upper mode it is rotated by $\simeq 70°$. This is due to the fact, that the trajectories are a "superposition" of ellipses oriented along the coordinate axes and those rotated by 45° (shown by the dashed-line ellipse). The hybrid branches are formed within a relatively small region of Brillouin zone (compare right column of Fig. 2.5a), yet the amplitude of the upper branch can be increased significantly, while for the lower branch it is reduced. All this governs the size and orientation of the corresponding orbitals: The lower orbital is practically horizontal and its size is similar to the one in the right plane of Fig. 2.5d, since the amplitude for the lower hybrid branch is too small. Hence, the separate branch provides the major contribution here. Contrary, the upper orbital is large and rotated by an angle notably smaller than 90° (but larger than 45°), since the major contribution in this case comes from the enhanced hybrid branch (the corresponding orbital is indicated by the dashed-line ellipse). x and z are in arbitrary units (compare discussion in App. A).

The functional dependence of the shifts of the critical point $\Delta k_{\rm cr}$ and the critical confinement $\Delta\Omega_{\rm cr}$ on the wake parameters $\tilde{q}$ and $\tilde{\delta}$, is found to be governed by the competition of two effects: (i) Increase of the dipole moment makes the "mode attraction" stronger, which causes the shifts to *increase*. (ii) Increase of the wake length $\tilde{\delta}$ weakens the screened wake-particle interaction, which forces the shifts to *decrease*. As a result, both shifts are small in cases of small ($\tilde{q}\tilde{\delta} \to 0$) and large ($\tilde{q}\tilde{\delta} \gtrsim 0.3$) wake dipole moments, and acquire their maxima at intermediate values of $\tilde{q}\tilde{\delta}$. Though $\Delta k_{\rm cr}$ and $\Delta\Omega_{\rm cr}$ essentially follow the same trends, their magnitudes are completely different: While the critical confinement practically remains the same (maximum relative difference $\simeq 2\%$), the onset of hybridization can be significantly shifted toward smaller wave numbers (the magnitude of the effect can be as high as $\simeq 15\%$), i.e., the shift of the hybrid mode should be revealed in experiments.

[45] Due to strong vertical confinement the vertical extent of the upper-mode orbital is somewhat smaller than the horizontal size of the lower-mode orbital.

Chapter 3

Conclusion and future work

Ground-based complex plasmas are often subjected to electric fields making the grain screening highly anisotropic. The particles levitate in the sheath electric field, the region of very strong ion-flow. Therefore the ion-velocity distribution function (idf) is of fundamental importance. Previous investigations of the problem considered only subthermal and strongly suprathermal regimes [42, 51] and thus experimental conditions with *intermediate* ion-flow velocity were *not* addressed.

In the first part of my thesis I provided a self-consistent solution for this problem. The developed model inherits two advantages, compared to the former theory: (i) The analytical model can be applied to a wide range of problems in complex plasmas, dealing with very different strength of ion downstream. (ii) The approximative solution for idf is numerically very efficient. Yet the results are reasonably accurate for most practical purposes.

Plasma crystals in anisotropic ion-flows are non-Hamiltonian systems, i.e., the dust grains exchange energy with the ambient plasma. Energy absorption can result in the primary complex plasma-specific melting process, the mode-coupling instability (MCI).

In the second part of my thesis, I suggested a mapping procedure relating the fundamental quantity in MCI-theory - the wake dipole moment - to the ambient plasma parameters. The dipole moment governs the main experimental observable of MCI, the hybrid modes intensity, as well as the thresholds of confinement eigenfrequency and screening parameter for instability onset. Thus the results are of practical importance for analysis of experimental data and purposeful design of next-generation MCI-dedicated experiments.

Previous publications studying the MCI presume that coupling results in small corrections to the modes. This corresponds to the regime of *weak* coupling reflected by infinitesimally small dipole moment. In this regime, the polarizations of separate modes and corresponding particle trajectories essentially remain linear.

In several of current experiments dealing with MCI, the magnitudes of wake dipole moment are rather large. This indicates the presence of *strong* mode-coupling which was never studied systematically before.

In the thesis' third part, I rigorously investigated essential features of strongly-coupled modes (dispersion relations and spectral densities). The fundamental questions about

the modes polarization and corresponding particle trajectories at the coupling onset were answered. Moreover, theoretical curves demonstrating the shift of coupling onset allow experimenters to easily identify the magnitude of coupling strength from measured spectra. To my best knowledge, this direct relation between the experimentally observable MCI-onset and principal characteristics of plasma wakes was never demonstrated before.

Succeeding the thesis' investigations is in progress, mainly on the following points:

- The suggested analytical model for the ion-velocity distribution function has to be applied to calculations of wake-field structures. This will result in a reasonably accurate, self-consistent model for the *grain interaction potential*, essentially valid at *arbitrary* strength of ion-flow. Such considerations are especially important for conditions where none of the present kinetic models [42,51] is applicable. Comparison with the Monte-Carlo wake-field calculations will serve for the evaluation of models accuracy.

- The effects of strong coupling, especially particle trajectories and spectral densities, have to be experimentally revealed by observation of particle motion and analysis of high signal-to-noise ratio spectra.

- Monolayers are not completely flat, but slightly bend under experimental conditions [101]. It is believed that this is caused by the attractive part of wake field. The effect requires careful investigation.

While the previous points can be elaborated using the framework of my thesis, I summarize further open questions which go beyond:

- The charge-exchange collisions are the dominant process in terms of ion-velocity distribution. Other collision types (e.g. Coulomb collisions, kinetic scattering) cause only minor corrections to the distribution function [54]. However, the charge exchange was treated in idealized form: It was assumed to take place *instantaneously*, i.e., the "collision time" is infinitesimally small. Accounting the real case of *finite* collision time may result in qualitatively new effects, e.g., energy transfer between longitudinal and transverse velocities.

- The electron response was neglected. As shown in experiments and simulations [47–50], the often assumed Boltzmann response is not appropriate. The real situation is further convoluted by the alternating rf-field. The problem of electron response can be self-consistently treated by coupling the kinetic equation for electrons to the Poisson equation. Together with the kinetic equation of ions, high computational effort is required. The solvability with desired accuracy and in reasonable calculation time is at least questionable.

- A constant electric sheath field was assumed. For experiments, this can be interpreted as the averaged field strength at the grains levitation height. However, the (pre)sheath is vertically highly inhomogeneous. Considering this effect requires

sheath modelling. Under certain conditions, the inhomogeneity can modify the wake dipole moment [113].

- The theory of MCI is essentially linear, i.e., the perturbations of particle positions are assumed to be small. While this is true at the instability onset, experiments show that during the evolution of MCI, the growth of kinetic energy steepens when the perturbations are rather large [114]. The steepening cannot be explained from linear theory, which indicates that at the *non-linear* stage another heating mechanism is working.

Appendix A

Unit scale of particle trajectories

Due to the linearity of Eq. (2.2), the unit scale of eigenvectors of $\mathsf{D}_{\mathbf{k}}$ remains arbitrary. However, the unit scale ζ_0 of perturbations $\tilde{\boldsymbol{\zeta}}$ and corresponding particle trajectories can be obtained from Langevin theory. ζ_0 is essentially determined by the Fourier transform of random acceleration (spatial components denoted by p)

$$a_p(\mathbf{k},\omega) = \sum_{m,n} \int dt\ e^{-i(\mathbf{k}\mathbf{s}-\omega t)} a_p(\mathbf{s},t). \tag{A.1}$$

The fluctuation-dissipation-theorem yields for the (squared) average of Eq. (A.1) the expression

$$\langle a_p(\mathbf{k},\omega) a_q^*(\mathbf{k}',\omega')\rangle = 2\delta_{pq}(v_d\Omega_{\mathrm{DL}})^2\nu_{\mathrm{dn}} \sum_{m,n} \int dt \exp -i[(\mathbf{k}-\mathbf{k}')\mathbf{s} - (\omega-\omega')t], \tag{A.2}$$

where $v_d = \sqrt{T_d/m}$ is the "thermal dust velocity", $\mathbf{s}(m,n) = \frac{1}{2}\left[\sqrt{3}m, m+n\right]$ are the equilibrium positions of particles and the summation is over all integers except $(m,n) = (0,0)$. Wave vectors are normalized by Δ, *all* frequencies (except for the dust-lattice scale) and time t by Ω_{DL} and its inverse, respectively. For the integration over $\mathbf{k}$, the wave vectors from the first Brillouin zone have to be considered[46].

Using Eq. (A.2), one obtains the length scale

$$\zeta_0 = \frac{\sqrt{2\nu_{\mathrm{dn}}}v_d}{\Omega_{\mathrm{DL}}}. \tag{A.3}$$

[46]The $\mathbf{k}$-integral can be conveniently expressed by multiple integration over the irreducible part of Brillouin zone $\int_0^{2\pi/(\sqrt{3})} dk_x \int_0^{\sqrt{3}k_x} dk_y$ [115].

Appendix B

Effect of finite particle number

In Sec. 2.2 and 2.3 a monolayer with infinite horizontal extent, i.e. constant interparticle separation, was assumed. A *real* crystal is comprised of a large, yet *finite* number of particles and its density is notably *decreasing* with respect to the centre.

The decrease of density can be neglected in studies of MCI, as the latter evolves at small scales and hence, even small areas with practically constant density, containing several particles, could be quite representative. Typically, observations are performed at the central area of monolayer.

To study the effect of finite particle number, I performed Molecular Dynamics (MD) simulations of an one-dimensional string[47] comprised of n particles. The essential features of these simulations are:

- The particles can move along and perpendicular to the string.
- The particles are horizontally and vertically confined by two fixed charges at the strings ends and a parabolic potential (with eigenfrequency Ω_{conf}), respectively. Therefore the (averaged) particle density remains constant.
- Each particle interacts only with its next neighbors. The interaction is of Yukawa/point-wake type.
- The string is coupled to a Langevin heat bath. The resulting stochastic noise is on average balanced by friction [116–118].
- The equations of motion are solved by Verlet or Beeman algorithms [119–121].
- The resulting time-energy curves (Fig. B.1 shows an example for $n = 8$) are smoothed by the Friedman-Schwarz "Super Smoother" [122, 123].
- In order to find the systems resonance frequencies, Ω_{conf} is used as control parameter (similar to experiments): Starting from a stable configuration, Ω_{conf} is gradually

[47] *Qualitatively*, the essential features of MCI in 2D crystals can be obtained from investigation of an one-dimensional string with next-neighbor interactions [89, 92].

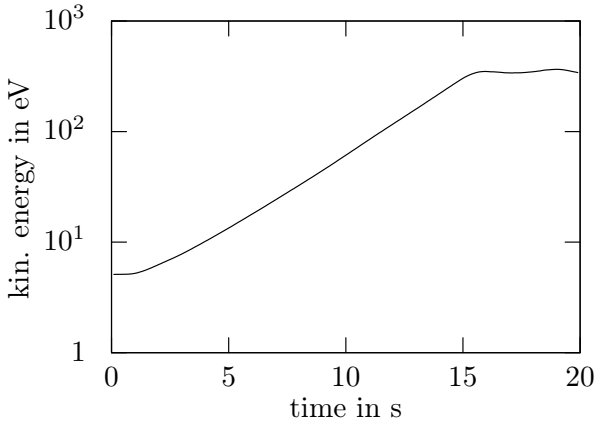

Figure B.1: Exponential increase of kinetic energy at a resonance associated with mode-coupling. The example was obtained for a string of eight particles.

decreased, until either an exponential energy increase occurs or the magnitude of interparticle separation changes (corresponding to a melted string).

Simulations with $n = 2 - 40$ particles were carried out. Each shows the same result: For a *finite* string, only a *finite* number of resonance frequencies exist. This number is equal to the particle number. In this case the hybrid branch [in the (k, ω)-plane] is *not* continuous, but consists of single points. For $n \simeq 40$ it is found to be quasi-continuous.

Below, the code of MD simulation - written in the high-level interpreter language Octave - is given:

```
%MD simulation of a 1D particle string with wakes
%Version from 12/13/2013
%Langevin heat bath implemented in noise.m
%horizontal and vertical parabolic confinement in conf.m
%additional vertical confinement with two fixed charges Qfix
%horizontal y-motion switched off
%next-neighbor Yukawa/point-wake model for
%direct interaction implemented in fyuk.m
%particle-wake interaction implemented in fyukw.m
%time-energy curves smoothened by Friedman-Schwarz super smoother

%global variables
global ga; %damping rate
global M; %particle mass in grams
global Q; %charge of free particles in esu
global la; %effective screening length in cm
global q; %wake charge
global de; %wake length
global h; %timestep
global fh; %horizontal confinement freq
global fv; %vertical confinement freq
```

```
global lp; %position of left fixed particle
global rp; %position of right fixed particle
global temp; %thermostat temperature in erg
global Qfix; %charge of fixed particles

%input simulation parameters
nof = 3;  %number of free particles
nop = nof + 2; %total number of particles to simulate
t0 = 0; %starting time in sec
t1 = 20; %ending time in sec
N = 2000; %time steps
h = (t1-t0)/N; %timestep
cas = 2; %select algorithm: 1 Beeman, 2 Verlet
s = 1;  %switch: 0=thermal noise off, 1=thermal noise on
fh = 0; %hor conf freq, here switched off
fv0 = 55; %lower limit of vert conf freq
fv1 = 120; %upper limit of vert conf freq
fvsteps = 150; %conf freq steps
derthr = 2.5; %slope threshold for kinetic energy
wndw = 10; %averaging interval in grid steps

%modified by simulation
cp = 0; %control parameter to terminate upon a res is found
sp = 1; %1=no resonance, 0=resonance occured
typ = 0; %1=interparticle dist > 3*r0, 2=exp. energy increase
cdm = -1; %stores max interparticle dist after resonance

%physical parameters
M = 6.1*10^(-13) * 1000;
Q = 15200 * 4.8032*10^(-10);
la = 400 * 10^(-6) * 100;
temp = 300*1.3806488*10^(-16);
qt = 0.1;
dt = 0.1;
ga = 0.1;

%calculate some quantities
dl = sqrt(Q^2/(M*la^3));  %dust lattice freq scale
q = qt*Q;
de = dt*la;
tvel = M*dl*la; %approximation of thermal velocity magnitude
r0 = la; %desired equlibrium particle distance
```

```
%grids
tspace = linspace(t0,t1,N); %time grid
fvspace = linspace(fv0,fv1,fvsteps); %conf freq grid
Ek = linspace(0.,0.,N); %kinetic energy grid
rspace = zeros(nop,3,N); %positions of free particles
vspace = zeros(nop,3,N); %velocities of free particles
dif = zeros(nop,3,N); %relative distance of free particles

%set start values
for k = 1:nop
rspace(k,:,1) = [(k-1)*r0-(nop-1)/2*la,0,0];
vspace(k,:,1) = [0,0,0];
endfor

%fixed charges
for i=1:length(tspace)
rspace(1,:,i) = rspace(1,:,1);
rspace(nop,:,i) = rspace(nop,:,1);
endfor

%second time step
fv = fv0;
for k = 2:nop-1
noise = nois(temp,ga);
noisev = [noise(4),noise(5),noise(6)];
noiser = [noise(1),noise(2),noise(3)];

vv = vdot(rspace(k,:,1),vspace(k,:,1),rspace(k-1,:,1),rspace(k+1,:,1));

rspace(k,:,2) = rspace(k,:,1) + vspace(k,:,1)*h + 0.5*vv*h^2 + s*noiser;
vspace(k,:,2) = vspace(k,:,1) + vv*h + s*noisev;
endfor

%solving the equations of motion
for j=1:(fvsteps+1)
if(cp==1)
%evaluate the interparticle seperation
for i=1:(length(tspace)-1)
for k=1:nop-1
dif(k,:,i) = abs(rspace(k+1,:,i)-rspace(k,:,i))/la;
endfor
endfor
```

```
res = [a2',Eksmu2'];
res2 = [tspace',Ek'];
s0 = num2str(nof);
s1 = num2str(fv);
s2 = num2str(typ);
dname = sprintf(["data_",s0]);
[fstatus,msg,msg2] = mkdir(dname);
if(status==0)
error('directory could not be created')
endif
fname = sprintf(["./data_",s0,"/kin","_",s1,".csv"]);
fname2 = sprintf(["./data_",s0,"/kin2","_",s1,".csv"]);
pname = sprintf(["./data_",s0,"/kin","_",s1,".ps"]);
dlmwrite(fname, res, "delimiter", ",", "newline", "\n");
dlmwrite(fname2, res2, "delimiter", ",", "newline", "\n");
orient tall;
orient landscape;
lab = ["nof = ",s0," ", "conf = ", s1," ","typ = ", s2, " ", "cdm = ", s3];
tit = sprintf(lab);
semilogy(a2,Eksmu2);
title(tit, "FontSize", 12);
xlabel("time/s", "FontSize", 9);
ylabel("kin. En./eV", "FontSize", 9);
print (pname, "-dpsc");
%error('DONE');

cp=0;
typ = 0;

for k = 1:nop
rspace(k,:,1) = [(k-1)*r0-(nop-1)/2*la,0,0];
vspace(k,:,1) = [0,0,0];
endfor
else
if(j~=1)
for k=2:nop-1
rspace(k,:,1) = rspace(k,:,length(tspace)-2);
vspace(k,:,1) = vspace(k,:,length(tspace)-2);
rspace(k,:,2) = rspace(k,:,length(tspace)-1);
vspace(k,:,2) = vspace(k,:,length(tspace)-1);
endfor
endif
endif
```

```
if(j>fvsteps)
error('lower limit of confinement reached');
endif
fv = fvspace(j);

if(cas==1)%Beeman
for i=2:(length(tspace)-1)
am = zeros(nop,3);
a = zeros(nop,3);

for k = 2:nop-1
am(k,:) = \
vdot(rspace(k,:,i-1),vspace(k,:,i-1),rspace(k-1,:,i-1),rspace(k+1,:,i-1));
a(k,:) = \
vdot(rspace(k,:,i),vspace(k,:,i),rspace(k-1,:,i),rspace(k+1,:,i));
rspace(k,:,i+1) = \
rspace(k,:,i) + vspace(k,:,i)*h + 2/3*a(k,:)*h^2 - 1/6*am(k,:)*h^2;
endfor

for k = 2:nop-1
vpred = vspace(k,:,i) + 3/2*a(k,:)*h - 1/2*am(k,:)*h;
ap = vdot(rspace(k,:,i+1),vpred,rspace(k-1,:,i+1),rspace(k+1,:,i+1));
vspace(k,:,i+1) = \
vspace(k,:,i) + 5/12*ap*h + 2/3*a(k,:)*h - 1/12*am(k,:)*h;

%add noise
noise = nois(temp,ga);
noisev = [noise(4),noise(5),noise(6)];
noiser = [noise(1),noise(2),noise(3)];

vspace(k,:,i+1) = (vspace(k,:,i+1) + s*noisev);
rspace(k,:,i+1) = (rspace(k,:,i+1) + s*noiser);

vspace(k,2,i+1) = 0;
%vspace(k,3,i+1) = 0;
vspace(k,2,i+1) = 0;
%vspace(k,3,i+1) = 0;

rspace(k,2,i+1) = 0;
%rspace(k,3,i+1) = 0;
rspace(k,2,i+1) = 0;
%rspace(k,3,i+1) = 0;
```

```
endfor
endfor
endif

if(cas==2)%Verlet
for i=2:(length(tspace)-1)
for k = 2:nop-1
a = vdot(rspace(k,:,i),vspace(k,:,i),rspace(k-1,:,i),rspace(k+1,:,i));
rspace(k,:,i+1) = 2*rspace(k,:,i) - rspace(k,:,i-1) + a*h^2;
vspace(k,:,i+1) = (rspace(k,:,i+1) - rspace(k,:,i-1))/(2*h);

%add noise
noise = nois(temp,ga);
noisev = [noise(4),noise(5),noise(6)];
noiser = [noise(1),noise(2),noise(3)];

vspace(k,:,i+1) = (vspace(k,:,i+1) + s*noisev);
rspace(k,:,i+1) = (rspace(k,:,i+1) + s*noiser);

vspace(k,2,i+1) = 0;
%vspace(k,3,i+1) = 0;
vspace(k,2,i+1) = 0;
%vspace(k,3,i+1) = 0;

rspace(k,2,i+1) = 0;
%rspace(k,3,i+1) = 0;
rspace(k,2,i+1) = 0;
%rspace(k,3,i+1) = 0;
endfor
endfor
endif

%evaluate kinetic energies
for i=1:length(tspace)
Ek(i) = 0;
for k=2:nop-1
v = vspace(k,:,i);
Ek(i) += 0.5*M*sqrt(v(1)^2);
endfor
Ek(i) = Ek(i)/1.602 * 10^12;
vp(i) = vspace(3,1,i);
endfor
```

```
%averaging of energies
for u=1:((length(tspace)-wndw)/wndw)
a1(u) = 0;
Ekavg(u) = 0;
for w=1:wndw
a1(u) = w+(u-1)*wndw;
Ekavg(u) += Ek(w+(u-1)*wndw)/wndw;
endfor
endfor

%smoothing of energy curves
a2 = a1*(t1-t0)/N;
Eksmu = supsmu(a1,log(Ekavg));
%Eksmu1 = supsmu(tspace,Ek); %alternative smooting
Eksmu2 = exp(Eksmu);
der = diff(Eksmu2)./diff(a2);
a3 = max(der);

for i=1:(length(tspace))
for k=1:nop-1
%check for collisions between particles
if((rspace(k,1,i))>=(rspace(k+1,1,i)))
printf("collision between particles!\n");
exit;
endif

%check for melting
if(abs(rspace(k+1,1,i)-rspace(k,1,i)) > 3*r0)
cp = 1;
sp = 0;
typ = 1;
endif
endfor
endfor

%check for exponential energy increase
if(max(der)>derthr)
cp = 1;
sp = 0;
typ = 2;
for k = 1:nop-1
cd(k) = abs((rspace(k+1,1,N)-rspace(k,1,N)));
endfor
```

```
cdm = max(cd);
s3 = num2str(cdm/la);

if(cdm<2*r0)
if(Eksmu2(length(Eksmu2))<10)
sp = 1
cp = 0
endif
endif
endif

if(j==fvsteps && sp==1)
sp = 1;
cp = 1;
printf("-----------------------------------------------\n");
printf("crystal stable for given parameters\n");
endif

status = j/fvsteps * 100
endfor

function fvdot = vdot(rn,vn,rnm,rnp)
global ga;
global M;
global sigma;
global h;
global Delta;

ynm = fyuka(rn,rnm);
ynp = fyuka(rn,rnp);
ynmw = fyukw(rn,rnm);
ynpw = fyukw(rn,rnp);

co = conf(rn);

fvdot(1) = 1/M*(ynm(1) + ynp(1) + ynmw(1) + ynpw(1) - M*ga*vn(1) + co(1));
fvdot(2) = 1/M*(ynm(2) + ynp(2) + ynmw(2) + ynpw(2) - M*ga*vn(2) + co(2));
fvdot(3) = 1/M*(ynm(3) + ynp(3) + ynmw(3) + ynpw(3) - M*ga*vn(3) + co(3));
endfunction

function ffyuka = fyuka(r1,r2)
global la;
global Q;
```

```
r = sqrt((r1(1)-r2(1))^2+(r1(2)-r2(2))^2+(r1(3)-r2(3))^2);
ffyuka(1) = Q^2/r^2 * exp(-r/la)*(1+r/la)*(r1(1)-r2(1))/r;
ffyuka(2) = Q^2/r^2 * exp(-r/la)*(1+r/la)*(r1(2)-r2(2))/r;
ffyuka(3) = Q^2/r^2 * exp(-r/la)*(1+r/la)*(r1(3)-r2(3))/r;
endfunction

function ffyukw = fyukw(r1,r2)
global Q;
global q;
global la;
global de;

r = sqrt((r1(1)-r2(1))^2+(r1(2)-r2(2))^2+(r1(3)-(r2(3)-de))^2);
ffyukw(1) = -Q*q/r^2 * exp(-r/la)*(1+r/la)*(r1(1)-r2(1))/r;
ffyukw(2) = -Q*q/r^2 * exp(-r/la)*(1+r/la)*(r1(2)-r2(2))/r;
ffyukw(3) = -Q*q/r^2 * exp(-r/la)*(1+r/la)*(r1(3)-(r2(3)-de))/r;
endfunction

function fconf = conf(r)
global M;
global fh;
global fv;
global fx;

fconf(1) = -M*fh^2*r(1);
fconf(2) = -M*fh^2*r(2);
fconf(3) = -M*fv^2*r(3);
endfunction

function fnois = nois(temp,ga)
global M;
global h;

a = ga*h;
cova = temp/(M*ga) * (1-2*exp(-a)+exp(-2*a));
varr = 2*h*temp/(M*ga)*(1 - 2*(1-exp(-a))/a + (1-exp(-2*a))/(2*a));
varv = temp/M*(1-exp(-2*a));
sig = cova/sqrt(varv);

ran1 = [randn,randn,randn];
ran2 = [randn,randn,randn];
norm1 = 1/sqrt(ran1(1)^2+ran1(2)^2+ran1(3)^2);
ran1 = norm1*ran1;
```

```
norm2 = 1/sqrt(ran2(1)^2+ran2(2)^2+ran2(3)^2);
ran2 = norm2*ran2;

fnois(1) = sig*ran1(1) + sqrt(varr-sig^2)*ran2(1);
fnois(2) = sig*ran1(2) + sqrt(varr-sig^2)*ran2(2);
fnois(3) = sig*ran1(3) + sqrt(varr-sig^2)*ran2(3);

fnois(4) = sqrt(varv)*ran1(1);
fnois(5) = sqrt(varv)*ran1(2);
fnois(6) = sqrt(varv)*ran1(3);
endfunction
```

Appendix C

Enclosed papers

Ion distribution function in a plasma with uniform electric field

M. Lampe,[1,a)] T. B. Röcker,[2] G. Joyce,[1,b)] S. K. Zhdanov,[2] A. V. Ivlev,[2] and G. E. Morfill[2]
[1]*Department of Astronomy, University of Maryland, College Park, Maryland 20740, USA*
[2]*Max Planck Institute for Extraterrestrial Physics, 85741 Garching, Germany*

(Received 21 September 2012; accepted 7 November 2012; published online 29 November 2012)

For a homogeneous partially ionized plasma subject to a uniform electric field **E**, several methods and models are used to calculate the distribution function $f(\mathbf{v})$ for ions subject to charge-exchange collisions. The exact solution for $f(\mathbf{v})$, based on the energy-dependent cross section for Ar, is obtained by Monte Carlo (MC) simulation. This is compared to the MC results for $f(\mathbf{v})$, based on either a constant cross section σ or a constant collision frequency ν. The constant-σ model is found to accurately represent $f(\mathbf{v})$ for any value of E, whereas the constant-ν results are qualitatively incorrect for large fields. Under the constant-σ assumption, a simple, easily solvable ordinary differential equation is obtained which reproduces the MC results with good accuracy. © *2012 American Institute of Physics*. [http://dx.doi.org/10.1063/1.4768456]

I. INTRODUCTION

In low-temperature partially ionized plasmas, the ion distribution function $f(\mathbf{v})$ is a measure of fundamental importance, which strongly influences all of the basic characteristics of the plasma,[1] as well as the interaction of the plasma with surrounding surfaces, and in the case of complex (dusty) plasmas, the interaction of the plasma with the dust grains, and the interaction of the grains with each other.[2,3] Thus, a realistic model of the ion distribution function is needed as a precursor to any overall model of plasma properties and processes.[4]

In typical rf and dc laboratory discharges, resonant charge exchange is the dominant ion collision process: The total cross-section for small-angle elastic scattering is comparable to the charge-exchange cross section, but the effect of an elastic collision on ion momentum is very much smaller.[5] Ion-ion Coulomb collisions are usually a small perturbation, except in the highest-density discharges. Thus, when the plasma is subject to an electric field **E** that causes ion flow, the flow velocity and the distribution function are determined by the balance between acceleration due to **E** and drag due to charge-exchange collisions. In this case, $f(\mathbf{v})$ may be very different from a displaced Maxwellian distribution. In situations where **E** is spatially varying $f(\mathbf{v})$ may become non-local.[6] Nevertheless, it is of general interest to determine the ion velocity distribution in the simplest case of a homogeneous plasma subject to a uniform electric field **E**.

Simple approximations for $f(\mathbf{v})$ are often used to facilitate theoretical analysis. For example, wake field calculations in dusty plasma[7–12] have often been based on an assumed displaced Maxwellian distribution at neutral-gas temperature T and thermal velocity $v_T = \sqrt{T/m}$,

$$f(\mathbf{v}) = \frac{1}{(2\pi v_T)^{3/2}} \exp\left[-\frac{(v_z - v_d)^2 + v_\perp^2}{2v_T^2}\right], \qquad (1)$$

where v_d is the mean drift velocity in z-direction (along the field) and $\mathbf{v}_\perp = (v_x, v_y)$ is the transverse velocity. Since the steady-state (mobility-limited) ion distribution function is actually quite different from Eq. (1),[13–16] a more realistic treatment is called for. The next simplest approximation is that the charge-exchange collision frequency ν is constant, i.e., independent of the relative velocity between colliding particles.[17,18] With this approximation, often called the Bhatnagar-Gross-Krook (BGK) model,[19] an analytic solution for the distribution function is possible. Although this solution is more realistic than the displaced Maxwellian, it is still not satisfactory quantitatively, since the assumption of constant ν is not accurate in real gases. Generally, the collision frequency is a function of $|\mathbf{v} - \mathbf{v}'|$, the relative speed between the two colliding particles, and is given by $\nu = n|\mathbf{v} - \mathbf{v}'|\sigma$, where n is the number density of neutrals and σ is the collision cross section. The latter is also a function of $|\mathbf{v} - \mathbf{v}'|$, but the dependence $\sigma(|\mathbf{v} - \mathbf{v}'|)$ for charge-exchange collisions is logarithmically weak[1,20]—e.g., for argon the cross section (in cm^2) is[21]

$$\sigma(|\mathbf{v} - \mathbf{v}'|) = 5.53 \times 10^{-15}(1 - 0.0543 \ln \varepsilon), \qquad (2)$$

where ε is the kinetic energy in eV corresponding to the relative velocity $|\mathbf{v} - \mathbf{v}'|$. Thus, it is a better approximation to assume constant σ rather than constant ν. However, an exact analytic solution for $f(\mathbf{v})$ is not possible with σ given by Eq. (2), or even for the reasonable approximation of constant σ.

This paper deals with the analytic and numerical calculation of realistic steady-state ion distribution functions in a homogeneous plasma flowing under the influence of a uniform electric field and experiencing charge-exchange collisions. In Sec. II, we review the available analytic approximate solutions for $f(\mathbf{v})$. In Sec. III, we present a Monte Carlo (MC) method for calculating $f(\mathbf{v})$ with no approximations and for any specified dependence of $\sigma(|\mathbf{v} - \mathbf{v}'|)$. We compare $f(\mathbf{v})$ for the three cases of constant ν, constant σ, or $\sigma(|\mathbf{v} - \mathbf{v}'|)$ from Eq. (2); the comparison gives an indication of the range of validity of the analytic approximations. In Sec. IV, following

a)martinlampe2@gmail.com.
b)Deceased.

guidelines suggested by the MC results, we develop a simple model that is easily solved and gives accurate approximate solutions for $f(\mathbf{v})$ under the constant-σ assumption. In Sec. V, we summarize our results. In a subsequent paper, we shall apply the results of this paper to the calculation of wake fields around dust grains in flowing plasma, and to the melting of two-dimensional dust crystals.

II. STEADY-STATE ION DISTRIBUTION FUNCTION: ANALYTICAL APPROXIMATIONS

A. Constant-ν approximation: Analytic solution for $f(\mathbf{v})$

For a homogeneous plasma, with ions flowing under the influence of a uniform electric field $\mathbf{E}$ and subject to charge-exchange collisions with a much denser background of neutral molecules, the steady state ion distribution function $f(\mathbf{v})$ is determined by the Boltzmann equation,

$$\frac{e\mathbf{E}}{m}\cdot\frac{\partial f}{\partial \mathbf{v}} = nf_n(v)\int d\mathbf{v}' f(\mathbf{v}')|\mathbf{v}-\mathbf{v}'|\sigma(|\mathbf{v}-\mathbf{v}'|) - nf(\mathbf{v})\int d\mathbf{v}' f_n(v')|\mathbf{v}-\mathbf{v}'|\sigma(|\mathbf{v}-\mathbf{v}'|), \quad (3)$$

where $d\mathbf{v} \equiv dv_x dv_y dv_z$. The neutral molecules, with mass m and density n, are assumed to have a Maxwellian distribution,

$$f_n(v) = \frac{1}{(2\pi v_T^2)^{3/2}}\exp\left(-\frac{v^2}{2v_T^2}\right). \quad (4)$$

It is convenient to use dimensionless velocity variables $\mathbf{u} = \mathbf{v}/v_T$, and to define the "thermal" Mach number $M \equiv v_d/v_T$.

For a general dependence $\sigma(|\mathbf{v}-\mathbf{v}'|)$, or even if σ is a constant, Eq. (3) is analytically intractable because of the factor $|\mathbf{v}-\mathbf{v}'|$ (except for the limiting cases $M \to 0$ and $M \to \infty$). However, under the constant-ν approximation (i.e., when the product $|\mathbf{v}-\mathbf{v}'|\sigma \equiv \nu/n$ can be treated as a constant), Eq. (3) reduces to the Bhatnagar-Gross-Krook form,[19]

$$\mathcal{E}_\nu \frac{\partial f}{\partial u_z} = \frac{1}{(2\pi)^{3/2}}\exp\left(-\frac{u^2}{2}\right) - f, \quad (5)$$

where $\mathcal{E}_\nu = eE/(m\nu v_T)$ is a dimensionless measure of the electric field (pointed in z-direction). Integro-differential equation (3) is thus reduced to an ordinary differential equation, and furthermore $f(\mathbf{u})$ separates into the product of distributions parallel and perpendicular to $\mathbf{E}$,

$$f(\mathbf{u}) = f_z(u_z) f_\perp(\mathbf{u}_\perp), \quad (6)$$

where

$$f_\perp(\mathbf{u}_\perp) = \frac{1}{2\pi}\exp\left(-\frac{u_\perp^2}{2}\right). \quad (7)$$

Equation (5) then reduces to a linear first-order ordinary differential equation for $f_z(u_z)$ which easily yields the exact solution,

$$f_z(u_z) = \frac{1}{2M}\exp\left(\frac{1-2Mu_z}{2M^2}\right)\times\left[1+\mathrm{erf}\left(\frac{Mu_z-1}{\sqrt{2}M}\right)\right]. \quad (8)$$

The mean drift velocity is $v_d = eE/m\nu$, or in dimensionless form, $M = \mathcal{E}_\nu$.

The constant-ν solution (8) is plotted in Fig. 1, for the case $M = 5$. In all of the plots, distributions are shown normalized, so that the peak value is unity. Note that, for this typical high-Mach number case, $f_z(u_z)$ peaks within the thermal region $0 \lesssim u_z \lesssim 2$ but has a long exponential tail. We see that $f_z(u_z)$ is very different from the displaced Maxwellian at the same Mach number, which is also plotted in Fig. 1.

As noted above, the assumption of constant ν is not very accurate in general. But in the regime of small E/n (low Mach numbers), both the ions and the scatterer atoms have distributions that are close to Maxwellian at temperature T, and for the majority of collisions $|\mathbf{u}-\mathbf{u}'|$ lies within the limited range 1 to 2. Thus, in this regime it is a reasonable qualitative model to replace $|\mathbf{u}-\mathbf{u}'|\sigma$ with a constant value obtained by taking an appropriate average over $\mathbf{u}$ and $\mathbf{u}'$, so that the Boltzmann equation reduces to the BGK form Eq. (5), leading to the analytic solution (8).

B. Constant-σ approximation, strong-field limit: Analytic solution for $f(\mathbf{v})$

If σ is assumed to be constant, it comes out of the integrals in Eq. (3), but the integro-differential equation is still intractable because of the factor $|\mathbf{v}-\mathbf{v}'|$. However, in the limit of large E/n (high Mach numbers) nearly all the ions have $v \gg v_T$, and thus $|\mathbf{v}-\mathbf{v}'| \simeq v$. Furthermore, the neutral thermal velocity v_T is much less than the mean ion speed Mv_T, and therefore it is argued that the neutral distribution

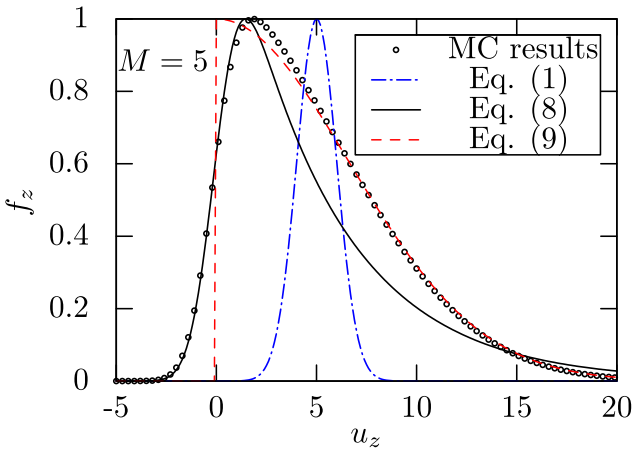

FIG. 1. Comparison of different models for the longitudinal velocity distribution $f_z(u_z)$ at the Mach number $M = 5$. Solid curve: constant-ν analytical solution, Eq. (8); dashed curve: constant-σ analytical solution in large-M limit, Eq. (9); dot-dashed curve: displaced Maxwellian distribution, Eq. (1); bullets: MC simulations for constant σ. Here and below, all distribution functions are normalized to unity at maximum.

function (4) can be replaced by $\delta(\mathbf{v})$. With these simplifications, and again using the dimensionless velocity variable u, the exact solution to Eq. (3) is[4,15,16]

$$f_z(u_z) = \begin{cases} \sqrt{\frac{2}{\pi \mathcal{E}_\sigma}} \exp\left(-\frac{u_z^2}{2\mathcal{E}_\sigma}\right), & u_z > 0, \\ 0, & u_z < 0, \end{cases} \tag{9}$$

where $\mathcal{E}_\sigma = eE/(n\sigma T)$ is a dimensionless measure of the electric field appropriate to the constant-σ case. The constant-σ, large-M-limit solution from Eq. (9) is plotted in Fig. 1, along with the constant-ν solution from Eq. (8). Note that $f_z(v_z)$ from Eq. (9) has a half-Gaussian form rather than an exponential tail, and therefore has more moderate-energy ions, but fewer ions in the high-energy tail. This is because the high-velocity tail is made up of ions which have been accelerated by $\mathbf{E}$ for a very long time, but have had very few scatterings. If σ is constant, the scattering probability increases nearly proportionally to v, so there are fewer of these ions. The distribution (9) includes no ions with negative u_z, because of the assumption that all charge-exchange ions are born with zero velocity inherited from the neutrals, and then are accelerated to positive velocity.

III. MONTE CARLO APPROACH

With a realistic treatment of the scattering cross-section, and outside of the limits discussed above, the Boltzmann equation (3) is intractable analytically, but $f(\mathbf{v})$ is easily calculated by MC simulation. To perform this calculation, we have written a code which proceeds as follows:

- A large number of simulation ions, typically $\sim 10^6$, are loaded with an initial Maxwellian distribution at temperature T.
- A time step Δt is set, which is chosen to be much smaller than the mean time between charge exchange collisions.
- All of the ions are accelerated by the constant field $\mathbf{E}$ over one time step.
- The ions are then subjected to probabilistic charge-exchange scattering. Since the probability of scattering depends on both the initial velocity $\mathbf{v}$ of the ion and the velocity $\mathbf{v}'$ of the scatterer, we use the null collision method,[22] wherein a "maximum collision frequency" $\nu_{\max}$ is chosen, which is larger than the collision frequency of any ion. A fraction of the ions equal to $\nu_{\max}\Delta t$ is then chosen randomly as ions that *may have* scattered during that time step. The scatterer velocity $\mathbf{v}'$ is then chosen randomly off the neutral distribution. At this point we know $\mathbf{v} - \mathbf{v}'$ and therefore the actual collision frequency ν for this collision. We then choose another random number α, uniformly distributed over $0 \le \alpha \le 1$, and if $\alpha < \nu/\nu_{\max}$ we say that a scattering did occur, and reset the ion velocity to $\mathbf{v}'$; if not, the velocity is left at $\mathbf{v}$.
- The time stepping is repeated until the ion distribution function reaches steady state, which occurs over a few mean scattering times.
- We then continue the time stepping for many more time steps, all the while laying down the ion velocities on a 2D $(v_z, v_\perp)$ velocity grid to calculate the distribution function. Averaging over $\sim$1000 time steps, which requires about 1 min on a single-processor PC, gives good generally smooth 1D distributions (averaged over either v_z or $v_\perp$); for low-noise 2D distribution functions, we use about ten times as many time steps ($\sim 10^{10}$ particles $\times$ timesteps).

As a test of the validity of the MC code, we first used it to treat the constant-ν case. The results were found to agree exactly (as best as can be determined) with the analytic solution (8) at all Mach numbers.

Let us now focus on the results of the MC calculation performed for constant σ. We note first that, even though we found that $f(\mathbf{u})$ *does not separate exactly* as in Eqs. (6) and (7), it does separate to a good approximation and shares many of the properties of a separable distribution. A first indication of this is that, for all values of M, the u_z-averaged distribution of transverse velocities,

$$f_\perp(u_\perp) \equiv \int_{-\infty}^{\infty} du_z f(u_z, u_\perp), \tag{10}$$

is found to be exactly Maxwellian at temperature T, as in Eq. (7) (as accurately as can be determined from the MC simulation; this might well be a rigorous result—so far we have not be able to prove it analytically). Second, the $u_\perp$ variation of $f(u_z, u_\perp)$, for any fixed u_z, is found to be very close to Maxwellian. This is shown in Fig. 2, where the $u_\perp$ dependence of $f(u_z, u_\perp)$, is plotted on a semi-log scale against $u_\perp^2$, for several fixed values of u_z and for $M = 1$, 4, and 10. In this plot scheme, a Maxwellian distribution corresponds to an oblique straight line, and the slope of the line is indicative of the effective temperature $T_\perp$ of the Maxwellian. We also include for comparison a plot of $\exp\left(-\frac{1}{2}u_\perp^2\right)$, i.e., the $T_\perp = T$ line. Figure 2 shows that $T_\perp$ depends to some extent on the value of u_z, an indication that the separation of variables in not exact. But the deviation of $T_\perp$ from T is small. For both very large and very small values of M, the separation of variables in the form Eq. (6) becomes exact, i.e., $T_\perp \to T$, and for all Mach numbers $T_\perp$ is within a few percent of T in the bulk of the distribution; the deviation is largest at $M \simeq 2$, where it is about 14% in the wings of the distribution. Thus, the velocity distribution $f(\mathbf{u})$ is multiplicative to a reasonable approximation, i.e.,

$$f(u_z, u_\perp) \simeq f_z(u_z) f_\perp(u_\perp), \tag{11}$$

where

$$f_z(u_z) \equiv 2\pi \int_0^{\infty} du_\perp \, u_\perp f(u_z, u_\perp), \tag{12}$$

is the average of $f(u_z, u_\perp)$ over $u_\perp$ and $f_\perp(u_\perp) \simeq \frac{1}{2\pi}\exp\left(-\frac{1}{2}u_\perp^2\right)$.

To further illustrate the shape of $f(u_z, u_\perp)$, in Fig. 3, we show a 3D plot of the distribution function obtained from the MC code. The main features are easily visible: strong anisotropy, a Maxwellian distribution in $u_\perp$, and a broad, asymmetric distribution in u_z—with a peak in the thermal region near $u_z \simeq 2$ and a long Maxwellian tail extending to several times M.

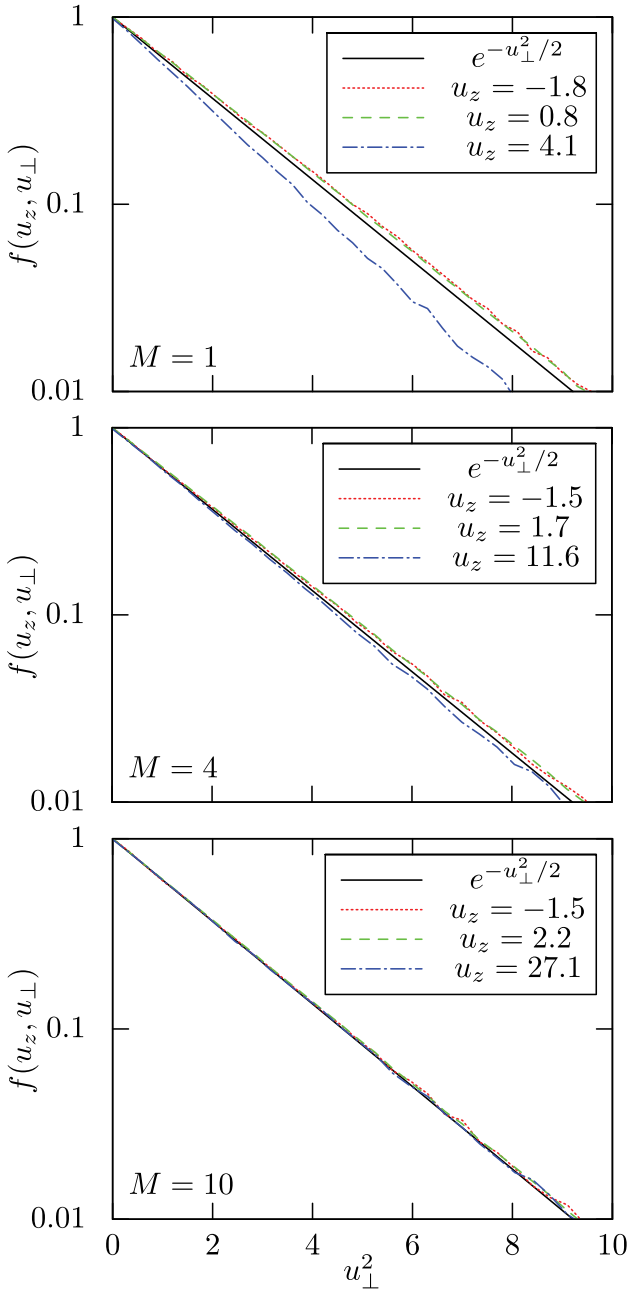

FIG. 2. Results of MC simulations for constant σ. Shown are semi-log plots of $f(u_z, u_\perp)$ as a function of $u_\perp^2$, plotted for fixed u_z. Different panels represent three different values of M. The solid line is the Maxwellian $\exp(-\frac{1}{2}u_\perp^2)$, the other three lines correspond to different values of u_z, as indicated in the inset. The u_z values are chosen to be at the peak of f, at the point on the left where f is 10% of peak, and at the point on the right where f is 10% of peak.

If one chooses to take advantage of the approximate separation of variables Eq. (11), the problem of calculating the distribution function is essentially reduced to 1D, the results are more easily visualized, the statistical requirements for the MC calculation are greatly reduced, and applications of the method, e.g., use of $f(\mathbf{v})$ to load simulation particles in a PIC simulation, are very much simplified. We shall also show in Sec. IV that the approximate separation of variables makes it possible to develop a very accurate simple analytical model.

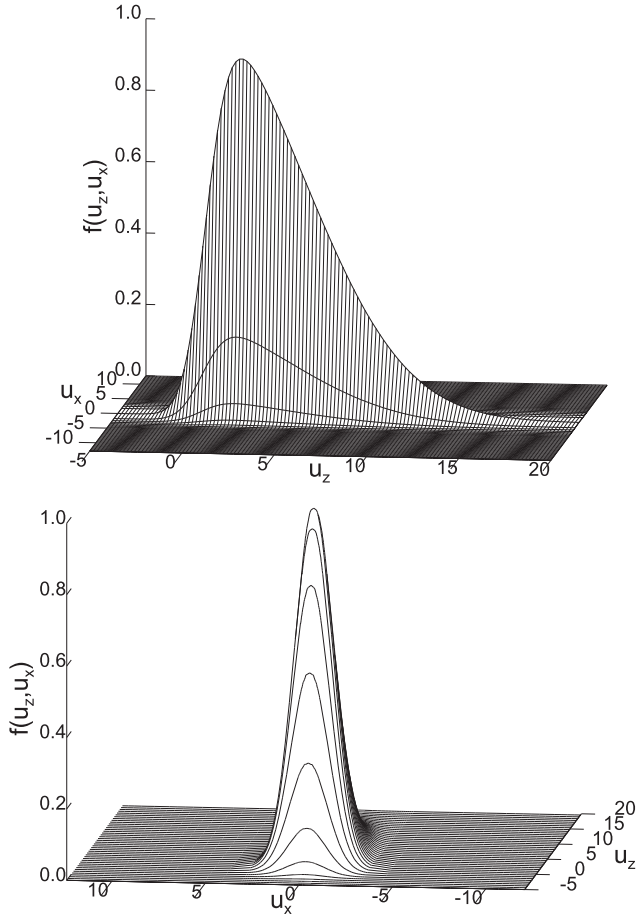

FIG. 3. MC results for constant σ, showing 3D plot of $f(u_z, u_\perp)$ for $M = 4$. Two different perspectives are depicted, with $u_x = \pm u_\perp$.

In Fig. 4, we show the MC results for $f_z(u_z)$ for four different Mach numbers. Also shown are the approximate analytic calculations from Eqs. (8) and (9). We note that Eq. (8) is a good approximation for M up to about 1, but has become inaccurate at $M = 2$. Equation (9) is reasonably accurate

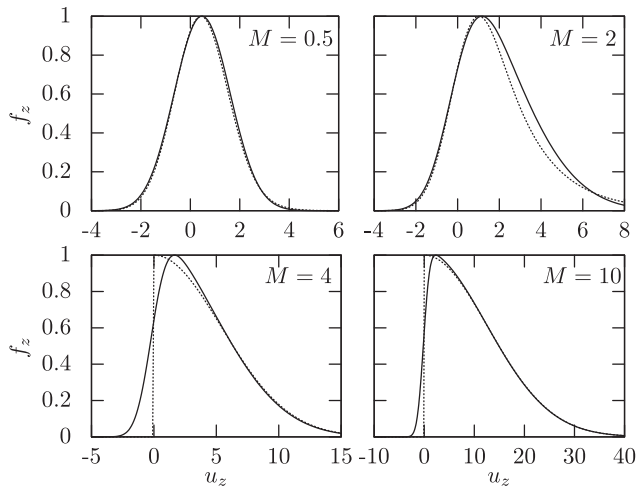

FIG. 4. Solid curves: MC distribution functions for $M = 0.5$, 2, 4, 10. Dotted curves: For $M = 0.5$ and $M = 2$, the constant-ν analytic distribution from Eq. (8). For $M = 4$ and $M = 10$, the constant-σ high-Mach-number analytic distribution from Eq. (9).

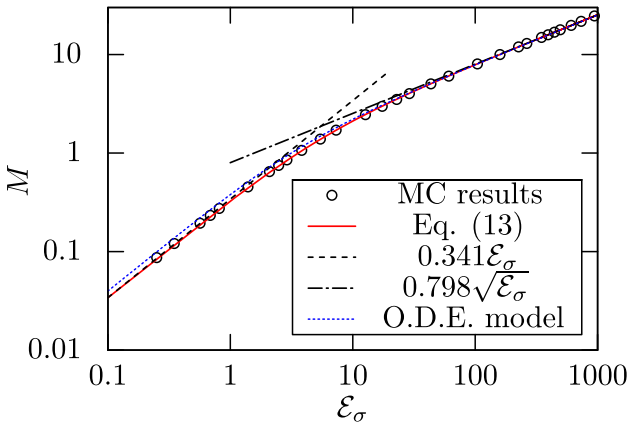

FIG. 5. Dependence of the ion Mach number M on the normalized field $\mathcal{E}_\sigma$.

overall at $M = 10$, and accurately represents the high-velocity tail of the distribution even for M as small as 4. However, Eq. (9) becomes less accurate near the peak of the distribution as M decreases, and most importantly, Eq. (9) entirely misses the thermal spread of $f_z(u_z)$ near $u_z = 0$.

In Fig. 5, we show the dependence of the drift velocity on the electric field expressed in the dimensionless form $M(\mathcal{E}_\sigma)$ (i.e., the normalized mobility). The MC results are in agreement with the known limits, $M \simeq 0.341\mathcal{E}_\sigma$ for $\mathcal{E}_\sigma \to 0$, and $M = \sqrt{(2/\pi)\mathcal{E}_\sigma} \simeq 0.798\sqrt{\mathcal{E}_\sigma}$ for $\mathcal{E}_\sigma \to \infty$.[20] For arbitrary $\mathcal{E}_\sigma$, the interpolation formula,

$$M = \frac{0.682\mathcal{E}_\sigma}{1 + \sqrt{1 + \dfrac{0.277\mathcal{E}_\sigma^{3/2}}{1 + 0.379\mathcal{E}_\sigma^{1/2}}}}, \tag{13}$$

fits the MC results to accuracy better than 3%.

In Fig. 6, we compare MC results for $f_z(u_z)$ under the constant-σ approximation with MC results using the exact cross section Eq. (2) for Ar. Although differences are visible for large-M cases, the constant-σ model is seen to be reasonably accurate, and to reproduce all the qualitative features of $f_z(u_z)$. This is not a surprise, as σ has only a weak logarithmic dependence on the relative velocity of the two colliding particles. The constant-σ approximation is probably good enough for most practical purposes. But if greater accuracy is desired, the MC code is available to readers with the online documentation for this paper.[23] The code can easily be used to calculate distribution functions for any species with any prescribed cross section.

IV. CONSTANT-σ APPROXIMATION: SIMPLE MODEL FOR ALL MACH NUMBERS

Assuming constant cross section σ, guided by the MC results of Sec. III, and following the strategy of averaging over Maxwellian-distributed variables, we can formulate an accurate approximate model for $f_z(u_z)$ that is valid for any value of $\mathcal{E}_\sigma$ and throughout the full range of u_z. We begin with the Boltzmann equation (3), rewritten in terms of the dimensionless velocities $\mathbf{u}$ and $\mathbf{u}'$, and the dimensionless electric field $\mathcal{E}_\sigma$,

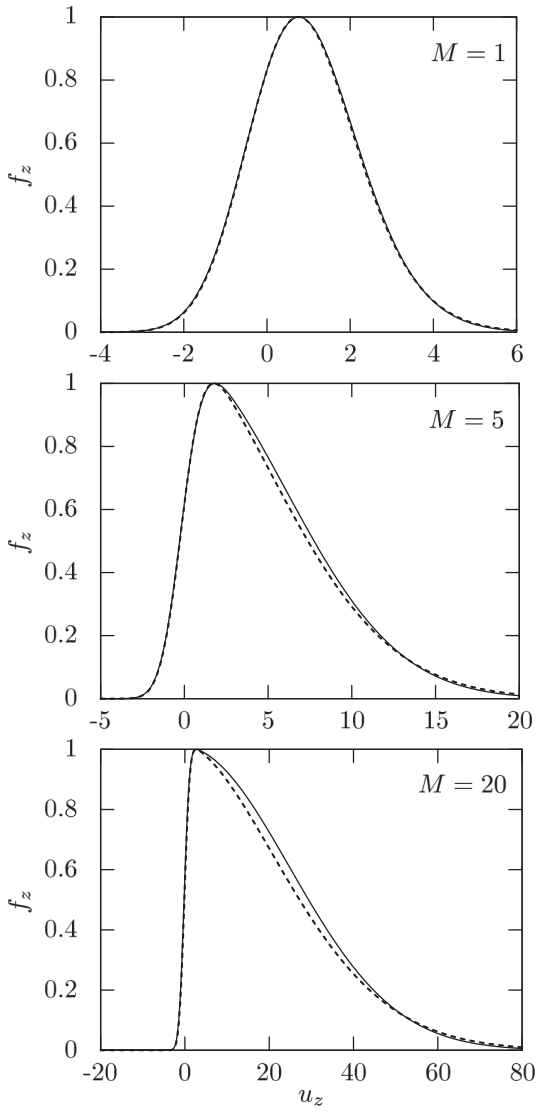

FIG. 6. Comparison of MC results for constant σ (dashed line) and for the exact σ, Eq. (2) (solid line), obtained for three different values of M.

$$\mathcal{E}_\sigma \frac{\partial f}{\partial u_z} = \exp\left(-\frac{u^2}{2}\right)\int \frac{d\mathbf{u}'}{(2\pi)^{3/2}}|\mathbf{u}-\mathbf{u}'|f(\mathbf{u}') - f(\mathbf{u})\int \frac{d\mathbf{u}'}{(2\pi)^{3/2}}|\mathbf{u}-\mathbf{u}'|\exp\left(\frac{-u'^2}{2}\right). \tag{14}$$

Making the multiplicative approximation Eq. (11) for $f(\mathbf{u})$ and integrating Eq. (14) over $\mathbf{u}_\perp$, we obtain

$$\mathcal{E}_\sigma \frac{df_z}{du_z} + U(u_z)f_z(u_z) = \frac{W(u_z)}{(2\pi)^{1/2}}\exp\left(-\frac{u_z^2}{2}\right), \tag{15}$$

where

$$U(u_z) = \int \frac{d\mathbf{u}_\perp d\mathbf{u}'}{(2\pi)^{5/2}}|\mathbf{u}-\mathbf{u}'|\exp\left(-\frac{u_\perp^2 + u'^2}{2}\right) \tag{16}$$

and

$$W(u_z) = \int \frac{d\mathbf{u}_\perp d\mathbf{u}'}{(2\pi)^2}|\mathbf{u}-\mathbf{u}'|f_z(u_z')\exp\left(-\frac{u_\perp^2 + u_\perp'^2}{2}\right). \tag{17}$$

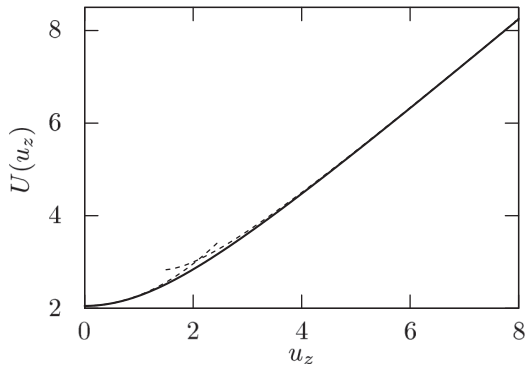

FIG. 7. The mean relative velocity $U(u_z)$ from Eq. (18). Dashed lines show the asymptotes, Eq. (19).

We show in Appendix A that $U(u_z)$ can be calculated in closed form,

$$U(u_z) = \sqrt{\frac{2}{\pi}}\exp\left(-\frac{u_z^2}{2}\right) + u_z \mathrm{erf}\left(\frac{u_z}{\sqrt{2}}\right) + \sqrt{\frac{\pi}{2}}\exp\left(\frac{u_z^2}{2}\right)\left[1 - \mathrm{erf}^2\left(\frac{u_z}{\sqrt{2}}\right)\right], \tag{18}$$

which is plotted in Fig. 7. In the limits of small and large u_z, it becomes

$$U(u_z) = \begin{cases} a_+ + a_- \dfrac{u_z^2}{2}, & u_z \to 0, \\ |u_z| + \dfrac{2}{|u_z|}, & |u_z| \to \infty, \end{cases} \tag{19}$$

where $a_\pm = \sqrt{\frac{\pi}{2}} \pm \sqrt{\frac{2}{\pi}}$.

Equation (15) is still an integro-differential equation, since $W(u_z)$ is an integral over $f_z(u_z)$. However, we note that the dependence of the r.h.s. of Eq. (15) on u_z is dominated by the exponential factor $\exp(-\frac{1}{2}u_z^2)$, whereas the function $W(u_z)$ varies relatively slowly: When $\mathcal{E}_\sigma$ is small and $f_z(u_z) \to \frac{1}{\sqrt{2\pi}} e^{-u_z^2/2}$, $W(u_z)$ tends to Eq. (18) (see Fig. 7); for large $\mathcal{E}_\sigma$ one can substitute $f_z(u_z)$ from Eq. (9), which yields $W(u_z) \propto u_z$. Thus, it is a reasonable approximation to replace $W(u_z)$ by its Maxwellian average,

$$\langle W \rangle = \int_{-\infty}^{\infty} \frac{du_z}{(2\pi)^{1/2}} W(u_z) \exp\left(-\frac{u_z^2}{2}\right). \tag{20}$$

The integral equation (15) is then reduced to an ordinary differential equation,

$$\mathcal{E}_\sigma \frac{df_z}{du_z} + U(u_z) f_z(u_z) = \frac{\langle W \rangle}{(2\pi)^{1/2}} \exp\left(-\frac{u_z^2}{2}\right), \tag{21}$$

where for a given value of $\mathcal{E}_\sigma$, $\langle W \rangle$ is just a number rather than a function of u_z. The key point is that *we do not need to know the value of* $\langle W \rangle$, since the linearity of Eq. (21) implies that $\langle W \rangle$ determines only the amplitude, not the shape of $f_z(u_z)$. The correct condition to specify the amplitude is conservation of particles, which requires $\int_{-\infty}^{\infty} du_z f_z(u_z) = 1$. Thus, the proper solution of Eq. (21) is

$$f_z(u_z) = \frac{\tilde{f}_z(u_z)}{\int_{-\infty}^{\infty} du_z \tilde{f}_z(u_z)}, \tag{22}$$

where $\tilde{f}_z(u_z)$ is the solution of the linear ordinary differential equation (O.D.E.),

$$\frac{d\tilde{f}_z}{du_z} + \frac{U(u_z)}{\mathcal{E}_\sigma} \tilde{f}_z(u_z) = \exp\left(-\frac{u_z^2}{2}\right), \tag{23}$$

with the boundary condition $\tilde{f}_z(-\infty) = 0$. The analytical solution of Eq. (23),

$$\tilde{f}_z(u_z) = \int_{-\infty}^{u_z} du'' \exp\left(-\frac{u''^2}{2} - \int_{u''}^{u_z} du' \frac{U(u')}{\mathcal{E}_\sigma}\right),$$

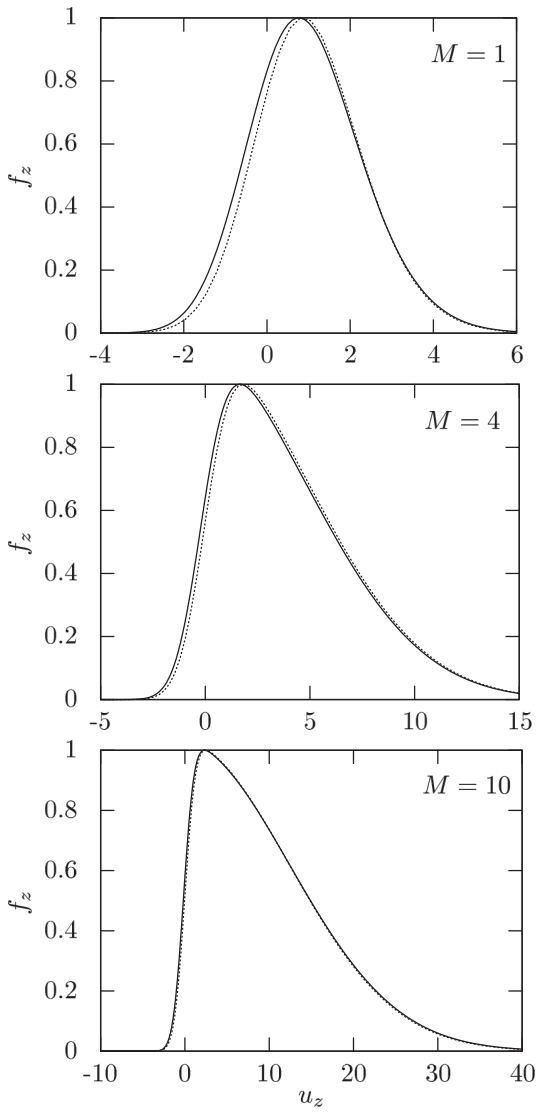

FIG. 8. Comparison of $f_z(u_z)$ from the MC simulations (solid curves) with the results of the O.D.E. model, Eq. (23) (dotted curves), obtained for three different values of M.

is complicated and not all of the integrals can be reduced to elementary functions, so there is little point in writing it out explicitly. On the other hand, it is trivial and virtually instantaneous to solve Eq. (23) numerically.

Figure 8 compares the distribution functions calculated from the approximate O.D.E model Eqs. (22) and (23) to the MC distributions, at $M=1$, 4, and 10. Also, in Fig. 5 the O.D.E results for the normalized mobility $M(\mathcal{E}_\sigma)$ are compared with the MC results. One can see that the O.D.E. model agrees very well with the exact MC solutions, and that the agreement is least good at low Mach numbers.

To understand the origins of the small discrepancy at low M, we note that in the limit $\mathcal{E}_\sigma \to \infty$ the solutions of the approximate Eq. (21) and exact Eq. (14) coincide; they tend to Eq. (9), which yields $M \simeq 0.798\sqrt{\mathcal{E}_\sigma}$. However, the two approximations employed to derive Eq. (21), viz., (i) the multiplicative approximation Eq. (11) and (ii) replacement of $W(u_z)$ with $\langle W\rangle$ in Eq. (15), become less accurate at small $\mathcal{E}_\sigma$. We show in Appendix B that the O.D.E model gives $M \simeq 0.398\mathcal{E}_\sigma$ in the limit $\mathcal{E}_\sigma \to 0$ (whereas the exact result is $M \simeq 0.341\mathcal{E}_\sigma$), which corresponds to a deviation of almost 17% in this worst case. One can also estimate how the approximations contribute to the error: The approximation (ii) yields $\langle W\rangle = \langle U^{-1}\rangle^{-1}$ in the limit $\mathcal{E}_\sigma \to 0$ [see Eq. (B2)], whereas the correct result in this limit, obtained by taking the average of Eqs. (16) and (17), is $\langle W\rangle = \langle U\rangle$. However, the resulting error is only about 1%. The major contribution to the discrepancy is thus due to the multiplicative approximation (i).

V. DISCUSSION AND CONCLUSION

We have presented a MC numerical simulation that can be used to calculate the ion mobility and the ion distribution function $f(\mathbf{v})$, for a homogeneous partially ionized plasma subject to a uniform electric field, using the exact energy dependence of the charge-exchange cross section σ. As an illustration and baseline case, we calculated $f(\mathbf{v})$ for Ar.

We noted first that for strong electric fields (i.e., thermal Mach number M greater than unity) the displaced Maxwellian distribution, which is frequently assumed because of its simplicity, grossly misrepresents $f(\mathbf{v})$. The correct distribution is asymmetric and much broader than the displaced Maxwellian, extending from $v_z \simeq -(1-2)v_T$ on the left, to a peak at $v_z \simeq (1-3)v_T$, and ending in a long tail that extends to $v_z \simeq (3-4)Mv_T$.

We then compared the exact MC result to the $f(\mathbf{v})$ that one obtains under the assumption of constant σ. We found good agreement, so that the assumption of constant σ is probably sufficient for most purposes. This is not a surprise, as the energy dependence of σ is quite weak. We also compared the exact MC result to the $f(\mathbf{v})$ that one obtains under the assumption of constant collision frequency ν, which admits an exact analytic solution. For Mach numbers greater than unity, we found the assumption of constant ν to be qualitatively inaccurate, showing an exponential dependence at large positive v_z, whereas the exact solution (and the constant-σ solution) show a Gaussian dependence.

We then explored the properties of the constant-σ MC solution in more detail. Although $f(\mathbf{v})$ does not separate exactly into a product $f_z(v_z)f_\perp(v_\perp)$, we found that this multiplicative form holds to good accuracy and, moreover, that $f_\perp(v_\perp)$ is simply a Maxwellian at the neutral temperature T (to the accuracy provided by MC simulations). We used this property to reduce the Boltzmann equation to an integro-differential equation for $f_z(v_z)$. Furthermore, we employed the fact that the integral part of the obtained equation is a slowly varying function of v_z. This allowed us to replace the integral by its Maxwellian average and, hence, to derive an ordinary differential equation which can easily be solved either numerically or analytically. We believe that this O.D.E. model gives an adequate representation of the ion mobility and ion distribution function for most practical purposes. However, if greater accuracy is desired, the MC code is available to the reader, and can be used to generate an exact solution based on the best available cross section data for any species.

ACKNOWLEDGMENTS

The research leading to these results has received funding from the European Research Council under the European Union's Seventh Framework Programme (FP7/2007-2013)/ ERC Grant agreement 267499. Martin Lampe wishes to thank Richard Fernsler for helpful discussions.

APPENDIX A: CALCULATION OF $U(u_z)$

In Eq. (16), we defined the Gaussian average of $|\mathbf{u}-\mathbf{u}'|$ over $\mathbf{u}_\perp$ and $\mathbf{u}'$, which we called $U(u_z)$. This quantity can be evaluated in closed form. We begin with the average over $\mathbf{u}'$ performed in spherical coordinates,

$$\langle|\mathbf{u}-\mathbf{u}'|\rangle_{\mathbf{u}'} = \int \frac{d\mathbf{u}'}{(2\pi)^{3/2}}|\mathbf{u}-\mathbf{u}'|\exp\left(-\frac{u'^2}{2}\right)$$
$$= \int_0^\infty \frac{dw}{(2\pi)^{1/2}}w^3\int_{-1}^{1}d\mu \times \exp\left[-\frac{1}{2}(w^2+u^2+2wu\mu)\right],$$

where $\mathbf{w}\equiv\mathbf{u}'-\mathbf{u}$, $\mu\equiv\cos\theta$, and θ is the angle between $\mathbf{w}$ and $\mathbf{u}$. The integral over μ can be done trivially, and then using $w-u$ and $w+u$ as variables of integration in place of w, we find

$$\langle|\mathbf{u}-\mathbf{u}'|\rangle_{\mathbf{u}'} = \sqrt{\frac{2}{\pi}}\exp\left(-\frac{u^2}{2}\right)+\left(u+\frac{1}{u}\right)\mathrm{erf}\left(\frac{u}{\sqrt{2}}\right). \quad \text{(A1)}$$

To calculate $U(u_z)$, we average Eq. (A1) over $\mathbf{u}_\perp$ in cylindrical coordinates. We use u rather than $u_\perp$ as the variable of integration. At the next step, the integral can be done by substituting $\mathrm{erf}(u/\sqrt{2}) = \frac{2}{\sqrt{\pi}}\int_0^{u/\sqrt{2}} dt\, e^{-t^2}$ and reversing the order of integration. This yields

$$U(u_z) = \int \frac{d\mathbf{u}_\perp}{2\pi} \langle |\mathbf{u} - \mathbf{u}'| \rangle_{\mathbf{u}'} \exp\left(-\frac{u_\perp^2}{2}\right)$$
$$= \frac{1}{\sqrt{2\pi}} \exp\left(-\frac{u_z^2}{2}\right) + \exp\left(\frac{u_z^2}{2}\right) \int_{|u_z|}^{\infty} du(1+u^2) \exp\left(-\frac{u^2}{2}\right) \mathrm{erf}\left(\frac{u}{\sqrt{2}}\right)$$
$$= \sqrt{\frac{2}{\pi}} \exp\left(-\frac{u_z^2}{2}\right) + u_z \,\mathrm{erf}\left(\frac{u_z}{\sqrt{2}}\right) + \sqrt{\frac{\pi}{2}} \exp\left(\frac{u_z^2}{2}\right) \left[1 - \mathrm{erf}^2\left(\frac{u_z}{\sqrt{2}}\right)\right]. \quad \text{(A2)}$$

APPENDIX B: CALCULATION OF $M(\mathcal{E}_\sigma)$ FOR THE O.D.E. MODEL: LIMIT OF SMALL $\mathcal{E}_\sigma$

We rewrite Eq. (21) in the following form:

$$f_z(u_z) = \frac{1}{(2\pi)^{1/2}} \frac{\langle W \rangle}{U(u_z)} \exp\left(-\frac{u_z^2}{2}\right) - \frac{\mathcal{E}_\sigma}{U(u_z)} \frac{df_z}{du_z}. \quad \text{(B1)}$$

By integrating this over u_z and using the normalization condition $\int_{-\infty}^{\infty} du_z f_z(u_z) = 1$, we readily obtain in the limit $\mathcal{E}_\sigma \to 0$,

$$\langle W \rangle = \frac{1}{\langle U^{-1} \rangle}, \quad \text{(B2)}$$

where the average operator $\langle \ldots \rangle$ is defined in Eq. (20). Now, we can calculate the Mach number,

$$M \equiv \int_{-\infty}^{\infty} du_z u_z f_z(u_z) = -\mathcal{E}_\sigma \int_{-\infty}^{\infty} du_z \frac{u_z}{U(u_z)} \frac{df_z}{du_z}.$$

By substituting $f_z(u_z) \simeq \frac{1}{(2\pi)^{1/2}} \frac{\langle W \rangle}{U(u_z)} e^{-u_z^2/2}$ and using Eq. (B2), after simple algebra we derive

$$M = \frac{1}{2\langle U^{-1} \rangle} \left\langle \frac{1+u_z^2}{U^2} \right\rangle \mathcal{E}_\sigma. \quad \text{(B3)}$$

Numerical integration using Eq. (18) yields $M \simeq 0.398\mathcal{E}_\sigma$.

[1] B. M. Smirnov, *Physics of Ionized Gases* (Wiley-VCH, 2001).
[2] G. E. Morfill and A. V. Ivlev, Rev. Mod. Phys. **81**, 1353 (2009).
[3] V. E. Fortov, A. V. Ivlev, S. A. Khrapak, A. G. Khrapak, and G. E. Morfill, Phys. Rep. **421**, 1 (2005).
[4] B. M. Smirnov, *Plasma Processes and Plasma Kinetics* (Wiley-VCH, 2007).
[5] A. V. Phelps, J. Appl. Phys. **76**, 747 (1994).
[6] G. Joyce, M. Lampe, R. F. Fernsler, and W. M. Manheimer, Plasma Sources Sci. Technol. **9**, 429 (2000).
[7] F. Melandso and J. Goree, Phys. Rev. E **52**, 5312 (1995).
[8] S. V. Vladimirov and O. Ishihara, Phys. Plasmas **3**, 444 (1996).
[9] O. Ishihara and S. V. Vladimirov, Phys. Plasmas **4**, 69 (1997).
[10] M. Lampe, G. Joyce, and G. Ganguli, Phys. Plasmas **7**, 3851 (2000).
[11] G. Lapenta, Phys. Rev. E **62**, 1175 (2000).
[12] D. Winske, W. Daughton, D. S. Lemons, and M. S. Murillo, Phys. Plasmas **7**, 2320 (2000).
[13] D. Else, R. Kompaneets, and S. V. Vladimirov, Phys. Plasmas **16**, 062106 (2009).
[14] T. B. Röcker, S. K. Zhdanov, A. V. Ivlev, M. Lampe, G. Joyce, and G. E. Morfill, Phys. Plasmas **19**, 073708 (2012).
[15] R. Kompaneets, U. Konopka, A. V. Ivlev, V. Tsytovich, and G. Morfill, Phys. Plasmas **14**, 052108 (2007).
[16] M. V. Rao, R. J. Van Brunt, and J. K. Olthoff, Phys. Rev. E **54**, 5641 (1996).
[17] S. A. Khrapak, A. V. Ivlev, S. K. Zhdanov, and G. E. Morfill, Phys. Plasmas **12**, 042308 (2005).
[18] A. V. Ivlev, S. K. Zhdanov, S. A. Khrapak, and G. E. Morfill, Phys. Rev. E **71**, 016405 (2005).
[19] P. L. Bhatnagar, E. P. Gross, and M. Krook, Phys. Rev. **94**, 511 (1954).
[20] B. M. Smirnov, Sov. Phys. Tech. Phys. **11**, 1388 (1967).
[21] S. A. Maiorov, O. F. Petrov, and V. E. Fortov, in *34th EPS Conference on Plasma Physics, Warsaw, 2–6 July 2007* (2007), ECA Vol. 31F, P2.115.
[22] C. K. Birdsall, IEEE Trans. Plasma Sci. **19**, 65 (1991).
[23] See supplementary material at http://dx.doi.org/10.1063/1.4768456 for the FORTRAN code of the Monte Carlo simulation.

Effective dipole moment for the mode coupling instability: Mapping of self-consistent wake models

T. B. Röcker,[1] S. K. Zhdanov,[1,a)] A. V. Ivlev,[1] M. Lampe,[2] G. Joyce,[3,b)] and G. E. Morfill[1]
[1]*Max Planck Institute for Extraterrestrial Physics, 85741 Garching, Germany*
[2]*Department of Astronomy, University of Maryland, College Park, Maryland 20740, USA*
[3]*Icarus Research, Inc., Bethesda, Maryland 20814, USA*

(Received 23 April 2012; accepted 4 June 2012; published online 25 July 2012)

The theory of the mode coupling instability operating in two-dimensional plasma crystals is generalized, by employing the linear plasma response formalism to describe the interparticle interactions self-consistently. In this approach, the underlying ion distribution function is calculated from first principles. Subthermal and suprathermal regimes of the ion flow are considered. A mapping procedure is proposed, which relates the self-consistent coupling coefficients to the effective dipole moment of the wake—the parameter which characterizes the mode coupling in the framework of the conventionally used Yukawa/point-wake model. The importance of the self-consistent approach is demonstrated by comparing the theoretically obtained dipole moments with the values deduced from experiments. © *2012 American Institute of Physics*. [http://dx.doi.org/10.1063/1.4737143]

I. INTRODUCTION

Understanding the melting mechanisms operating in plasma crystals is a fundamental problem in the physics of complex (dusty) plasmas.[1,2] One can distinguish generic melting[3–10] (also occurring in other strongly coupled systems, i.e., molecular liquids, colloidal dispersions) from plasma-specific melting processes. For 2D crystals, the *mode coupling instability* (MCI)[11] is the primary plasma-specific melting mechanism.[11–17] Melting in this case is accompanied by anomalous increase of the particle kinetic energy.

The MCI occurs because the interparticle interactions are *mediated* by the plasma wakes. The wakes[18–24] are generated due to ion flow in the plasma (pre)sheath, where particles normally levitate in ground-based experiments.[1,25,26] The electrostatic field of the wakes makes the interaction anisotropic and *nonreciprocal*,[27] so that strongly coupled particle systems—plasma crystals—can absorb energy from the ambient plasma. This can trigger crystal disruption, provided the damping is weak.[17,28–30]

The most remarkable fact about the MCI (Ref. 17) is that in all experiments with 2D plasma crystals where the instability onset has been observed so far, it can be quite precisely described with a simple string model[11] and its 2D generalization.[13] One of the prominent features—"fingerprints"—of the instability is the emergence of *hot spots* in the phonon fluctuation spectra (measured experimentally[14] or obtained in numerical simulations[17]), which originate from the wake-induced coupling of two dust-lattice (DL) wave modes.[11,13]

In the so-called "Yukawa/point-wake" interaction model usually employed in the MCI theory, the wake is represented as a positive, point-like effective charge below each particle. The resulting interaction between particles is a superposition of the particle-particle and particle-wake interactions, both described by the (spherically symmetric) Yukawa potentials. Although the MCI theory itself is essentially self-contained, the Yukawa/point-wake model includes two free parameters: The first one, the effective wake charge, is in fact a hidden parameter—it can be readily excluded from consideration by renormalizing the particle charge (this is equivalent to taking into account the particle self-action effect—the ion drag force), as explained recently in Ref. 17. The second parameter, the effective dipole moment of the wake, characterizes the breaking of vertical symmetry and thereby determines the MCI growth rate. The dipole moment is an input to the theory, which previously has been specified by fitting to experimental data on the MCI.[17]

The aim of this paper is to evaluate the effective dipole moment of the wake—the critical parameter in the MCI. By utilizing the linear plasma response kinetic theory, this can be done from first principles. We employ two different analytic models: the constant collision frequency (CCF) model[31] appropriate to the subthermal regime of the ion flow and the constant mean-free path (CMP) model[32] originally derived for a highly suprathermal regime. The analytic results are complemented with results from Monte Carlo (MC) simulations which are applicable to arbitrary flow velocities. We demonstrate the applicability of the theoretical work by estimating the effective dipole moments for several experiments spanning a broad range of the ion flow velocities.

II. MAJOR CHARACTERISTICS OF MCI

Let us consider a hexagonal monolayer of charged particles in a weakly ionized plasma—a 2D *plasma crystal*. The monolayer is parallel to the xy-plane (at $z^{(0)} = 0$), as shown in Fig. 1(a). The particle equilibrium positions in this reference frame are $\mathbf{r}_j^{(0)} = (s_x\hat{\mathbf{e}}_x + s_y\hat{\mathbf{e}}_y)\Delta$, where Δ is the lattice constant and $s_x = \frac{\sqrt{3}}{2}m$ and $s_y = \frac{1}{2}m + n$ are components of the vector $\mathbf{s}$ with the absolute value $s = \sqrt{m^2 + n^2 + mn}$ (m, n are integer).

a)e-mail: zh@mpe.mpg.de.
b)Deceased.

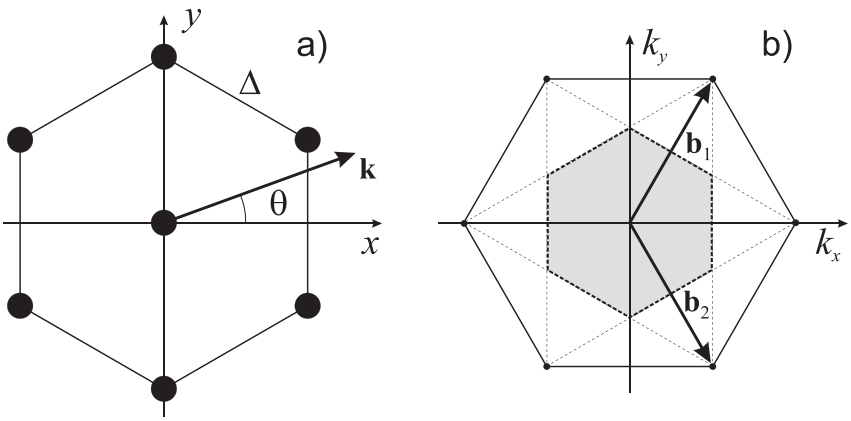

FIG. 1. (a) Elementary hexagonal lattice cell with the frame of reference. (b) The reciprocal lattice in $\mathbf{k}$-space with the basis vectors $|\mathbf{b}_1| = |\mathbf{b}_2| = \frac{4\pi}{\sqrt{3}}\Delta^{-1}$. Due to the lattice symmetry, it is sufficient to consider the wave vectors $\mathbf{k}$ at $0^\circ \le \theta \le 30^\circ$ and from within the first Brillouin zone (gray region enclosed by dashed lines), so that $|\mathbf{k}|\Delta \le \frac{2\pi}{\sqrt{3}}$ for $\theta = 0^\circ$ and $|\mathbf{k}|\Delta \le \frac{4\pi}{3}$ for $\theta = 30^\circ$.

Each particle acquires a large negative charge in a plasma, e.g., for grains in the range of 5–10 μm, it is typically some tens of thousands of electron charges.[2] The monolayer is levitating horizontally, at the height where gravity is primarily balanced by an inhomogeneous (vertical) electric field of the sheath. "Microscopically," every charged particle embedded in a flowing plasma acts as a lens, effectively focusing the ion flow and hence inducing local plasma polarization. Therefore, additional important contributions to the force balance are the *direct* ion drag force $F_{\rm id}$, which is (mostly) due to the interaction of a particle with its own wake, and the *induced* vertical components $F_{\rm id}^{(\rm ind)}$ of the force exerted by wakes of the neighboring particles. Thus, the equilibrium levitation condition reads as follows:

$$mg + F_{\rm id}(M_T) + \sum F_{\rm id}^{(\rm ind)}(M_T) = QE_0, \tag{1}$$

where Q and m are the particle charge and mass, respectively, g is the gravitational acceleration, E_0 is the electrical field of the sheath at equilibrium, and the summation is over all particles in the lattice. Note that $F_{\rm id}(M_T)$ and $F_{\rm id}^{(\rm ind)}(M_T)$ are usually nonlinear functions of the thermal Mach number (defined as ratio of ion flow velocity u_i to thermal velocity of neutrals $v_T = \sqrt{T_n/m}$, i.e., $M_T = u_i/v_T$) which, in turn, is some (complicated) function of the electric field.

The dispersion relations of the DL modes are generally derived by considering small perturbations of the individual particle positions in the form $\propto e^{-i\omega t + i\mathbf{k}\cdot\mathbf{r}}$. After linearizing (and also including a frictional damping rate $\nu_{\rm dn}$ due to dust-neutral collisions), the dispersion relation $\omega(\mathbf{k})$ for each mode is determined by the requirement that $\omega(\omega + i\nu_{\rm dn})$ is an eigenvalue of the symmetric dynamical matrix $\mathsf{D}_\mathbf{k}$. The latter depends on the interparticle interactions and has the following generic form for the 2D modes:[13,17,33]

$$\mathsf{D}_\mathbf{k} = \begin{pmatrix} \alpha_x - \beta & 2\gamma & i\sigma_x \\ 2\gamma & \alpha_y + \beta & i\sigma_y \\ i\sigma_x & i\sigma_y & \Omega_{\rm conf}^2 - 2\alpha_z \end{pmatrix}. \tag{2}$$

Elements of $\mathsf{D}_\mathbf{k}$ strongly depend on the magnitude and the orientation of $\mathbf{k}$. It is assumed that vertically the particles are confined in a (parabolic) potential well characterized by the eigenfrequency $\Omega_{\rm conf} = 2\pi f_{\rm conf}$. The horizontal confinement is not discussed here, since we assume an infinite monolayer.

If the interactions are reciprocal (i.e., $\sigma_{x,y} \equiv 0$), then $\mathsf{D}_\mathbf{k}$ is Hermitian and therefore the eigenvalues $\omega(\omega + i\nu_{\rm dn})$ are real. When the interactions are nonreciprocal, the modes are coupled and the eigenvalues can become complex. This can trigger the MCI provided additional thresholds are fulfilled: both the damping rate and confinement eigenfrequency have to be sufficiently low.[11,13,17]

For further calculations, we normalize all frequencies by the DL frequency scale $\Omega_{\rm DL} = \sqrt{Q^2/(M\lambda^3)}$ (where λ is the model-specific screening length) and all wave vectors by interparticle distance Δ,

$$\omega/\Omega_{\rm DL} \to \omega, \quad \mathbf{k}\Delta \to \mathbf{k}.$$

For the Yukawa/point-wake model, this results in a "natural" normalization for the effective wake dipole moment,

$$\tilde{q}\tilde{\delta} \equiv \frac{q}{Q}\frac{\delta}{\Delta},$$

where q and δ are the effective "charge" and "downstream displacement" of the wake, respectively.[11]

Let us now focus on self-consistent interaction models. In the framework of the linear response formalism, the pair interaction force $\mathbf{F}(\mathbf{r})$ (exerted by a particle located at the origin) is given by the self-consistent electrostatic potential $\phi(\mathbf{r})$ which is expressed via the relevant plasma dielectric function $\epsilon(\mathbf{p})$,[31,34]

$$\mathbf{F}(\mathbf{r}) = -Q\nabla\phi, \quad \phi(\mathbf{r}) = \frac{Q}{2\pi^2}\int d\mathbf{p}\frac{e^{i\mathbf{p}\cdot\mathbf{r}}}{p^2\epsilon(\mathbf{p})}. \tag{3}$$

The ion drag force $F_{\rm id}$ in Eq. (1) is given by Eq. (3) at the origin. We stress that all assumptions involved in the particular plasma model are incorporated in $\epsilon(\mathbf{p})$.

The elements of the dynamical matrix in Eq. (2) can be computed from Eq. (3) by using the following mnemonic rules:

$$\{V\} = \frac{1}{2\pi^2\kappa^3}\sum_{m,n}\int d\mathbf{p}e^{i\mathbf{p}\cdot\mathbf{s}}(e^{-i\mathbf{k}\cdot\mathbf{s}} - 1)\frac{\{v\}}{p^2}\Re\left[\frac{1}{\epsilon(\mathbf{p})}\right], \tag{4}$$

where $\kappa = \Delta/\lambda$ is the screening parameter (we also use the normalization $\mathbf{p}\Delta \to \mathbf{p}$). The reciprocal (dispersion) elements are determined as

$$\{V\} \equiv \{\alpha_x - \beta, \alpha_y + \beta, \gamma, \alpha_z\},$$

$$\{v\} \equiv \left\{p_x^2, p_y^2, \frac{1}{2}p_x p_y, p_z^2\right\},$$

and the nonreciprocal (coupling) elements responsible for the mode coupling are

$$\sigma_{\{x,y\}} = \frac{1}{2\pi^2\kappa^3}\sum_{m,n}\int d\mathbf{p}e^{i\mathbf{p}\cdot\mathbf{s}}(e^{-i\mathbf{k}\cdot\mathbf{s}} - 1)\frac{p_{\{x,y\}}p_z}{p^2}\Im\left[\frac{1}{\epsilon(\mathbf{p})}\right]. \tag{5}$$

Note that the summations run over all integers except $(0,0)$. The integrals specifying the elements are all well defined and rapidly converging and can be successfully treated by applying suitable numerical methods. Moreover, in some cases, calculations can be performed analytically. Below we consider two practically important regimes.

III. WAKES AT DIFFERENT MACH NUMBERS: CCF AND CMP MODELS

The dominant ion collision process in weakly ionized plasma is ion-neutral charge exchange. The collision frequency is $\nu = n_n\langle\sigma_{in}v_{\rm rel}\rangle$, where $\langle\ldots\rangle$ denotes average over relevant velocity distributions (of ions and neutrals), n_n is the neutral number density, $v_{\rm rel}$ is the relative velocity between the ion and the neutral scatter, and the cross section σ_{in} is assumed to be independent of $v_{\rm rel}$ (in fact, σ_{in} has a weak logarithmic dependence on $v_{\rm rel}$, which usually can be neglected[35]). For $M_T \ll 1$, the mean relative velocity $\langle v_{\rm rel}\rangle$ is equal to the thermal velocity of neutrals v_T times a factor of order unity. Then, it is reasonable to approximate that ν is independent of the ion flow velocity u_i and is equal to $\nu = \langle v_{\rm rel}\rangle/\ell$, where $\ell = (\sigma_{in}n_n)^{-1}$ is the ion mean free path. In this CCF limit, the collision integral reduces to the Bhatnagar-Gross-Krook (BGK) form.[36] The flow velocity, $u_i = eE_0/m_i\nu$, is thus proportional to E_0, and it is possible to derive rather simple analytic expressions for the ion distribution function and the interaction potential.[31] However, when $M_T \gg 1$, the BGK model becomes increasingly inaccurate, since $\langle v_{\rm rel}\rangle \sim u_i$ and, thus, $u_i \propto \sqrt{E_0}$, which is in agreement with experimental data.[37–42] At large M_T, the appropriate approximation is CMP rather than CCF. Kompaneets *et al.*[32] derived the interaction potential in the CMP approximation analytically *in the limit* $M_T \to \infty$, i.e., neglecting the ion thermal motion. The longitudinal ion velocity distribution in this limit has a simple half-Maxwellian form with the temperature proportional to E_0 (see Eq. (3) in Ref. 32).

In order to evaluate the range of validity of these two analytical models, we use MC simulations where a constant ion-neutral charge exchange cross section (and, hence, a constant mean free path) is assumed. For a given M_T, the electrical field resulting from MC simulations is compared to the fields from the analytic CCF and CMP models, as shown in Fig. 2. The CMP model is exact in the limit $M_T \to \infty$, where it yields the relation $M_T = \sqrt{\frac{2}{\pi}eE_{\rm CMP}\ell/T_n}$,[32] so that the ratio $E_{\rm CMP}/E_{\rm MC}$ tends to unity in this regime. We see that the CMP model is reasonably (within 10%) accurate at $M_T \gtrsim 4-5$. To make the direct comparison with the CCF model, we employ the exact solution of the kinetic equation obtained in the regime of infinitesimal M_T,[43] which yields $M_T = 0.341eE\ell/T_n$. Hence, the CCF model is exact in the limit $M_T \to 0$ when the collision frequency is equal to $\nu = 2.93v_T/\ell$. The resulting ratio $E_{\rm CCF}/E_{\rm MC}$ (tending to unity at $M_T \to 0$) decreases fairly rapidly with M_T. We conclude that the CCF model provides the 10% accuracy at $M_T \lesssim 0.8$.

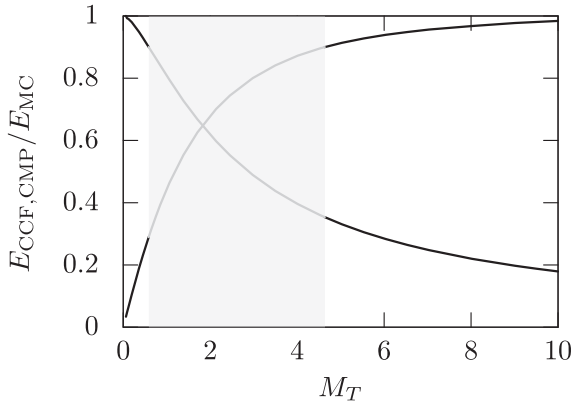

FIG. 2. Ratio of the electric field corresponding to a given thermal Mach number M_T in the CCF (CMP) analytic model, $E_{\rm CCF}$ ($E_{\rm CMP}$), to the electric field in MC simulations, $E_{\rm MC}$. The curve tending to unity at $M_T = 0$ represents the comparison of the CCF model with simulations, $E_{\rm CCF}/E_{\rm MC}$, the curve approaching unity at large M_T shows $E_{\rm CMP}/E_{\rm MC}$. The shadowed "gray zone" indicates the range of M_T where neither analytic model provides acceptable accuracy ($\leq 10\,\%$).

The agreement between the analytic models and MC simulations is further illustrated in Fig. 3 showing the corresponding longitudinal (averaged over the transverse velocities) ion velocity distribution functions $f_z(v_z)$. We see that for subthermal ion flows ($M_T = 0.5$) the MC curve can indeed be very well approximated by the CCF model, while at $M_T = 1$, the deviation becomes noticeable. Similarly, the deviation between the CMP model and simulations is significant for moderately suprathermal flows ($M_T = 4$), whereas at $M_T = 10$, the CMP model is reasonably accurate. The deviation from the half-Maxwellian form (at $|v_z|/v_T \lesssim 3$) plays only a minor role in the latter case. A noteworthy fact we found is that Eq. (3) from Ref. 31 (CCF approximation) quite accurately describes the left branch of $f_z(v_z)$ (i.e., where $df_z/dv_z > 0$) for *any* M_T.

A. Wake in subthermal regime: CCF model

For the CCF model, the reciprocal (dispersion) elements of $\mathsf{D}_\mathbf{k}$ remain practically the same as in the Yukawa/point-wake model.[13] This is because the "wake contribution" to the plasma permittivity is quite small in the subthermal regime. In this case, the diagonal dispersion elements for the in-plane mode are degenerate, $\alpha_x = \alpha_y$, and the screening is determined by the linearized local Debye length, $\lambda^{-2} = \lambda_{{\rm D}i}^{-2} + \lambda_{{\rm D}e}^{-2}$, where $\lambda_{{\rm D}i,e} = \sqrt{T_{i,e}/4\pi e^2 n_{i,e}}$ are the electron and ion Debye lengths.[2] Note that in the subthermal regime $T_i \simeq T_n$ and hence, $\lambda_{{\rm D}e} \gg \lambda_{{\rm D}i}$, i.e., $\lambda \simeq \lambda_{{\rm D}i}$.

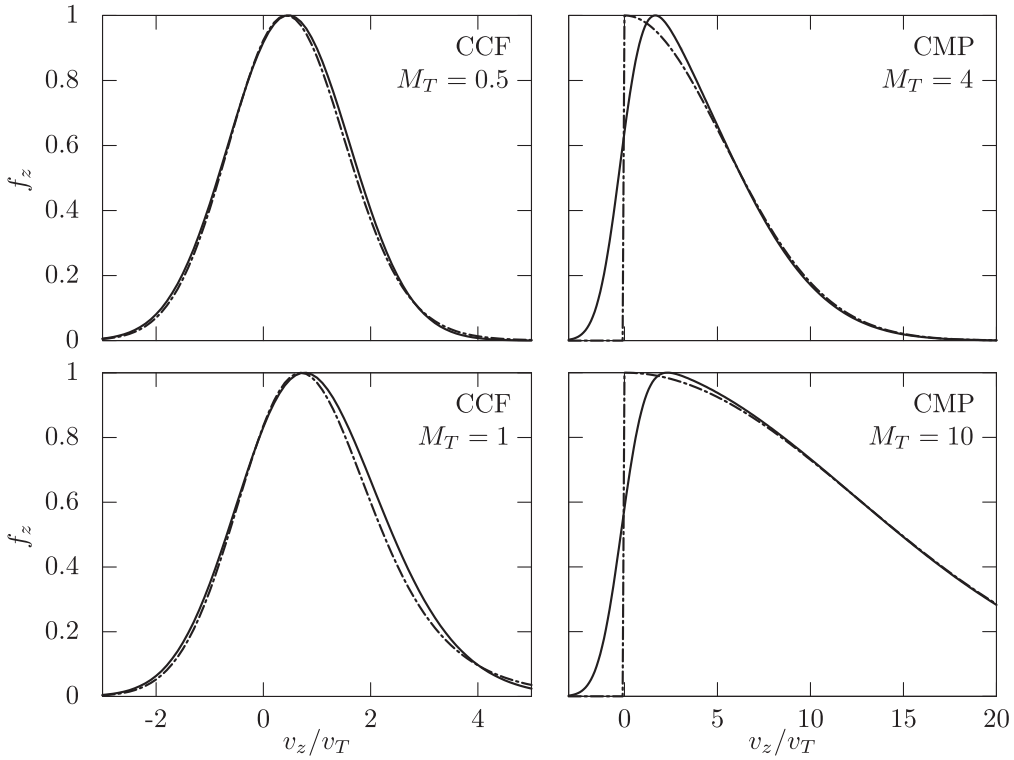

FIG. 3. The longitudinal ion velocity distribution functions $f_z(v_z)$. Shown are the results of MC simulation (solid lines) compared with the analytical results (dashed-dotted lines): CCF model (Eq. (3) from Ref. 31) in the left panel, and CMP model (Eq. (3) from Ref. 32) in the right panel. The distributions are normalized by the maximal values, velocity is normalized by v_T.

By introducing $K \equiv \kappa s$ for brevity, we obtain the following expressions for the dispersion elements:

$$\{V\} = \sum_{m,n} \{v\} \frac{e^{-K}}{K^3} \sin^2 \frac{1}{2} \mathbf{k} \cdot \mathbf{s},$$

$$\{v\} = \left\{ K^2 + K + 1 - \frac{s_y^2 - s_x^2}{s^2}(K^2 + 3K + 3), K^2 + K + 1 \right.$$
$$\left. + \frac{s_y^2 - s_x^2}{s^2}(K^2 + 3K + 3), \frac{s_y s_x}{s^2}(K^2 + 3K + 3), K + 1 \right\}. \quad (6)$$

The coupling elements

$$\sigma_{\{x,y\}} = \frac{M_T}{2\sqrt{2\pi}} \sum_{m,n} \left[\left(\frac{3}{K^4} + \frac{2}{K^2} \right) F_+(K) \right.$$
$$\left. - \left(\frac{3}{K^3} + \frac{1}{K} \right) F_-(K) - \frac{6}{K^3} \right] \frac{s_{\{x,y\}}}{s} \sin \mathbf{k} \cdot \mathbf{s} \quad (7)$$

are expressed via the auxiliary functions

$$F_\pm(x) = e^x E_1(x) \pm e^{-x} E^*(x),$$

written in terms of exponential integral functions $E_1(x)$ and $E^*(x)$.[44] Figure 4 (upper panel) shows that, unlike the dispersion elements, the coupling elements for the CCF and Yukawa/point-wake models (plotted along the respective principal lattice directions) are quite different.

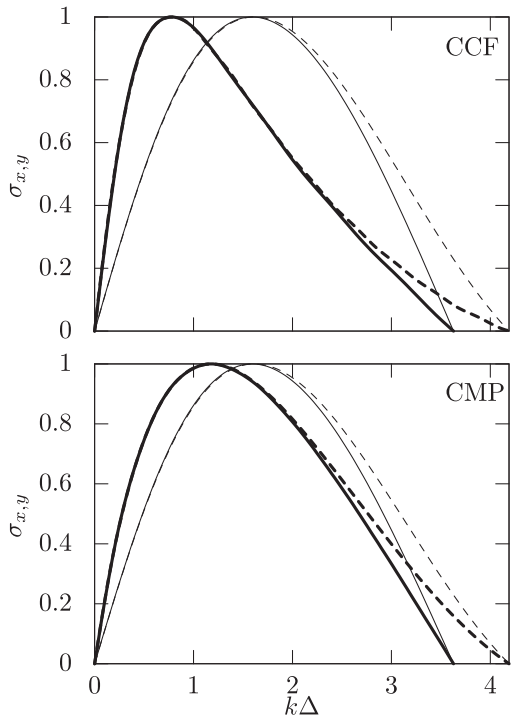

FIG. 4. The coupling elements of the dynamical matrix $\sigma_{x,y}$ (normalized by the maximal values) vs. the absolute value of the wave vector $k_{x,y}$ (normalized by Δ) along the respective principal lattice direction. Shown is the comparison of the CCF model (upper panel) and CMP model (lower panel) with the Yukawa/point-wake model. The thick solid (thick dashed) line shows σ_x (σ_y) obtained from Eq. (7) (CCF) and Eq. (10) (CMP), the thin solid (thin dashed) line represents σ_x (σ_y) for the Yukawa/point-wake model, Eq. (5) from Ref. 13. The results are for $\kappa = 1$.

B. Wake in suprathermal regime: CMP model

The CMP model corresponds to the highly suprathermal regime, where all elements of the dynamical matrix change significantly. As compared to the Yukawa/point-wake model,[13] the numerical convergence of Eqs. (4) and (5) in this case is slower, since interactions on intermediate scales (several screening lengths) are more important. The CMP model is characterized by the "self-consistent" screening length,[32,33]

$$\lambda_{\rm sc} = \sqrt{\frac{eE_0\ell}{4\pi e^2 n_{i0}}} \equiv \sqrt{\frac{\pi}{2}} M_T \lambda_{{\rm D}i}, \tag{8}$$

which is determined by the local ion Debye length $\lambda_{{\rm D}i}$ and depends on the Mach number. The elements of the dynamical matrix are[33]

$$\{V\} = \sum_{m,n} \{v\} \sin^2 \frac{1}{2} \mathbf{k}\cdot\mathbf{s},$$
$$\{v\} = \left\{ Z^{(1)} \frac{s_x^2}{s^2} - \frac{Z^{(3)}}{\zeta\kappa} \frac{s_x^2 - s_y^2}{s^3},\ Z^{(1)} \frac{s_y^2}{s^2} + \frac{Z^{(3)}}{\kappa\zeta} \frac{s_x^2 - s_y^2}{s^3},\right.$$
$$\left. \left(sZ^{(1)} + 2\frac{Z^{(3)}}{\kappa\zeta} \right) \frac{s_x s_y}{s^3},\ Z^{(2)} \right\}, \tag{9}$$

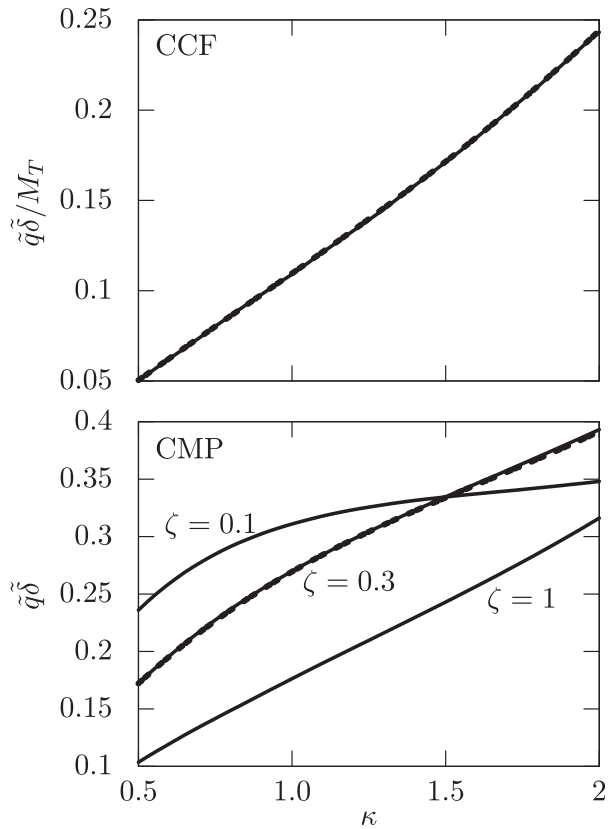

FIG. 5. The effective wake dipole moment $\tilde{q}\tilde{\delta}$ versus the screening parameter κ. The upper panel shows the universal dependence $\tilde{q}\tilde{\delta}/M_T$ vs. κ derived from the CCF model (subthermal regime); the solid line represents the dependence for the wave vector along x-axis (for the y-direction the difference is within 3%), the double-dashed line is the cubic polynomial fit, Eq. (11). The lower panel shows the dependence $\tilde{q}\tilde{\delta}$ vs. κ derived from the CMP model (suprathermal regime) for three values of $\zeta = \lambda_{\rm sc}/\ell$; the solid lines are for the wave vector along x-axis (for the y-direction the difference is within 1%), the double-dashed line is the cubic polynomial fit for $\zeta = 0.3$, Eq. (12).

and

$$\sigma_{\{x,y\}} = \sum_{m,n} Z^{(4)} \frac{s_{\{x,y\}}}{s} \sin \mathbf{k}\cdot\mathbf{s}. \tag{10}$$

Here, we introduced the following integrals:

$$Z^{\{(1),(2)\}} = \Re \int_0^\infty dt \frac{\{h_\zeta^2(t), t^2\}}{g_\zeta(t)} K_0[\zeta K h_\zeta(t)],$$

$$Z^{\{(3),(4)\}} = \Re \int_0^\infty dt \frac{h_\zeta(t)}{g_\zeta(t)} \{1, -it\} K_1[\zeta K h_\zeta(t)],$$

where $K_0(x)$ and $K_1(x)$ are the modified Bessel functions of zeroth and first order, respectively. The auxiliary functions used in $Z^{(j)}$ read

$$h_\zeta(t) = \sqrt{\frac{\zeta^2 t^2 + 1 - \sqrt{1+it}}{\frac{4}{\pi}\zeta^5 g_\zeta(t)}},$$

$$g_\zeta(t) = \frac{\pi}{4}\zeta^{-5} \times \left\{ \zeta^2 - \frac{1}{it(1+it)} + \frac{2\sqrt{1+it}}{it} \int_0^1 \frac{d\alpha}{[1+it(1-\alpha^2)]^2} \right\},$$

where all square roots should be taken with a positive real part. Note that now α_x and α_y are different from each other. The resulting coupling elements are shown in Fig. 4 (lower panel).

There are two parameters governing the behavior of the dynamical matrix in the CMP model: the screening parameter $\kappa = \Delta/\lambda_{\rm sc}$ and the collision parameter $\zeta = \lambda_{\rm sc}/\ell$. The thermal Mach number is included in the model via the scaling $\lambda_{\rm sc} \propto M_T$, Eq. (8), i.e., both κ and ζ are functions of M_T.

IV. MAPPING OF YUKAWA/POINT-WAKE MODEL TO CCF AND CMP MODELS

The main observable feature of MCI is the emergence of the hybrid mode whose "intensity" is governed by the *maximum* growth rate. The latter depends on the vertical confinement eigenfrequency $\Omega_{\rm conf}$ and is proportional to the *maximum* of the coupling elements $\sigma_{x,y}(\mathbf{k})$[17] shown in Fig. 4. Note that the threshold (critical) damping rate $\nu_{\rm dn}^{\rm (cr)}$ necessary to suppress the MCI is twice the maximum growth rate (see Fig. 7(b) and Sec. III D 2 in Ref. 17).

The functions $\sigma_{x,y}(\mathbf{k})$ for the Yukawa/point-wake model and those for the CCF or CMP models do not coincide, as one can see from Fig. 4. Nevertheless, their overall shape appears to be similar. Therefore, we propose to specify the effective dipole moment $\tilde{q}\tilde{\delta}$ by *matching* the corresponding maxima of either σ_x or σ_y.

The results of this "mapping" of the CCF model (representing the subthermal regime) to the Yukawa/point-wake model are shown in Fig. 5 (upper panel). It turns out that the ratio $\tilde{q}\tilde{\delta}/M_T$ depends only on κ. The results are presented for the (experimentally relevant) interval $0.5 < \kappa < 2$. Given

TABLE I. Data available from 2D complex plasma experiments performed in an argon discharge. For each experiment, the particle diameter 2 a, absolute value of charge $|Q|$, mass m, and gas pressure p are shown, as well as the corresponding levitation electric field E_0, ion mean free path ℓ, and the thermal Mach number M_T. Also, the collision parameter ζ (where appropriate) and screening parameter κ are presented. The last two columns show the effective wake dipole moments deduced from experiments/simulations, $(\tilde{q}\tilde{\delta})_{\text{pub}}$, and calculated theoretically from our mapping procedure, $\tilde{q}\tilde{\delta}$.

Ref.	$2a$ (μm)	$\lvert Q\rvert$ (10^3 e)	m (10^{-14} kg)	E_0 (V/cm)	p (Pa)	ℓ (mm)	ζ	κ	M_T	$(\tilde{q}\tilde{\delta})_{\text{pub}}$	$\tilde{q}\tilde{\delta}$
47	4.8	7.3	8.8	7.4[a]	2.9	—	—	—	0.8[a]	—	0.09[b]
48[c]	6.5	10.0	22	13.5	4.7	1.57	0.38	0.67	6.0	—	0.20
47	8.9	15.2	56	22.4[a]	2.9	—	—	—	7.2[a]	—	0.29[b]
12	8.9	15.5	55	21.7	2.8	2.64	0.19	1.1	10.3	0.25[e]	0.30
16[d]	8.09	12.0	42	21.4	2.67	2.77	0.27	0.79	10.5	0.26	0.24
49[c]	8.9	16.0	56	21.4	1.0	7.39	0.13	0.75	17.6	—	0.27
46[d]	8.77	18.0	53	18.0	0.76	9.73	0.06	1	18.6	—	0.29
14[d]	9.19	18.3	61	20.4	0.76	9.73	0.06	1.05	19.8	0.1[f]	0.30

[a]Calculated from data presented in Ref. 47.
[b]Assuming $\kappa = 1$.
[c]Experiment with gas flow.
[d]Experiment with mode coupling.
[e]Used in simulations.
[f]Obtained by comparing with fluctuation spectra.

the fact that the MCI sets in first for $\mathbf{k}$ along the x-axis[13] (i.e., for $\theta = 0^\circ$ in Fig. 1(a)) we show only this case. The universal dependence can be fitted with the following polynomial:

$$\tilde{q}\tilde{\delta}/M_T \simeq 0.0105\kappa^3 - 0.0259\kappa^2 + 0.139\kappa - 0.0139. \quad (11)$$

In the suprathermal regime, the mapping of the CMP model yields an effective dipole moment $\tilde{q}\tilde{\delta}$ which depends on the collision parameter ζ as well as on κ. The results are shown in Fig. 5 (lower panel). For a given ζ, the mapping curve $\tilde{q}\tilde{\delta}(\kappa)$ is very well fitted with a third-order polynomial. For instance, assuming $\zeta = 0.3$ (which corresponds to the experiment of Ref. 32, see Table I), we obtain

$$\tilde{q}\tilde{\delta} \simeq 0.035\kappa^3 - 0.17\kappa^2 + 0.39\kappa + 0.015. \quad (12)$$

Summarizing Fig. 5, we conclude that in the subthermal regime the normalized wake dipole moment is directly proportional to the Mach number M_T, and increases almost linearly with the screening parameter κ. In the suprathermal regime, where both κ and ζ are functions of M_T [see Eq. (8)], the κ-scaling is essentially nonlinear and the dependence on ζ is non-monotonic.

V. DISCUSSION AND CONCLUSION

Previously, the effective dipole moment could only be roughly estimated from the intensity of "hot spots" in the experimentally measured phonon fluctuation spectra. In this paper, we propose the methodology to assign a value to the dipole moment from first principles. This allows us to specify the dependence of the dipole moment on experimentally "accessible" quantities (e.g., particle charge, mass, Debye length, Mach number, ion-neutral mean free path).

Table I illustrates how our theoretical results can be applied to experiments with 2D complex plasmas. It summarizes all essential parameters which determine the value of the effective wake dipole moment. The table covers a broad range of the Mach numbers ($M_T \simeq 1 - 20$), screening parameters ($\kappa \simeq 0.7 - 1.1$), and collision parameters ($\zeta \simeq 0.06 - 0.4$) achievable in experiments, all resulting in a rather narrow range of the normalized dipole moments ($\simeq 0.1 - 0.3$) presented in the last two columns. Here, we show the dipole moments $(\tilde{q}\tilde{\delta})_{\text{pub}}$ deduced from published experiments/simulations (where available) and the corresponding theoretical values $\tilde{q}\tilde{\delta}$ which are derived from the proposed mapping procedure.

In order to obtain the theoretical dipole moment for each experiment, we first calculated the levitation electric field E_0 from Eq. (1) using the measured values of the particle charge Q and mass m. The ion drag force F_{id} was estimated from Ref. 45; for most experiments, it turned out to be smaller than 10% of mg and therefore was neglected (for the same reason, the vertical induced force $F_{\text{id}}^{(\text{ind})}$ was neglected as well). Then M_T was estimated assuming the mobility-limited ion drift, for which the ion mean free path ℓ corresponding to the experimental pressure was employed (with the cross section from Ref. 42).

Among available experiments, we found one performed in the regime of subthermal ion flow,[47] for which we applied the CCF model (first row of Table I). All other experiments[12–16,46–49] correspond to a highly suprathermal regime (listed by increasing M_T) and, hence, the CMP model was used for their analysis (in this case, the "self-consistent" screening length $\lambda_{\text{sc}}(M_T)$ was employed to calculate κ). We see that the theoretical values $\tilde{q}\tilde{\delta}$ agree very well with $(\tilde{q}\tilde{\delta})_{\text{pub}}$ from Refs. 12 and 16, whereas for Ref. 14, the deviation is relatively large. We attribute the latter to the fact that Couëdel *et al.*[14] obtained $(\tilde{q}\tilde{\delta})_{\text{pub}}$ by comparing the theoretical dispersion relations with fluctuation spectra, whereas the comparison in terms of the growth rate (e.g., by using the local intensity of the hybrid mode) was not carried out. In this respect, the fact that the two completely different approaches yield comparable dipole moments can be considered as a good agreement.

To conclude, in this paper we proposed a general and relatively straightforward model allowing us to "map"

available self-consistent kinetic models of the interparticle interaction on the Yukawa/point-wake model commonly employed in the MCI theory of 2D plasma crystals. The Yukawa/point-wake model is characterized by the effective dipole moment which determines the pressure threshold of the MCI. Here, we used two self-consistent models, CCF and CMP, both derived in the framework of linear response formalism for ions, in the regimes of constant collision frequency and constant mean free path, respectively (which allowed us to cover both subthermal and suprathermal regimes of the ion flow). The theoretical values of the dipole moments derived from the mapping, $\tilde{q}\tilde{\delta}$, are in quite reasonable agreement with the values $(\tilde{q}\tilde{\delta})_{\mathrm{pub}}$ deduced from several available experiments/simulations. Therefore, we hope that the proposed method of evaluating the wake dipole moment will be a useful, practical tool for the analysis of experiments on the wake-induced melting of 2D plasma crystals.

ACKNOWLEDGMENTS

We appreciate funding from the European Research Council under the European Union's Seventh Framework Programme (FP7/2007-2013)/ERC Grant agreement 267499. M.L. and G.J. appreciate the hospitality and encouragement of the Plasma Physics Division of the Naval Research Laboratory.

[1]G. E. Morfill and A. V. Ivlev, Rev. Mod. Phys. **81**, 1353 (2009).
[2]V. E. Fortov, A. V. Ivlev, S. A. Khrapak, A. G. Khrapak, and G. E. Morfill, Phys. Rep. **421**, 1 (2005).
[3]C. A. Knapek, A. V. Ivlev, B. A. Klumov, G. E. Morfill, and D. Samsonov, Phys. Rev. Lett. **98**, 015001 (2007).
[4]C. A. Knapek, D. Samsonov, S. Zhdanov, U. Konopka, and G. E. Morfill, Phys. Rev. Lett. **98**, 015004 (2007).
[5]V. Nosenko, S. K. Zhdanov, A. V. Ivlev, C. A. Knapek, and G. E. Morfill, Phys. Rev. Lett. **103**, 015001 (2009).
[6]O. S. Vaulina and S. A. Khrapak, JETP **90**, 287 (2000).
[7]O. S. Vaulina and S. A. Khrapak, JETP **92**, 228 (2001).
[8]A. Schella, T. Miksch, A. Melzer, J. Schablinski, D. Block, A. Piel, H. Thomsen, P. Ludwig, and M. Bonitz, Phys. Rev. E **84**, 056402 (2011).
[9]S. A. Khrapak, M. Chaudhuri, and G. E. Morfill, J. Chem. Phys. **134**, 241101 (2011).
[10]O. S. Vaulina and X. G. Koss, Phys. Lett. A **373**, 3330 (2009).
[11]A. V. Ivlev and G. Morfill, Phys. Rev. E **63**, 016409 (2001).
[12]A. V. Ivlev, G. Joyce, U. Konopka, and G. Morfill, Phys. Rev. E **68**, 026405 (2003).
[13]S. K. Zhdanov, A. V. Ivlev, and G. E. Morfill, Phys. Plasmas **16**, 083706 (2009).
[14]L. Couëdel, V. Nosenko, A. V. Ivlev, S. K. Zhdanov, H. M. Thomas, and G. E. Morfill, Phys. Rev. Lett. **104**, 195001 (2010).
[15]B. Liu, J. Goree, and Yan Feng, Phys. Rev. Lett. **105**, 085004 (2010).
[16]B. Liu, J. Goree, and Yan Feng, Phys. Rev. Lett. **105**, 269901 (2010).
[17]L. Couëdel, S. K. Zhdanov, A. V. Ivlev, V. Nosenko, H. M. Thomas, and G. E. Morfill, Phys. Plasmas **18**, 083707 (2011).
[18]S. V. Vladimirov and M. Nambu, Phys. Rev. E **52**, R2172 (1995).
[19]O. Ishihara and S. V. Vladimirov, Phys. Plasmas **4**, 69 (1997).
[20]F. Melandso and J. Goree, Phys. Rev. E **52**, 5312 (1995).
[21]M. Lampe, G. Joyce, G. Ganguli, and V. Gavrishchaka, Phys. Plasmas **7**, 3851 (2000).
[22]A. Samarian, S. Vladimirov, and B. James, JETP Lett. **82**, 758 (2005).
[23]S. V. Vladimirov and A. A. Samarian, Phys. Rev. E **65**, 046416 (2002).
[24]A. Melzer, V. A. Schweigert, and A. Piel, Phys. Scr. **61**, 494 (2000).
[25]J. H. Chu and I. Lin, Phys. Rev. Lett. **72**, 4009 (1994).
[26]H. Thomas, G. E. Morfill, V. Demmel, J. Goree, B. Feuerbacher, and D. Möhlmann, Phys. Rev. Lett. **73**, 652 (1994).
[27]A. Melzer, V. A. Schweigert, and A. Piel, Phys. Rev. Lett. **83**, 3194 (1999).
[28]A. Melzer, V. A. Schweigert, I. V. Schweigert, A. Homann, S. Peters, and A. Piel, Phys. Rev. E **54**, R46 (1996).
[29]G. Joyce, M. Lampe, and G. Ganguli, IEEE Trans. Plasma Sci. **29**, 238 (2001).
[30]G. Joyce, M. Lampe, and G. Ganguli, Phys. Rev. Lett. **88**, 095006 (2002).
[31]A. V. Ivlev, S. K. Zhdanov, S. A. Khrapak, and G. E. Morfill, Phys. Rev. E **71**, 016405 (2005).
[32]R. Kompaneets, U. Konopka, A. V. Ivlev, V. Tsytovich, and G. E. Morfill, Phys. Plasmas **14**, 052108 (2007).
[33]T. B. Röcker, A. V. Ivlev, R. Kompaneets, and G. E. Morfill, Phys. Plasmas **19**, 033708 (2012).
[34]E. M. Lifshitz and L. P. Pitaevskii, *Physical Kinetics* (Pergamon, Oxford, 1981).
[35]Yu. P. Raizer, *Gas Discharge Physics* (Springer, Berlin, 1991).
[36]P. L. Bhatnagar, E. P. Gross, and M. Krook, Phys. Rev. **94**, 511 (1954).
[37]S. Robertson and Z. Sternovsky, Phys. Rev. E **67**, 046405 (2003).
[38]D. Else, R. Kompaneets, and S. V. Vladimirov, Phys. Plasmas **16**, 062106 (2009).
[39]M. Zeuner and J. Meichsner, Vacuum **46**, 151 (1995).
[40]G. H. Wannier, Bell Syst. Tech. J. **32**, 170 (1953).
[41]E. W. McDaniel, *Collision Phenomena in Ionized Gases* (Wiley, New York, 1964).
[42]J. A. Hornbeck and G. H. Wannier, Phys. Rev. **82**, 458 (1951).
[43]B. M. Smirnov, Sov. Phys. Tech. Phys. **11**, 1388 (1967).
[44]W. J. Cody and H. C. Thacher, Jr., Math. Comput. **22**, 641 (1968); **23**, 289 (1969).
[45]S. A. Khrapak, A. V. Ivlev, S. K. Zhdanov, and G. E. Morfill, Phys. Plasmas **12**, 042308 (2005).
[46]L. Couëdel, V. Nosenko, S. K. Zhdanov, A. V. Ivlev, H. M. Thomas, and G. E. Morfill, Phys. Rev. Lett. **103**, 215001 (2009).
[47]U. Konopka, *Wechselwirkungen geladener Staubteilchen in Hochfrequenzplasmen*, Ph.D. dissertation, Ruhr-University Bochum, 2000.
[48]P. Hartmann, A. Douglass, J. C. Reyes, L. S. Matthews, T. W. Hyde, A. Kovacs, and Z. Donko, Phys. Rev. Lett. **105**, 115004 (2010).
[49]D. Samsonov, S. Zhdanov, and G. Morfill, Phys. Rev. E **71**, 026410 (2005).

Effect of strong wakes on waves in two-dimensional plasma crystals

T. B. Röcker,* A. V. Ivlev,† S. K. Zhdanov, and G. E. Morfill
Max Planck Institute for Extraterrestrial Physics, 85741 Garching, Germany
(Received 28 August 2013; published 15 January 2014)

We study the effects of the particle-wake interactions on the dispersion and polarization of dust lattice wave modes in two-dimensional plasma crystals. Most notably, the wake-induced coupling between the modes causes the branches to "attract" each other, and their polarizations become elliptical. Upon the mode hybridization the major axes of the ellipses (remaining mutually orthogonal) rotate by 45°. To demonstrate the importance of the obtained results for experiments, we plot representative particle trajectories and spectral densities of the longitudinal and transverse waves. These characteristics reveal distinct fingerprints of the mixed polarization. Furthermore, we show that at strong coupling the hybrid mode is significantly shifted towards smaller wave numbers, away from the border of the first Brillouin zone (where the hybrid mode is localized for a weak coupling).

DOI: 10.1103/PhysRevE.89.013104 PACS number(s): 52.27.Lw, 52.27.Gr, 52.35.−g

I. INTRODUCTION

A complex (dusty) plasma consists of a weakly ionized gas and small solid particles (also referred to as "dust" or "grains"), which are charged negatively due to absorption of the surrounding electrons and ions and typically carry some thousands electron charges [1–5]. The name was chosen in analogy to complex liquids due to the fact that complex plasmas can be regarded as a new (plasma) state of soft matter [6]. Under certain conditions, strongly coupled complex plasmas can be treated as a *single-species* weakly damped medium whose interparticle interactions are determined by the surrounding electrons and ions [7].

Experimentally, solid-state complex plasmas ("plasma crystals") are produced by injecting monodisperse microparticles in a low-pressure gas-discharge plasma [8,9]. In ground-based experiments performed in radio-frequency (rf) discharges, the particles are normally levitated in the (pre)sheath above the powered horizontal rf electrode, where the balance of a (highly inhomogeneous) electrostatic force and gravity produces a strong vertical confinement [5,7]. This provides excellent conditions to create two-dimensional (2D) crystalline monolayers of particles with the hexagonal order, as shown in Fig. 1(a).

The (pre)sheath electric field generates a strong vertical plasma flow. This produces a perturbed region downstream each particle, which is called "plasma wake" (or simply "wake") [10,11]. The electrostatic potential of the wake has been calculated analytically (by employing the linear-response formalism) and numerically (by using particle-in-cell simulations) in very many papers, assuming different models for the ion velocity distribution and ion collisionality, see, e.g. [12–19].

The wakes couple the horizontal and vertical motion of particles in the monolayer. The particle-wake interactions are nonreciprocal [20], and therefore under certain conditions the total kinetic energy of the ensemble is no longer conserved: As was shown by Ivlev and Morfill [21], when the horizontal and vertical motions are in resonance (which occurs when the out-of-plane and longitudinal in-plane wave modes intersect) the *mode-coupling instability* sets in. When the gas pressure is low enough and the instability cannot be suppressed by friction, microparticles acquire anomalously high kinetic energy and the crystal melts. The mode-coupling instability and the associated melting have been investigated in numerous theoretical [22–24] and experimental works [25–30].

Self-consistent wake models provide better agreement with experimental results [23,24]. Nevertheless, many theoretical investigations of the mode-coupling instability are still based on a simple "Yukawa/point-wake model" [21,22] since it makes the analysis of new qualitative effects associated with particle-wake interaction more transparent. In this model, the wake is considered as a positive, point-like effective charge q located at the distance δ below each particle (of charge Q). Thus, the total interaction between two particles is a simple superposition of the particle-particle and particle-wake interactions, both described by the (spherically symmetric) Yukawa potentials with effective screening length λ. For a given screening parameter $\kappa = \Delta/\lambda$ the effective dipole moment of wake

$$\tilde{d}_{\rm eff} = \frac{\tilde{q}\tilde{\delta}}{1-\tilde{q}} \tag{1}$$

(normalized by $Q\Delta$ and expressed in terms of the dimensionless wake charge $\tilde{q} = q/Q$ and distance $\tilde{\delta} = \delta/\Delta$) determines the growth rate of the mode-coupling instability [30].

The effective dipole moment is related to parameters of the ambient plasma and can be fairly large for typical experimental conditions [24]. On the other hand, the theoretical analysis of the mode coupling performed so far was primarily focused on the limit of small $\tilde{d}_{\rm eff}$ [21,22,30]. The question of how the wave modes are modified at large (but still experimentally accessible) values of $\tilde{d}_{\rm eff}$ remains open. Furthermore, while uncoupled in-plane and out-of-plane wave modes (corresponding to purely horizontal and vertical motion, respectively) are linearly polarized, the polarization of waves with a *strong* wake-induced coupling (when $\tilde{d}_{\rm eff}$ cannot be considered as a small parameter) is a fundamental question which has never been systematically studied.

*tbr@mpe.mpg.de
†ivlev@mpe.mpg.de

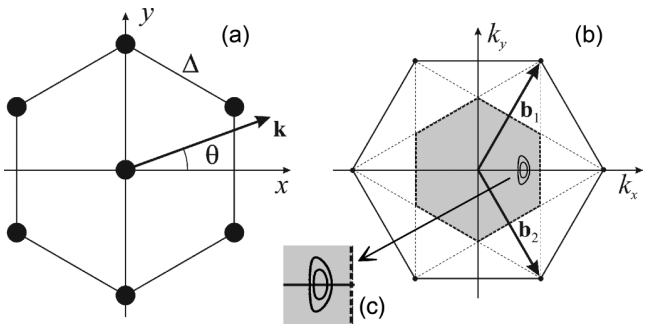

FIG. 1. (a) Elementary hexagonal lattice cell with the frame of reference. (b) The reciprocal lattice in $\mathbf{k}$ space with the basis vectors $|\mathbf{b}_1| = |\mathbf{b}_2| = \frac{4\pi}{\sqrt{3}}\Delta^{-1}$. Due to the lattice symmetry, it is sufficient to consider the wave vectors $\mathbf{k}$ at $0^\circ \leqslant \theta \leqslant 30^\circ$ and from within the first Brillouin zone (gray region enclosed by dashed lines), so that $|\mathbf{k}|\Delta \leqslant \frac{2\pi}{\sqrt{3}}$ for $\theta = 0^\circ$ and $|\mathbf{k}|\Delta \leqslant \frac{4\pi}{3}$ for $\theta = 30^\circ$. (c) Enclosed regions where the particle-wake interactions cause the in-plane and out-of-plane wave modes to merge and form the hybrid mode [see also Fig. 2(c)]. The smaller (larger) region corresponds to the effective dipole moment of wake $\tilde{d}_{\rm eff} = 0.7(0.71)$ [Eq. (1)], the screening parameter is $\kappa = 1$, the normalized eigenfrequency of the vertical confinement is $\Omega_{\rm conf} = 5.66$.

In this paper we investigate the regime of *strong* wake-induced coupling between wave modes in 2D plasma crystals. In Sec. II we compare the weak and strong coupling regimes and point out their essential differences. The polarization of separate and hybrid wave modes are discussed in Sec. III. To demonstrate the importance of the obtained results for experiments and demonstrate distinct fingerprints of the mixed polarization upon the strong coupling, in Sec. IV we plot the representative particle trajectories and spectral densities of the longitudinal and transverse waves, and calculate the shift of the hybridization point.

We normalize the wave number k by the lattice constant Δ, and all frequencies by the dust-lattice frequency scale

$$\Omega_{\rm DL} = \sqrt{\frac{(1-\tilde{q})Q^2}{M\lambda^3}}, \tag{2}$$

viz.,

$$k\Delta \to k, \quad \omega/\Omega_{\rm DL}, \Omega/\Omega_{\rm DL} \to \omega, \Omega,$$

where M is the particle mass [21,22].

II. WEAK AND STRONG MODE COUPLING

The wake-induced coupling of the in-plane and out-of-plane modes is most efficient for the propagation direction $\theta = 0^\circ$ [22,30], when $\mathbf{k} = k\hat{\mathbf{e}}_x$ [see Fig. 1(a)]. In this case, the in-plane transverse (acoustic "shear") mode becomes exactly decoupled. Therefore, below we assume $\theta = 0^\circ$ and study the coupling between the remaining two modes [21,22].

The exact dispersion relations $\omega(k)$ of the coupled in-plane and out-of-plane wave modes for $\theta = 0^\circ$ are determined by the following equation [21,22,30]:

$$\left[\omega(\omega + i\nu) - \Omega_h^2\right]\left[\omega(\omega + i\nu) - \Omega_v^2\right] + \sigma^2 = 0, \tag{3}$$

where $\Omega_{h,v}(k)$ are the eigenfrequencies of the *horizontal* (in-plane) and *vertical* (out-of-plane) modes in the absence of coupling, $\sigma(k) > 0$ is the coupling term, and ν is the damping rate due to neutral gas friction [31]. The expressions for $\Omega_{h,v}^2$ and σ are given in Appendix A (the wake-free results are obtained by putting the wake charge $\tilde{q}$ equal to zero). Adopting the notation $\Omega^2 = \omega(\omega + i\nu)$, Eq. (3) can be written in a form of the the eigenvalue problem [22,30]

$$\det(\mathsf{D}_k - \Omega^2\mathsf{I}) = 0, \quad \mathsf{D}_k = \begin{pmatrix} \Omega_h^2 & i\sigma \\ i\sigma & \Omega_v^2 \end{pmatrix}, \tag{4}$$

where I denotes the unit matrix and D_k is the non-Hermitian dynamical matrix (note that $\mathsf{D}_k^* = \mathsf{D}_{-k}$). The squared eigenfrequencies of the *lower* and *upper* modes

$$\Omega_{\rm lo,up}^2 = \frac{\Omega_v^2 + \Omega_h^2}{2} \mp \frac{\Omega_v^2 - \Omega_h^2}{2}\sqrt{1-p^2}, \tag{5}$$

are determined by the *reduced coupling parameter* $p(k)$

$$p = \frac{2\sigma}{\Omega_v^2 - \Omega_h^2}. \tag{6}$$

When $p \to 0$ the lower and upper modes are reduced to the horizontal and vertical modes, respectively, i.e., $\Omega_{\rm lo,up}(k) \to \Omega_{h,v}(k)$.

The eigenfrequencies of the upper and lower modes are real and different for $p < 1$; in this regime we shall call the modes *separate*. For $p > 1$ the eigenfrequencies become complex conjugate (i.e., with equal real parts), and therefore the resulting lower and upper modes are referred to as *hybrid*; in this case, $\Omega_{\rm lo,up}$ in Eq. (5) has to be replaced with $\Omega_{\rm lo,up}^{\rm (hyb)}$. The eigenfrequencies of the lower and upper hybrid modes have negative and positive imaginary parts, respectively, so that the former is decaying and the latter is growing. The hybrid modes emerge at the *critical point* $p = 1$, which occurs at the critical wave number $k = k_{\rm cr}$ when the critical confinement $\Omega_{\rm conf} = \Omega_{\rm cr}$ is reached.

Thus, the wake-induced mode coupling can be considered as a *nonequilibrium* second-order phase transition, where p plays the role of the control parameter, while the *imaginary part* of the hybrid eigenfrequency, $\mathrm{Im}\Omega^{\rm (hyb)}$, is the proper order parameter.

The lower and upper modes near the onset of hybridization are illustrated in Figs. 2(a) to 2(c) for three characteristic values of the vertical confinement frequency $\Omega_{\rm conf}$ (for simplicity we consider undamped waves). The corresponding coupling parameters $p(k,\Omega_{\rm conf})$ are plotted in Fig. 2(d), so that $\Omega_{\rm conf}$ plays the role of the control parameter. In Fig. 2(a) the branches $\Omega_{\rm lo}(k)$ and $\Omega_{\rm up}(k)$ are noticeably attracted to each other near $k \simeq 2.7$, where the maximum of $p(k)$ is reached; although $p_{\rm max} \simeq 0.67$ is still well below unity, the deviation from the wake-free results $\Omega_{h,v}(k)$ is already quite significant. In Fig. 2(b), where $p_{\rm max} \simeq 0.97$, one can see that the gap between the modes becomes constricted. In Fig. 2(c), where $\Omega_{\rm conf} > \Omega_{\rm cr}$, the modes merge and form the hybrid branch in the range of k where $p(k) \geqslant 1$ [$\mathrm{Re}\Omega^{\rm (hyb)}(k)$ is shown]. In the $\mathbf{k}$ plane, the hybrid modes are located in an enclosed region, as illustrated in Figs. 1(b) and 1(c).

The magnitude of the coupling term σ is determined by the effective dipole moment of the wake [see, e.g., Eq. (A2)]. For the example presented in Fig. 2 we choose $\tilde{d}_{\rm eff} = 0.7$, which is rather large but quite realistic for experiments (see,

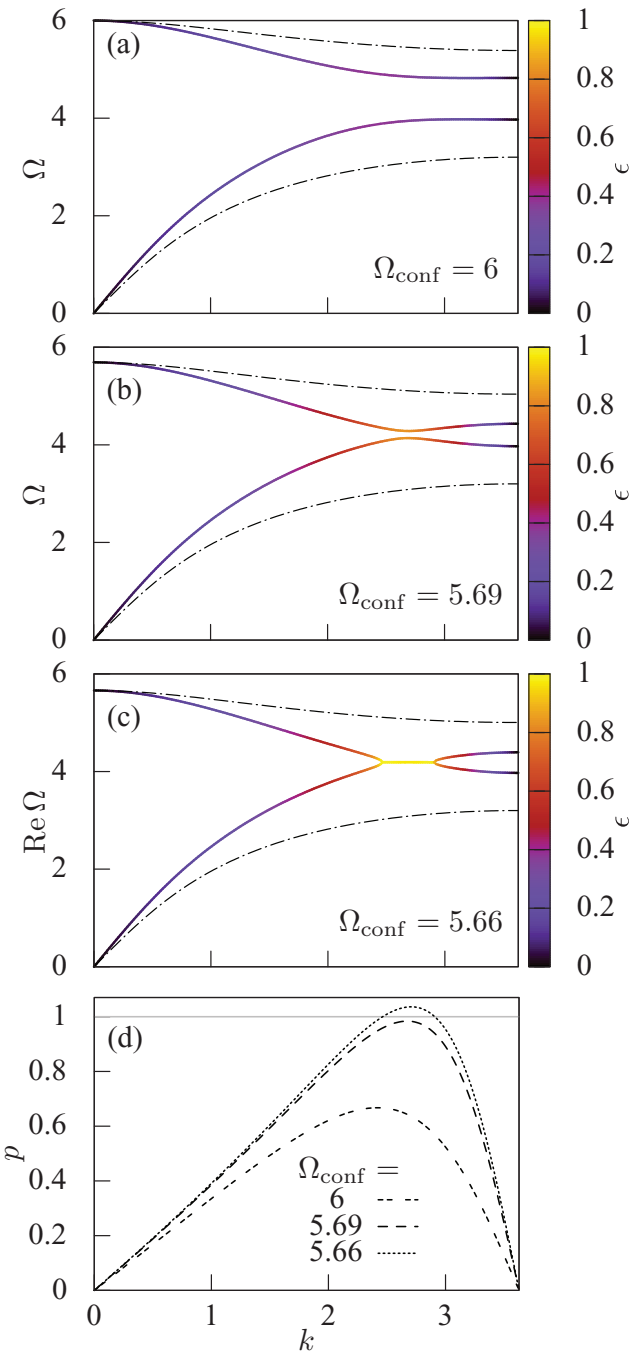

FIG. 2. (Color) Effect of the wake-induced coupling on the wave modes. (a)–(c) The colored lines show the (undamped) dispersion relations of the lower and upper modes $\Omega_{\rm lo,up}(k)$ [Eq. (5)], the dash-dotted lines represent the respective wake-free results $\Omega_{h,v}(k)$ [Eq. (A2) with $\tilde{q} = 0$]. The curves are obtained for three different values of the vertical confinement frequency $\Omega_{\rm conf}$. In (a) the modes are attracted to each other, in (b) the gap between the modes is getting constricted, and in (c) they merge and form the hybrid mode (only the real part is shown). The color-coding shows the circularity of the mode polarization ϵ, which is determined by the reduced coupling parameter [Eqs. (10) and (14) for the separate and hybrid modes, respectively]. (d) The coupling parameter $p(k)$ [Eq. (6)] for panels (a)–(c), the modes merge at $p = 1$. The results are for $\kappa = 1$, the dimensionless wake charge $\tilde{q} = 0.7$, the wake length $\tilde{\delta} = 0.3$ ($\tilde{d}_{\rm eff} = 0.7$).

e.g., [25,27,29]). As we can see, in this case the critical point and hence the hybrid branch are significantly shifted away from the border of the Brioullin zone, where the hybrid mode is localized in the limit of weak coupling [since the uncoupled branches $\Omega_{h,v}(k)$ are monotonic].

The "attraction effect" between the modes seen in Figs. 2(a) to 2(c) has not been carefully studied before since theoretical analysis of the mode coupling performed so far was primarily focused on the limit of small σ [21,22,30]. As we can see from Eq. (6), the critical point in this limit is reached when the uncoupled branches practically cross. From Fig. 2 it is evident that for finite σ the merging occurs well before the crossing (which now corresponds to $p \to \infty$).

In what follows we shall always consider a weak neutral damping, viz., $\nu \ll \Omega_{\rm lo,up}$, which is the typical situation for experiments [25–27]. In this case the dispersion relations $\omega_{\rm lo,up}(k)$ are obtained by simply adding $-\frac{1}{2}\nu$ to the imaginary part of $\Omega_{\rm lo,up}(k)$, i.e.,

$$\omega_{\rm lo,up}(k) \simeq \Omega_{\rm lo,up}(k) - i\frac{\nu}{2}. \tag{7}$$

On the other hand, we shall assume the damping to be sufficiently strong to suppress the mode-coupling instability, viz., $\nu > 2|{\rm Im}\Omega^{\rm (hyb)}(k)|$. This ensures that the kinetic temperature of particles can reach a steady-state level which is low enough to keep the crystalline order, i.e., the hybrid mode can still be observed in experiments.

III. POLARIZATION OF WAVE MODES

From the eigenvectors $\boldsymbol{\zeta}_\alpha$ of the dynamical matrix (where $\alpha = {\rm lo, up}$) we obtain the wave modes $\mathbf{w}_\alpha$. The separate modes are

$$\mathbf{w}_\alpha = \boldsymbol{\zeta}_\alpha e^{ikx - i\omega_\alpha(k)t} + {\rm c.c.}, \tag{8}$$

where c.c. denotes the complex conjugate, and the hybrid modes $\mathbf{w}_\alpha^{\rm (hyb)}$ are similarly obtained from $\boldsymbol{\zeta}_\alpha^{\rm (hyb)}$.

The polarization of the modes can be conveniently characterized by the "real phases"

$$\Phi_\alpha \equiv kx - {\rm Re}\,\Omega_\alpha t,$$

and the "circularity" ϵ: 0 and 1 stand for the linear and circular polarizations, respectively, $0 < \epsilon < 1$ are for elliptical polarization. For the separated and hybridized regimes the circularity is given by certain functions of the reduced coupling parameter p (see below).

A. Separate modes ($p < 1$)

Uncoupled ($p \to 0$) horizontal and vertical wave modes are linearly polarized ($\epsilon \to 0$) and the corresponding dynamical matrix is purely real (Hermitian) [22]. Hence, the uncoupled eigenvectors are mutually orthogonal and real. For finite p we obtain

$$\boldsymbol{\zeta}_{\rm lo} = \frac{(1,\ -i\epsilon)}{\sqrt{1+\epsilon^2}}, \quad \boldsymbol{\zeta}_{\rm up} = \frac{(i\epsilon,\ 1)}{\sqrt{1+\epsilon^2}}, \tag{9}$$

so that $|\boldsymbol{\zeta}_\alpha|^2 = 1$ and the circularity ϵ is the following function of p:

$$\epsilon = p/(1+\sqrt{1-p^2}). \tag{10}$$

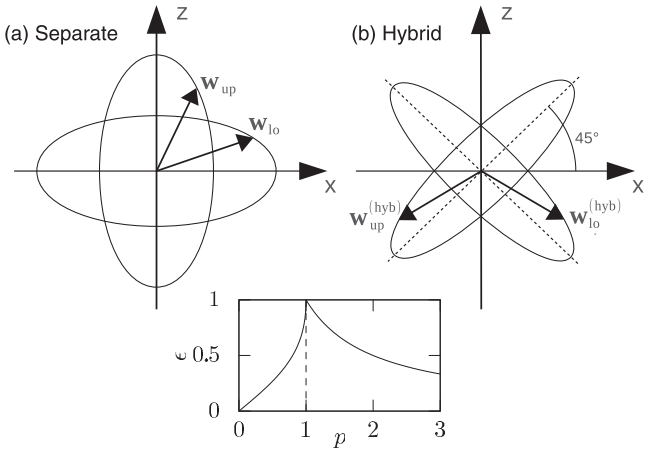

FIG. 3. Lissajous ellipses (a) of the lower and upper *separate* modes, $\mathbf{w}_{lo,up}$ [Eq. (11)], and (b) of the lower and upper *hybrid* modes, $\mathbf{w}_{lo,up}^{(hyb)}$ [Eq. (13)]. For the separate modes the major axes of the ellipses are along the coordinate axes, for the hybrid modes the axes remain mutually orthogonal, but are rotated by 45°. The shape of the ellipses is determined by the circularity ϵ: For $\epsilon = 0$ the ellipses degenerate into lines, for $\epsilon = 1$ they form a circle (the illustration is for $\epsilon = 0.5$). The inset below shows the dependence of ϵ on the reduced coupling parameter p, which is determined by Eqs. (10) and (14) for the separate and hybrid modes, respectively.

Thus, the lower and upper modes expressed via the corresponding wave phases,

$$\mathbf{w}_{lo} = \frac{2e^{-\frac{1}{2}\nu t}}{\sqrt{1+\epsilon^2}}(\cos\Phi_{lo},\ \epsilon\sin\Phi_{lo}),$$
$$\mathbf{w}_{up} = \frac{2e^{-\frac{1}{2}\nu t}}{\sqrt{1+\epsilon^2}}(-\epsilon\sin\Phi_{up},\ \cos\Phi_{up}), \tag{11}$$

are parametric functions of the two ellipses illustrated in Fig. 3(a).

Figure 2 shows that for $k \ll 1$ as well as for k near the border of the first Brillouin zone the coupling parameter p is very small and therefore both $\mathbf{w}_{lo}$ and $\mathbf{w}_{up}$ are linearly polarized ($\epsilon \to 0$). For k where $p \simeq p_{max}$ the circularity becomes significant and the polarization is essentially elliptical. At the points where the upper and lower separate branches merge and form the hybrid branch [Fig. 2(c)] the modes are circularly polarized ($\epsilon = 1$).

B. Hybrid modes ($p \geqslant 1$)

For $p = 1$ the modes are degenerate. Hence, the eigenvectors for the separate modes [Eq. (9)] and hybrid modes should coincide at this point, which yields

$$\boldsymbol{\zeta}_{lo}^{(hyb)} = \frac{1}{\sqrt{2}}(1,\ -i\epsilon - \sqrt{1-\epsilon^2}),$$
$$\boldsymbol{\zeta}_{up}^{(hyb)} = \frac{1}{\sqrt{2}}(i\epsilon + \sqrt{1-\epsilon^2},\ 1). \tag{12}$$

The lower and upper hybrid modes

$$\mathbf{w}_{lo}^{(hyb)} = \sqrt{2}e^{-\frac{1}{2}(\gamma+\nu)t}\ \{\cos\Phi_{lo},\ \sin(\Phi_{lo}-\Phi_0)\},$$
$$\mathbf{w}_{up}^{(hyb)} = \sqrt{2}e^{\frac{1}{2}(\gamma-\nu)t}\ \{-\sin(\Phi_{up}-\Phi_0),\ \cos\Phi_{up}\}, \tag{13}$$

are parametric functions of the two ellipses shown in Fig. 3(b). Here, $\gamma(k) \equiv 2|\mathrm{Im}\Omega^{(hyb)}(k)|$ is the damping (growth) rate of the lower (upper) hybrid mode, the circularity ϵ and phase shift Φ_0 are given by

$$\epsilon = \cos\Phi_0 = p^{-1}. \tag{14}$$

We see that the major polarization axes of the hybrid modes (remaining mutually orthogonal) are rotated by 45° with respect to the axes of separate modes. The rotation occurs discontinuously at $p = 1$ (where the degenerate modes are circularly polarized). Unlike the separate modes, the hybrid mode circularity decreases with p (see inset in Fig. 3), i.e., the hybrid modes are always elliptically polarized between the merging points [see Fig. 2(c)]. Furthermore, upon the crossing of the horizontal and vertical branches $\Omega_v^2 - \Omega_h^2 \to 0$, the coupling p diverges at the crossing point and the polarization of hybrid modes becomes linear near the intersection.

So far, reliable experimental results on the onset of the mode-coupling instability have been only obtained for a slightly overcritical coupling. The reason for that is rather simple: Upon a "deep quenching" the crystal cannot be observed long enough (to deduce sufficiently accurate dispersion relations) before it is completely destroyed by the instability. Such conditions [e.g., of Fig. 2(c)] yield slightly distorted circular polarization ($0.95 \lesssim \epsilon \leqslant 1$) along the whole hybrid branch.

IV. FEATURES OF STRONG COUPLING: EXAMPLES

The strong mode coupling introduces several characteristic features which are expected to be revealed upon analysis of corresponding experiments. Below we discuss some of the most interesting phenomena characterizing the individual particle motion as well as the wave modes near the hybridization point.

A. Particle trajectories

The individual particle trajectories are calculated by applying the inverse Fourier transform (over k) to the wave modes, Eqs. (11) and (13). Thus, each trajectory can be viewed as the weighted "superposition" of the Lissajous ellipses (at a given k), with the weights determined by the magnitudes of the corresponding eigenvectors. The gray lines in Fig. 4 illustrate the resulting steady-state trajectories (when friction is on average balanced by the thermal noise, see Sec. IV B for details) for the separated [Fig. 4(a)] and hybridized [Fig. 4(b)] regimes. The trajectories are shown for the time interval of $50\Omega_{DL}^{-1}$, which corresponds to ~ 3 s under typical experimental conditions [30]. We also draw "orbitals" (solid-line ellipses) to indicate the areas mostly covered by the trajectories (i.e., where particles reside most of the time). Due to stronger vertical confinement in the separated regime [Fig. 4(a)], the vertical extent of the upper-mode orbital is somewhat smaller than the horizontal size of the lower-mode orbital.

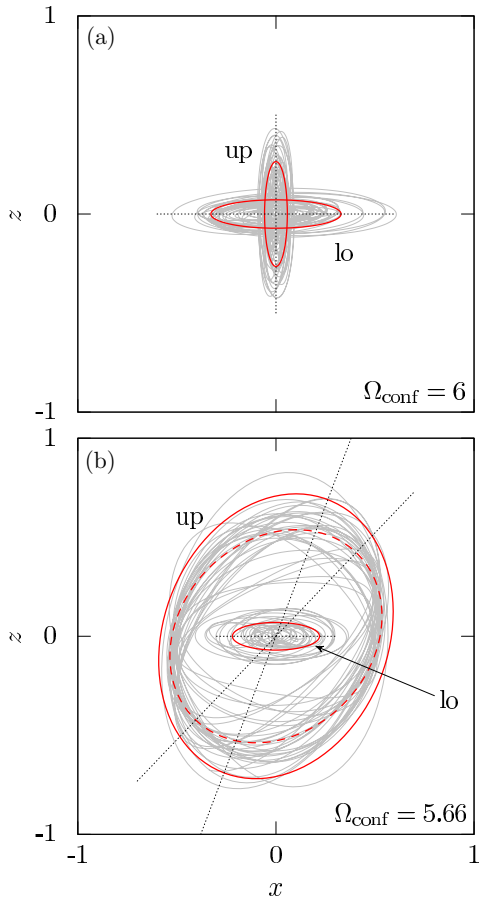

FIG. 4. (Color online) Characteristic particle trajectories representing the lower and upper wave modes for the time interval of $50\Omega_{\rm DL}^{-1}$. All parameters of (a) and (b) correspond to Figs. 2(a) and 2(c), respectively, x and z are in arbitrary units. The solid-line ellipses depict "orbitals" (straight dotted lines indicate their major axes) inside which the particles mostly reside. In (a) the separated regime, the major axes are along the coordinate axes. In (b) the hybridized regime, the major axis for the (decaying) lower mode is practically horizontal, while for (growing) upper mode it is rotated by $\simeq 70^\circ$. The dashed-line ellipse shows the contribution from the upper hybrid branch only.

In the hybridized regime illustrated in Fig. 4(b), the trajectories are determined by the superposition of (weighted) contributions from the separate and hybrid branches [see Fig. 2(c)]. As one can conclude from Fig. 3, this yields a "superposition" of ellipses oriented along the coordinate axes and those rotated by 45°. The hybrid branches are formed within a relatively small region of the Brillouin zone, yet the amplitude of the upper branch can be significantly increased, while for the lower branch it is reduced [see Eq. (13)]. All this governs the size and orientation of the corresponding orbitals: The lower orbital is practically horizontal and its size is similar to that in Fig. 4(a) since the amplitude for the lower hybrid branch is too small and hence the separate branch provides the major contribution here. On the contrary, the upper orbital is large and rotated by an angle notably smaller than 90° (but larger than 45°) since the major contribution in this case is from the enhanced hybrid branch (the corresponding orbital is indicated by the dashed-line ellipse).

B. Mode spectral density

Experimentally, fluctuation wave spectra (dispersion relations) were extracted from the observation of the particle motion which is triggered by thermal noise and damped by neutral gas friction [26,27,32].

The scenario can be mimicked by the Langevin equation, where the stochastic excitation force on each particle is uncorrelated and described by the Gaussian white noise [33–35]. We write the force in the form $M\mathbf{a}(t)$, where the elements a_j of the stochastic acceleration are defined by the first two stochastic moments, $\langle a_j(t)\rangle = 0$ and $\langle a_j(t)a_k(t')\rangle = (2\nu T/M)\delta_{jk}\delta(t-t')$ (as it follows from the fluctuation-dissipation theorem). Here, δ_{jk} is the Kronecker delta function ($j,k = x,y,z$) and T is the relevant kinetic temperature (determined by the temperature of neutral gas and mechanisms of individual dust "heating" operating in a plasma, e.g., due to charge variations [36–39]).

The perturbations for the separate modes read

$$\tilde{\boldsymbol{\zeta}} = \sum_{\alpha={\rm lo,up}} \frac{(\mathbf{a}^{(k\omega)}\cdot\boldsymbol{\zeta}_\alpha)\boldsymbol{\zeta}_\alpha}{\left[\Omega_\alpha^2(k) - \omega(\omega+i\nu)\right]\zeta_\alpha^2}, \tag{15}$$

where $\zeta_\alpha^2 \equiv \boldsymbol{\zeta}_\alpha\cdot\boldsymbol{\zeta}_\alpha$ and $\mathbf{a}^{(k\omega)}$ is the Fourier transform of the stochastic acceleration over *all* particles; for the hybrid modes, the superscript "(hyb)" has to be added.

For a monolayer comprised of N particles, the total kinetic energy is

$$K = \frac{1}{2}M\sum_{j=1}^{N}\langle v_j^2\rangle \equiv N\int d\mathbf{k}\int d\omega\, I(\mathbf{k},\omega). \tag{16}$$

Here $I(\mathbf{k},\omega) = I_l(\mathbf{k},\omega) + I_t(\mathbf{k},\omega)$ is the spectral density of thermal fluctuations, which consists of the longitudinal and transverse components (with respect to $\mathbf{k} = k\hat{\mathbf{e}}_x$, the $\mathbf{k}$ integration is over the first Brillouin zone). By representing K via the Fourier-transformed particle velocities with the components $v_{l,t}^{(k\omega)} = -i\omega\tilde{\zeta}_{x,z}$, we obtain the spectral density components expressed in terms of the horizontal and vertical eigenfrequencies

$$I_{l,t}(k,\omega) = I_0\omega^2\frac{\sigma^2 + |A_{v,h}|^2}{|\sigma^2 + A_vA_h|^2}, \tag{17}$$

where $A_{h,v}(k,\omega) \equiv \Omega_{h,v}^2(k) - \omega(\omega+i\nu)$. The spectral density scale $I_0 = \sqrt{3}\Delta^2\nu T/\left(16\pi^3\Omega_{\rm DL}^2\right)$ has the dimensionality of J·cm^2·s (here ν is not normalized).

Remarkably, $I_l(k,\omega)$ of the separate modes shows not only a bright longitudinal, but also a weak transverse component, and vice versa for $I_t(k,\omega)$ (see left panel of Fig. 5). When the coupling is intermediate-to-strong [$0.3 \lesssim p \lesssim 0.95$, see Fig. 2(d)] the "weak" components become fairly bright. For a small coupling ($p \ll 1$) Eq. (17) is reduced to $I_{l,t}(k,\omega) \simeq I_0\omega^2\left|\Omega_{h,v}^2(k) - \omega(\omega+i\nu)\right|^{-2}$ and the weak components disappear. The qualitative interpretation of these results is straightforward: The mode polarization changes between linear and elliptical, and therefore we find the "weak" components varying between zero and their peak

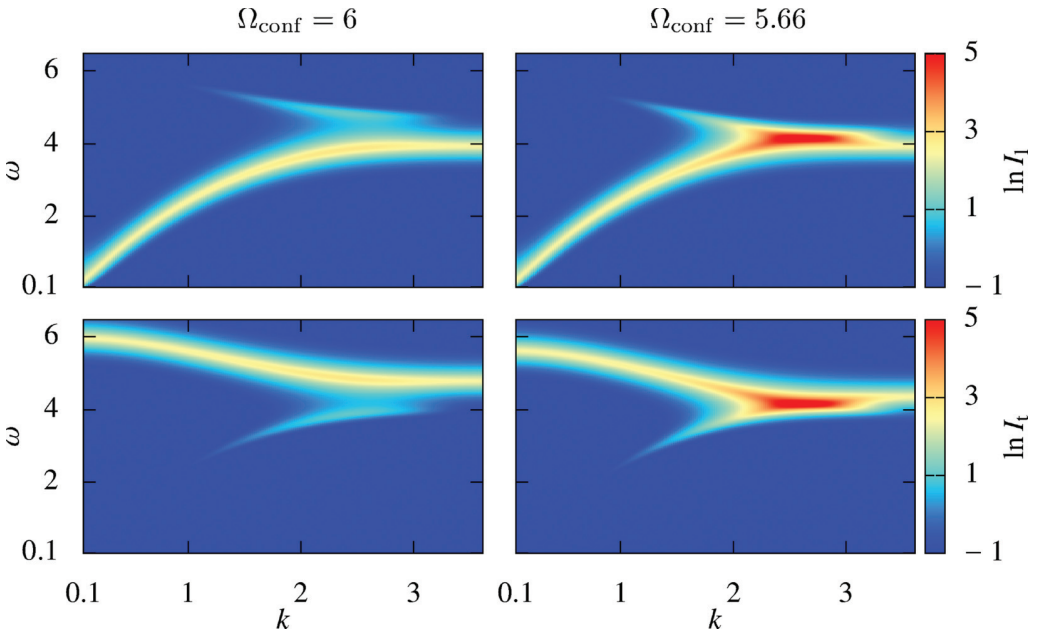

FIG. 5. (Color) Longitudinal (upper panel) and transverse (lower panel) mode spectral densities $I_{l,t}(k,\omega)$. Figures on the left show the results calculated from Eq. (17) for the separate modes, on the right the results from Eq. (18) for the hybrid modes are presented [all parameters correspond to Figs. 2(a) and 2(c), respectively]. In the separated regime, the lower mode (longitudinal without coupling) has a transverse component, the upper mode (transverse without coupling) has a longitudinal component. The longitudinal and transverse densities of the hybrid modes are equal, which follows from the orientation of their polarization ellipses [see Fig. 3(b)]. The shown example is for the normalized damping rate $\nu = 0.3$, the spectral density is in units of I_0.

brightness. The latter is smaller than the density of the "strong" components since the modes are still separated.

From the orientation of polarization ellipses of the hybrid modes (Fig. 3, $p > 1$), it is evident that their longitudinal and transverse spectral densities are equal along the hybrid branch (see right panel of Fig. 5). These densities are

$$I_l^{(\rm hyb)}(k) = I_t^{(\rm hyb)}(k) = I_0 \frac{\nu^2 + (p^2+1)B}{[\nu^2 - (p^2-1)B]^2}, \qquad (18)$$

where $B(k) = \frac{1}{2}(\Omega_v^2 - \Omega_h^2)^2(\Omega_v^2 + \Omega_h^2)^{-1}$. In accordance with Eq. (13), the decay rate of the lower hybrid mode is added to the neutral damping rate ν, while the growth rate of the upper mode is subtracted. Therefore, the relative contribution of the lower hybrid mode to the total spectral density in Eq. (18) is relatively small. The density naturally diverges if the damping threshold of the mode-coupling instability is reached [at the maximum of $p(k)$].

Figure 5 indicates that the spectral density distribution along the hybrid branch can be slightly asymmetric (with respect to the center). This is because the functions $p(k)$ and $B(k)$ are slightly asymmetric as well [see Figs. 2(c) and 2(d)]. This feature might be important for the analysis of high-resolution experimental spectra [26–30].

C. Shift of the critical point

In the limit of *weak* mode coupling, the hybridization sets in upon the crossing of the uncoupled branches $\Omega_h(k)$ and $\Omega_v(k)$. The critical point in this case is located at the border of the first Brillouin zone, $k_{\rm cr,0} = \frac{2\pi}{\sqrt{3}}$ [see Fig. 1(b)], and the corresponding critical confinement is $\Omega_{\rm cr,0}$. As one can see from Figs. 2(a) to 2(c), in the regime of *strong* coupling the critical point is shifted towards smaller k and occurs at higher confinement. Hence, we can write

$$k_{\rm cr} = k_{\rm cr,0} - \Delta k_{\rm cr}, \quad \Omega_{\rm cr} = \Omega_{\rm cr,0} + \Delta\Omega_{\rm cr}. \qquad (19)$$

In Appendix B we derive universal expressions for $k_{\rm cr}$ and $\Omega_{\rm cr}/\Omega_{\rm cr,0}$ which are functions of the wake parameters $\tilde{q}$ and $\tilde{\delta}$ (for a given κ). Let us analyze the obtained results.

The functional dependence of $\Delta k_{\rm cr}$ on the wake parameters is governed by the competition of two effects: (i) Increase of the effective dipole moment $\tilde{d}_{\rm eff}$ makes the "mode attraction" stronger, which causes $\Delta k_{\rm cr}$ to *increase*. (ii) The increase of the wake length $\tilde{\delta}$ weakens the screened wake-particle interaction, which forces $\Delta k_{\rm cr}$ to *decrease*. Figure 6(a) illustrates these effects. We fixed the wake charge $\tilde{q}$ and vary the wake length $\tilde{\delta}$ (and, hence, the dipole moment): When $\tilde{\delta}$ is sufficiently small ($\lesssim 0.2$), the effect (i) obviously dominates, resulting in an almost linear increase of $\Delta k_{\rm cr}$ with the dipole moment; the maximum is reached at $\tilde{d}_{\rm eff} \simeq 0.22$. For larger $\tilde{\delta}$ ($\gtrsim 0.3$), the effect (ii) becomes more important and $\Delta k_{\rm cr}$ starts to decrease. When the wake length is so large that the particle-wake interactions are strongly screened ($\kappa\tilde{\delta} \gtrsim 2-3$), $\Delta k_{\rm cr}$ rapidly falls off and the modes become weakly coupled again.

It is noteworthy that the k shift of the critical point can be really significant (up to $\simeq 15\%$), making the effect experimentally observable.

The dependence of $\Delta\Omega_{\rm cr}$ on $\tilde{d}_{\rm eff}$ shown in Fig. 6(b) follows essentially the same trend since the two effects mentioned above equally work for the shift of the critical confinement. However, the magnitude of $\Delta\Omega_{\rm cr}$ turns out to be much smaller than that of $\Delta k_{\rm cr}$ ($\Delta\Omega_{\rm cr}/\Omega_{\rm cr,0} \lesssim 2\%$) and therefore

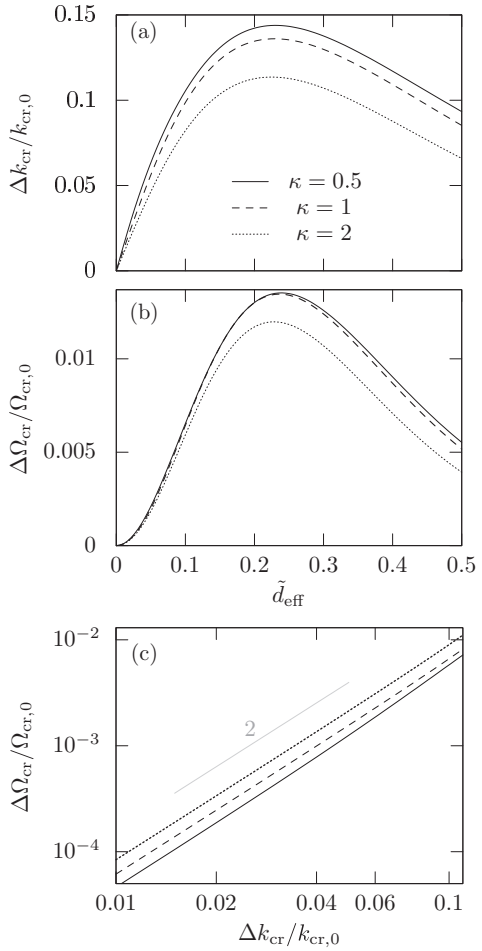

FIG. 6. The relative shift (a) of the critical wave number $\Delta k_{cr}/k_{cr,0}$ and (b) of the critical confinement $\Delta\Omega_{cr}/\Omega_{cr,0}$, as a function of the effective dipole moment of wake $\tilde{d}_{eff}$. (c) Relation between the shifts, showing that it is very close to $\Delta\Omega_{cr} \propto (\Delta k_{cr})^2$. The results are for $\tilde{q} = 0.4$ and three different values of κ.

is practically negligible. To a very good accuracy $\Delta\Omega_{cr}/\Omega_{cr,0}$ is a parabolic function of Δk_{cr}, as shown in Fig. 6(c).

Note that these results can be also obtained from a simple one-dimensional (1D) string model with next-neighbor interactions [21]. The 1D model provides compact analytical expressions for Δk_{cr} and $\Delta\Omega_{cr}/\Omega_{cr,0}$ [see Eqs. (B1) and (B2)] which are convenient for order-of-magnitude estimates. The main qualitative difference from the rigorous calculations is that the approximate results become independent of κ in the limit of small $\tilde{d}_{eff}$ (compare with Fig. 6).

V. SUMMARY AND CONCLUSION

In this paper we discussed the effects of *strong* wake-induced coupling between dust-lattice wave modes in 2D plasma crystals. So far, the mode coupling occurring due to nonreciprocal particle-wake interactions (and resulting in the *mode-coupling instability*, the major plasma-specific mechanism of melting of 2D crystals) has been systematically studied only in the *weak* regime, when the effective dipole moment of wake is assumed to be sufficiently small [22–24,27]. In this case, the longitudinal in-plane and out-of-plane modes (participating in the coupling) were shown to be strongly modified only in a small vicinity of their crossing, where they form the hybrid mode.

In fact, the regime of strong mode coupling has been already achieved in several experiments [25,27,29], and therefore careful analysis of its implications is absolutely necessary for further studies of 2D plasma crystals. Below we summarize the most notable features of the strong mode coupling:

(i) The two coupled wave modes corresponding to the in-plane and out-of-plane motion are significantly modified in a broad range of wave numbers: The branches become "attracted" to each other even before they merge and form the hybrid modes. The modified modes are called, respectively, "lower" and "upper," to distinguish from the weak-coupling regime.

(ii) Unlike the weak-coupling regime, the polarization of the two modes becomes essentially elliptical before the hybridization: The (originally longitudinal) lower mode can have a significant transverse component, the (originally transverse) upper mode has a longitudinal component.

(iii) The polarization of the hybrid modes is circular at the merging ends, and is (weakly) elliptical in the middle of the hybrid branch. The polarization ellipses in this case are rotated by 45° with respect to the polarization of the separate modes, and therefore the hybrid mode spectral density has equal longitudinal and transverse components.

(iv) The individual particle trajectories for the separate modes are localized within ellipsoidal "orbitals" with the mutually orthogonal axes. Upon the hybridization, the orbital representing the (growing) upper mode is significantly increased and rotated by an angle notably larger than 45°.

(v) The location of the hybrid mode can be significantly shifted towards smaller wave numbers, away from the border of the Brioullin zone (where the hybrid mode is formed for a weak coupling). The relative magnitude of the effect can be as high as $\simeq 15\%$.

It would be highly desirable to perform accurate experimental measurements of the individual particle trajectories and wave fluctuation spectra (performed with increased signal-to-noise ratio). The analysis of such trajectories and spectra would make it possible to reveal (at least) some of the above-mentioned features. The theory presented in this paper provides a direct relation between the magnitude of the strong-mode-coupling effects (such as the wave polarization, distribution of the fluctuation intensity, shift of the hybrid mode) and the principal characteristics of the plasma wakes.

ACKNOWLEDGMENTS

We appreciate funding from the European Research Council under the European Union's Seventh Framework Programme (FP7/2007-2013)/ERC Grant agreement 267499.

APPENDIX A: ELEMENTS OF THE DYNAMICAL MATRIX $\mathbf{D}_k$

We introduce utility functions

$$h_1(\kappa) = e^{-\kappa}(\kappa^{-1} + 2\kappa^{-2} + 2\kappa^{-3}),\ \ h_2(\kappa) = e^{-\kappa}(\kappa^{-2} + \kappa^{-3}),$$
$$h_3(\kappa) = h_1(\kappa) + h_2(\kappa),$$

to be used for expressions of the elements of D_k [Eq. (4)]. For the 1D string model with next-neighbor interactions [21] we have

$$\begin{aligned}
\Omega_h^2 &= \frac{4}{1-\tilde{q}}\left(h_1(\kappa)+\tilde{q}h_2(\tilde{\kappa})-\frac{\tilde{q}}{1+\tilde{\delta}^2}h_3(\tilde{\kappa})\right)\sin^2\frac{1}{2}k,\\
\Omega_v^2 &= \Omega_{\mathrm{conf}}^2\\
&\quad -\frac{4}{1-\tilde{q}}\left(h_2(\kappa)-\tilde{q}h_2(\tilde{\kappa})+\frac{\tilde{q}\tilde{\delta}^2}{1+\tilde{\delta}^2}h_3(\tilde{\kappa})\right)\sin^2\frac{1}{2}k,\\
\sigma &= 2\frac{\tilde{q}\tilde{\delta}}{(1-\tilde{q})(1+\tilde{\delta}^2)}h_3(\tilde{\kappa})\sin k. \qquad \text{(A1)}
\end{aligned}$$

where $\tilde{\kappa}=\kappa\sqrt{1+\tilde{\delta}^2}$.

The rigorous results for 2D monolayers are obtained by taking into account interactions with all neighbors [22,30]. For the wave vector $\mathbf{k}=k\hat{\mathbf{e}}_x$, the elements of D_k are

$$\begin{aligned}
\Omega_h^2 &= \frac{2}{1-\tilde{q}}\sum_{m,n}\left(\frac{s_x^2}{s^2}h_1(\kappa s)-\frac{s_y^2}{s^2}h_2(\kappa s)\right.\\
&\quad \left.+\tilde{q}h_2(\kappa s_\delta)-\tilde{q}\frac{s_x^2}{s_\delta^2}h_3(\kappa s_\delta)\right)\sin^2\frac{1}{2}ks_x,\\
\Omega_v^2 &= \Omega_{\mathrm{conf}}^2-\frac{2}{1-\tilde{q}}\sum_{m,n}\left(h_2(\kappa s)-\tilde{q}h_2(\kappa s_\delta)\right.\\
&\quad \left.+\tilde{q}\frac{\tilde{\delta}^2}{s_\delta^2}h_3(\kappa s_\delta)\right)\sin^2\frac{1}{2}ks_x,\\
\sigma &= \frac{\tilde{q}\tilde{\delta}}{1-\tilde{q}}\sum_{m,n}\frac{s_x}{s_\delta^2}h_3(\kappa s_\delta)\sin ks_x, \qquad \text{(A2)}
\end{aligned}$$

where $s_x=\sqrt{3}m/2$, $s_y=m/2+n$, $s=\sqrt{m^2+n^2+mn}$, $s_\delta=\sqrt{s^2+\tilde{\delta}^2}$, the summation is over all integers except $(0,0)$.

APPENDIX B: SHIFT OF THE CRITICAL POINT [EQ. (19)]

The critical wave number k_{cr} and critical confinement frequency Ω_{cr} for the onset of hybridization are determined from the following conditions on the reduced coupling parameter: $p(k_{\mathrm{cr}},\Omega_{\mathrm{cr}})=1$ and $\partial p/\partial k|_{k_{\mathrm{cr}},\Omega_{\mathrm{cr}}}=0$.

For the 1D string model we use Eq. (A1), which yields

$$\Delta k_{\mathrm{cr}}=\arctan\mathcal{D},\quad \frac{\Omega_{\mathrm{cr}}^2}{\Omega_{\mathrm{cr},0}^2}=\frac{1}{2}(1+\sqrt{1+\mathcal{D}^2}), \qquad \text{(B1)}$$

where

$$\mathcal{D}=\frac{2\tilde{q}\tilde{\delta}h_3(\tilde{\kappa})}{(1+\tilde{\delta}^2)h_3(\kappa)-\tilde{q}(1-\tilde{\delta}^2)h_3(\tilde{\kappa})}.$$

For small $\tilde{\delta}$ we get $\mathcal{D}\to 2\tilde{q}\tilde{\delta}/(1-\tilde{q})\equiv 2\tilde{d}_{\mathrm{eff}}$. Thus, in the weak-coupling regime we get a simple universal relation between Δk_{cr} and $\Delta\Omega_{\mathrm{cr}}$,

$$\frac{\Delta\Omega_{\mathrm{cr}}}{\Omega_{\mathrm{cr},0}}\simeq\frac{1}{8}(\Delta k_{\mathrm{cr}})^2\simeq\frac{1}{2}\tilde{d}_{\mathrm{eff}}^2. \qquad \text{(B2)}$$

For the rigorous 2D model we employ Eq. (A2) and obtain the following equations for k_{cr} and Ω_{cr}:

$$\begin{aligned}
&\sum_{m,n}s_x(\mathcal{A}\cos k_{\mathrm{cr}}s_x+\mathcal{B}\sin k_{\mathrm{cr}}s_x)=0,\\
&\frac{\Omega_{\mathrm{cr}}^2}{\Omega_{\mathrm{cr},0}^2}=\frac{\sum_{m,n}[\mathcal{A}\sin k_{\mathrm{cr}}s_x+\mathcal{B}(1-\cos k_{\mathrm{cr}}s_x)]}{\sum_{m,n}\mathcal{B}[1-(-1)^m]}, \qquad \text{(B3)}
\end{aligned}$$

where

$$\begin{aligned}
\mathcal{A}(\tilde{q},\tilde{\delta},\kappa) &= 4\tilde{q}\tilde{\delta}\frac{s_x}{s_\delta^2}h_3(\kappa s_\delta),\\
\mathcal{B}(\tilde{q},\tilde{\delta},\kappa) &= 2\frac{s_x^2}{s^2}h_3(\kappa s)-2\tilde{q}\frac{s_x^2-\tilde{\delta}^2}{s_\delta^2}h_3(\kappa s_\delta).
\end{aligned}$$

The first equation (B3) yields k_{cr}, which should then be substituted to the second equation to obtain Ω_{cr}.

[1] P. K. Shukla and A. A. Mamun, *Introduction to Dusty Plasma Physics* (IOP, Philadelphia, 2002).
[2] V. E. Fortov, A. V. Ivlev, S. A. Khrapak, A. G. Khrapak, and G. E. Morfill, Phys. Rep. **421**, 1 (2005).
[3] P. K. Shukla and B. Eliasson, Rev. Mod. Phys. **81**, 25 (2009).
[4] M. Bonitz, C. Henning, and D. Block, Rep. Prog. Phys. **73**, 066501 (2010).
[5] V. E. Fortov and G. E. Morfill, *Complex and Dusty Plasmas: From Laboratory to Space*, Series in Plasma Physics (CRC Press, Boca Raton, 2010).
[6] G. E. Morfill and A. V. Ivlev, Rev. Mod. Phys. **81**, 1353 (2009).
[7] A. Ivlev, H. Löwen, G. Morfill, and C. P. Royall, *Complex Plasmas and Colloidal Dispersions: Particle-Resolved Studies of Classical Liquids and Solids* (World Scientific, Singapore, 2012).
[8] J. H. Chu and L. I, Phys. Rev. Lett. **72**, 4009 (1994).
[9] H. Thomas, G. E. Morfill, V. Demmel, J. Goree, B. Feuerbacher, and D. Möhlmann, Phys. Rev. Lett. **73**, 652 (1994).
[10] F. Melandsö and J. Goree, Phys. Rev. E **52**, 5312 (1995).
[11] S. V. Vladimirov and A. A. Samarian, Phys. Rev. E **65**, 046416 (2002).
[12] I. H. Hutchinson, Phys. Plasmas **18**, 032111 (2011).
[13] S. V. Vladimirov and O. Ishihara, Phys. Plasmas **3**, 444 (1996).
[14] O. Ishihara and S. V. Vladimirov, Phys. Plasmas **4**, 69 (1997).
[15] M. Lampe, G. Joyce, G. Ganguli, and V. Gavrishchaka, Phys. Plasmas **7**, 3851 (2000).
[16] R. Kompaneets, U. Konopka, A. V. Ivlev, V. Tsytovich, and G. Morfill, Phys. Plasmas **14**, 052108 (2007).
[17] M. Lampe, T. B. Röcker, A. V. Ivlev, S. K. Zhdanov, and G. E. Morfill, Phys. Plasmas **19**, 113703 (2012).
[18] G. Lapenta, Phys. Rev. E **62**, 1175 (2000).
[19] A. V. Ivlev, S. K. Zhdanov, S. A. Khrapak, and G. E. Morfill, Phys. Rev. E **71**, 016405 (2005).
[20] V. A. Schweigert, I. V. Schweigert, A. Melzer, A. Homann, and A. Piel, Phys. Rev. E **54**, 4155 (1996).
[21] A. V. Ivlev and G. Morfill, Phys. Rev. E **63**, 016409 (2000).
[22] S. K. Zhdanov, A. V. Ivlev, and G. E. Morfill, Phys. Plasmas **16**, 083706 (2009).

[23] T. B. Röcker, A. V. Ivlev, R. Kompaneets, and G. E. Morfill, Phys. Plasmas **19**, 033708 (2012).
[24] T. B. Röcker, S. K. Zhdanov, A. V. Ivlev *et al*., Phys. Plasmas **19**, 073708 (2012).
[25] A. V. Ivlev, U. Konopka, G. Morfill, and G. Joyce, Phys. Rev. E **68**, 026405 (2003).
[26] L. Couëdel, V. Nosenko, S. K. Zhdanov, A. V. Ivlev, H. M. Thomas, and G. E. Morfill, Phys. Rev. Lett. **103**, 215001 (2009).
[27] L. Couëdel, V. Nosenko, A. V. Ivlev, S. K. Zhdanov, H. M. Thomas, and G. E. Morfill, Phys. Rev. Lett. **104**, 195001 (2010).
[28] B. Liu, J. Goree, and Y. Feng, Phys. Rev. Lett. **105**, 085004 (2010).
[29] B. Liu, J. Goree, and Y. Feng, Phys. Rev. Lett. **105**, 269901(E) (2010).
[30] L. Couëdel, S. K. Zhdanov, A. V. Ivlev, V. Nosenko, H. M. Thomas, and G. E. Morfill, Phys. Plasmas **18**, 083707 (2011).
[31] P. Epstein, Phys. Rev. **23**, 710 (1924).
[32] S. Nunomura, J. Goree, S. Hu, X. Wang, A. Bhattacharjee, and K. Avinash, Phys Rev. Lett. **89**, 035001 (2002).
[33] F. Schwabl, *Statistische Mechanik* (Springer, New York, 2006).
[34] S. Zhdanov, S. Nunomura, D. Samsonov, and G. Morfill, Phys. Rev. E **68**, 035401(R) (2003).
[35] N. G. van Kampen, *Stochastic Processes in Physics and Chemistry* (Elsevier, Amsterdam, 1981).
[36] S. Nunomura, T. Misawa, N. Ohno, and S. Takamura, Phys. Rev. Lett. **83**, 1970 (1999).
[37] O. S. Vaulina, S. A. Khrapak, A. P. Nefedov, and O. F. Petrov, Phys. Rev. E **60**, 5959 (1999).
[38] A. V. Ivlev, U. Konopka, and G. E. Morfill, Phys. Rev. E **62**, 2739 (2000).
[39] M. Y. Pustylnik, N. Ohno, S. Takamura, and R. Smirnov, Phys. Rev. E **74**, 046402 (2006).

Bibliography

[1] B.M. Smirnov, *Physics of Ionized Gases*, Wiley-VCH (2001).

[2] Yu.P. Raizer, *Gas Discharge Physics*, Springer-Verlag Berlin (1991).

[3] D.A. Mendis, Astrophys. & Space Sci. **65**, 5 (1979).

[4] D.A. Mendis and M. Rosenberg, Astronomy & Astrophys. **32**, 419 (1994).

[5] B.M. Smirnov, *Plasma Processes and Plasma Kinetics*, Wiley-VCH (2007).

[6] S.V. Vladimirov and K. Ostrikov, Phys. Rep. **4**, 393(3) (2004).

[7] A. Ivlev *et al.*, *Complex Plasmas and Colloidal Dispersions*, World Scientific (2012).

[8] G.E. Morfill and A.V. Ivlev, Rev. Mod. Phys. **81**, 1353 (2009).

[9] S. Herminghaus, *Wet granular matter. A truly complex fluid.*, World Scientific (2013).

[10] U. Konopka, *Wechselwirkungen geladener Staubteilchen in Hochfrequenzplasmen*, Phd thesis (2000).

[11] K. Takahashi *et al.*, Phys. Rev. E. **58**, 7805 (1998).

[12] P. Bandyopadhyay *et al.*, AIP Conf. Proceed. **1397**, 389 (2011).

[13] M. Schwabe *et al.*, Phys. Rev. Lett. **106**, 21 (2011).

[14] P.K. Shukla and A.A. Mamun, *Introduction to Dusty Plasma Physics*, IoP Publishing (2002).

[15] V.N. Tsytovich *et al.*, *Elementary Physics of Complex Plasmas*, Springer Berlin Heidelberg (2008).

[16] S. Mitic *et al.*, Phys. Rev. Lett. **101**, 12 (2008).

[17] M.H. Thoma *et al.*, IEEE Trans. Plas. Science **35**, 255 (2007).

[18] R. Seurig *et al.*, Acta Astronautica **61**, 940 (2007).

[19] P.J. Hargis *et al.*, Rev. Sci. Instrum. **65**, 140 (1994).

[20] R.V. Kennedy and J.E. Allen, J. Plasma Phys. **69**, 485 (2003).

[21] V.E. Fortov *et al.*, Phys. Rep. **421**, 1 (2005).

[22] D. Winske and M.E. Jones, IEEE Trans. Plas. Sci. **23**, 2 (1995).

[23] O. Vaulina *et al.*, Phys. Rev. E **60**, 5959 (1999).

[24] G. Morfill *et al.*, Phys. Rev. Lett. **83**, 971 (1999).

[25] A.V. Ivlev *et al.*, Phys. Rev. E **62**, 2739 (2000).

[26] H. Rothermel *et al.*, Phys. Rev. Lett. **89**, 175001 (2002).

[27] G. Morfill *et al.*, Phys. Rev. Lett. **83**, 1598 (1999).

[28] D. Samsonov and J. Goree, Phys. Rev. E **59**, 1047 (1999).

[29] Z. Zakrzewski and T. Kopiczynski, Plasma Phys. **16**, 1195 (1974).

[30] A.V. Ivlev, G. Morfill, V.E. Fortov, Phys. Plasmas **6**, 1416 (1999).

[31] V.A. Schweigert, Plasma Phys. Rep. **27**, 997 (2001).

[32] M. Lampe *et al.*, Phys. Plasmas **10**, 1500 (2003).

[33] I.H. Hutchinson, Phys. Plasmas **18**, 3 (2011).

[34] S.V. Vladimirov and M. Nambu, Phys. Rev. E **52**, R2172 (1995).

[35] S.V. Vladimirov and O. Ishihara, Phys. Plasmas **3**, 444 (1996).

[36] O. Ishihara and S.V. Vladimirov, Phys. Plasmas **4**, 69 (1997).

[37] G. Lapenta, Phys. Rev. E **62**, 1175 (2000).

[38] D. Winske *et al.*, Phys. Plasmas **7**, 2320 (2000).

[39] M. Lampe *et al.*, Phys. Plasmas **7**, 3851 (2000).

[40] L.-J. Hou *et al.*, Phys. Rev. E **68**, 016410 (2003).

[41] A.V. Ivlev *et al.*, G. Joyce, Phys. Rev. Lett. **92**, 205007 (2004).

[42] A.V. Ivlev *et al.*, Phys. Rev. E **71**, 016405 (2005).

[43] S.A. Khrapak *et al.*, Phys. Rev. E **66**, 046414 (2002).

[44] S.A. Khrapak *et al.*, Phys. Rev. Lett. **90**, 225002 (2003).

[45] E.M. Lifshitz and L. P. Pitaevskii, *Physical Kinetics*, Pergamon Oxford (1981).

[46] A.F. Alexandrov *et al.*, *Principles of Plasma Electrodynamics*, Springer New York (1984).

[47] M. Surendra and D.B. Graves, IEEE Trans. Plasma Sci. **19**, 144 (1991).

[48] V.A. Godyak and R.B. Piejak, Appl. Phys. Lett. **63**, 3137 (1993).

[49] D. Vender *et al.*, J. Vac. Sci. Technol. **A 10**, 1331 (1992).

[50] T. Gans *et al.*, Europhys. Lett. **66**, 232 (2004).

[51] R. Kompaneets *et al.*, Phys. Plasmas **14**, 052108 (2007).

[52] T.B. Röcker *et al.*, Phys. Plasmas **19**, 033708 (2012).

[53] E.W. McDaniel, *Collision Phenomena in Ionized Gases*, Wiley New York (1964).

[54] A.V. Phelps, J. Appl. Phys. **76**, 747 (1994).

[55] I.V. Schweigert *et al.*, Phys. Plasmas **12**, 113501 (2005).

[56] P.L. Bhatnagar *et al.*, Phys. Rev. **94**, 511 (1954).

[57] A. Melzer *et al.*, Phys. Rev. E **54**, R46 (1996).

[58] M. Zeuner and J. Meichsner, Vacuum **46**, 151 (1995).

[59] S. Robertson and Z. Sternovsky, Phys. Rev. E **67**, 046405 (2003).

[60] D. Else *et al.*, Phys. Plasmas **16**, 062106 (2009).

[61] S.A. Maiorov *et al.*, in 34th EPS Conference on Plasma Physics, Warsaw, 2 - 6 July 2007 (2007), ECA Vol. **31F**, P2.115.

[62] O.S. Vaulina and S.A. Khrapak, JETP **90**, 287 (2000).

[63] O.S. Vaulina and S.A. Khrapak, JETP **92**, 228 (2001).

[64] D.H.E. Dubin and T.M. O'Neil, Rev. Mod. Phys. **71**, 87 (1999).

[65] N.D. Drummond and R.J. Needs, Phys. Rev. Lett. **102**, 126402 (2009).

[66] E. Wigner, Phys. Rev. **46**, 1002 (1934).

[67] G.E. Morfill *et al.*, Plasma Phys. Rep. **29**, 1 (2003).

[68] J.H. Chu and Lin I, Phys. Rev. Lett. **72**, 4009 (1994).

[69] H. Thomas *et al.*, Phys. Rev. Lett. **73**, 652 (1994).

[70] J. Kong *et al.*, Phys. Rev. E **84**, 016411 (2011).

[71] T.W. Hyde *et al.*, Phys. Rev. E **87**, 053106 (2013).

[72] O. Arp *et al.*, Phys. Rev. Lett. **93**, 165004 (2004).

[73] A. Melzer, Phys. Rev. E **73**, 056404 (2006).

[74] L. Wörner *et al.*, Eu. Phys. Lett. **100**, 35001 (2012).

[75] Y. Khodataev *et al.*, Phys. Scr. **T89**, 95 (2001).

[76] P. Epstein, Phys. Rev. **23**, 710 (1924).

[77] B. Liu *et al.*, Phys. Plasmas **10**, 9 (2003).

[78] V. V. Zhakhovskii *et al.*, JETP Lett. **66**, 419 (1997).

[79] A. Melzer *et al.*, Phys. Rev. Lett. **83**, 3194 (1999).

[80] G.A. Hebner *et al.*, Phys. Rev. E **68**, 016403 (2003).

[81] S. Nunomura *et al.*, Phys. Rev. Lett. **83**, 1970 (1999).

[82] M.Y. Pustylnik *et al.*, Phys. Rev. E **74**, 046402 (2006).

[83] V.V. Yaroshenkov *et al.*, Phys. Rev. E **71**, 046405 (2005).

[84] S.K. Zhdanov *et al.*, Phys. Plasmas **12**, 072312 (2005).

[85] R. Kompaneets *et al.*, Phys. Plasmas **12**, 062107 (2005).

[86] F. Riewe, Phys. Rev. E **55**, 3 (1996).

[87] E.M. Rabei *et al.*, Turk. J. Phys. **28**, 213 (2004).

[88] C.E. Smith, J. Phys. Conf. Ser. **237**, 012021 (2010).

[89] A.V. Ivlev and G. Morfill, Phys. Rev. E **63**, 016409 (2001).

[90] S.K. Zhdanov *et al.*, Phys. Plasmas **16**, 083706 (2009).

[91] L. Couëdel *et al.*, Phys. Rev. Lett. **104**, 195001 (2010).

[92] L. Couëdel *et al.*, Phys. Plasmas **18**, 083707 (2011).

[93] S.V. Vladimirov *et al.*, Phys. Plasmas **13**, 030703 (2006).

[94] K. Jiang *et al.*, Eu. Phys. Lett. **85**, 45002 (2009).

[95] P. Harvey *et al.*, Phys. Rev. E **81**, 057401 (2010).

[96] S. Zhdanov *et al.*, Eu. Phys. Lett. **89**, 25001 (2010).

[97] S. Zhdanov *et al.*, New J. Phys. **5**, 74 (2003).

[98] S. Nunomura *et al.*, Phys. Rev. Lett. **84**, 5141 (2000).

[99] S. Nunomura *et al.*, Phys. Rev. E **65**, 066402 (2002).

[100] D. Samsonov *et al.*, Phys. Rev. E **71**, 026410 (2005).

[101] A.V. Ivlev *et al.*, Phys. Rev. E **68**, 026405 (2003).

[102] C.L. Wang *et al.*, J. Plasma Phys. **25**, 225 (1981).

[103] C.K. Birdsall, IEEE Trans. Plasma Sci. **19**, 65 (1991).

[104] B.M. Smirnov, Sov. Phys. Tech. Phys. **11**, 1388 (1967).

[105] M. Abramowitz and I. Stegun, *Handbook of Mathematical Functions*, Dover Publications (1965).

[106] B. Liu *et al.*, Phys. Rev. Lett. **105**, 085004 (2010).

[107] B. Liu *et al.*, Phys. Rev. Lett. **105**, 269901 (2010).

[108] N.G. van Kampen, *Stochastic Processes in Physics and Chemistry*, Elsevier Amsterdam (1981).

[109] E.L. Cussler, *Diffusion: Mass Transfer in Fluid Systems*, Cambridge University Press (1997).

[110] F. Schwabl, *Statistische Mechanik*, Springer Berlin Heidelberg (2006).

[111] L. Couëdel *et al.*, Phys. Rev. Lett. **103**, 215001 (2009).

[112] Personal conversation with C.-R. Du (2013).

[113] R. Kompaneets *et al.*, arXiv:1401.3688v1 (2014).

[114] Personal conversation with V. Nosenko.

[115] A.S. Phani *et al.*, J. Acoust. Soc. Am. **119**, 4 (2006).

[116] D.S. Lemons, *An Introduction to Stochastic Processes*, John Hopkins University Press (2002).

[117] L.-J. Hou *et al.*, Phys. Rev. E **70**, 056406 (2004).

[118] K. Jiang, *Particle manipulation in plasma device & Dynamics of binary complex plasma*, Phd thesis LMU (2001).

[119] L. Verlet, Phys. Rev. **159**, 98 (1967).

[120] P. Schofield, Comp. Phys. Comm. **5**, 17 (1973).

[121] D. Beemann, J. Comp. Phys. **20**, 130 (1976).

[122] J.H. Friedman, Tech. Rep. LCS **5** (1984).

[123] D. Schwarz, Mathworks File Exchange #17986 (2007).

Acknowledgement

I am very grateful to

- Prof. Dr. Dr. h.c. Gregor Morfill for the chance to do the thesis within his group and his supervision,
- Priv.-Doz. Dr. Alexei Ivlev for his teaching, guidance, critics, and настоящий русский подход, *not* only in physics,
- Priv.-Doz. Dr. Sergey Zhdanov, Prof. Martin Lampe, Prof. Dr. Markus Thoma, Dr. Roman Kompaneets, Dr. Tetsuji Shimizu, Dr. Lenaic Couëdel, Dr. Vladimir Nosenko, Dr. Ke Jiang, Dr. Peter Huber, and Dr. Daniel Mohr for their help, the fruitful work and share of their experience,
- Angelika Langer, Silvia Goldbrunner, and Birgit Boller for short administrative channels,
- my parents Ernst Werner and Ingrid Maria, and my brother Dennis "Poomeister" for supporting, understanding, motivating me in every situation, more than I will ever deserve,
- Stephan, Florian, Anna, Hubert, Leila, Uwe, Alex, and Robert for being my loyal friends and conspired strategy commitee,
- Dr. Ferdinand Helmer and Dr. Jochen Baumann, my dedicated teachers in the early years,
- Dr. Hans-Eberhard Hehl for his mentoring.

Without all of you this thesis would not have been possible.